# *Ab Initio* Study of Dynamically Tunable Catalysis for Carbon Dioxide Reduction

by

Babatunde O. Alawode
S.M., Mechanical Engineering, Massachusetts Institute of Technology (2015)
S.M., Material Science and Engineering, Massachusetts Institute of Technology (2015)

Submitted to the Department of Mechanical Engineering
in partial fulfillment of the requirements for the degree of
Doctor of Philosophy
at the
MASSACHUSETTS INSTITUTE OF TECHNOLOGY
September 2017



Signature redacted

Author .....
Department of Mechanical Engineering
June 5th, 2017

Certified by..... Signature redacted .....
Alexie M. Kolpak
Assistant Professor, Department of Mechanical Engineering
Thesis Supervisor

Certified by..... Signature redacted .....
Betar M. Gallant
Assistant Professor, Department of Mechanical Engineering
Thesis Supervisor

Certified by.... Signature redacted .....
Ahmed Ghoniem
Professor, Department of Mechanical Engineering
Thesis Supervisor

Accepted by..... Signature redacted .....
Rohan Abeyaratne
Chairman, Department Committee on Graduate Theses

# *Ab Initio* Study of Dynamically Tunable Catalysis for Carbon Dioxide Reduction

by

Babatunde O. Alawode

Submitted to the Department of Mechanical Engineering
on June 5th, 2017, in partial fulfillment of the
requirements for the degree of
Doctor of Philosophy

## Abstract

Catalytic conversion of $CO_2$ into useful chemicals is an attractive alternative to expensive physical carbon sequestration methods. However, this approach is challenging because current chemical conversion methods employ high temperatures or pressures, thereby increasing cost and potentially leading to net carbon positive processes. Our work presents a novel materials system for dynamic modification of catalytic behavior via polarization reversal in a ferroelectric substrate (i.e tunable catalysis) in order to reduce the energy required for these reactions.

Dynamically Tunable Catalysis (catalysis enhanced by real-time changes in the surface chemistry of the catalyst) has been gaining ground recently as a way to go beyond the limits of Sabatier's principle. However, it is not clear whether the catalytic activities of proposed schemes are really better than simply finding a good material close to the top of the volcano in a static catalysis scheme. In this thesis, we study the tunable catalysis scheme of ZnO supported on a ferroelectric. We demonstrate that the physics and chemistry at the surface of the ZnO film can be tuned via the polarization direction of the $PbTiO_3$ substrate and the thickness of the ZnO. Using Density Functional Theory (DFT), we evaluate the effect of the number of layers and ZnO film orientation on the film's surface chemistry. By characterizing the adsorption and reduction of $CO_2$ on the different surfaces, we show that a tunable catalysis scheme can significantly increase the rate of $CO_2$ reduction by several orders of magnitude with less energy cost than simply increasing reaction temperatures and pressures.

In addition, we develop a scheme to induce ferroelectricity in ZnO films. If proven in the lab, this will be the first scheme to induce ferroelectricity in ZnO without relying on the involvement of dipole-inducing dopants. In addition, we show that this scheme allows for consistent surface chemistry in tunable catalysis which is important for practical applications. Finally, for the first time, we develop an approach to screen for new tunable catalyst candidates that can potentially be applied to oxides. Our work opens new doors for the catalysis of $CO_2$ reactions.

This work provides a quantitative indication of the promise of tunable catalysts

and also their limitations. It thus represents an important contribution to both interface physics and surface catalysis.

Thesis Supervisor: Alexie M. Kolpak
Title: Assistant Professor, Department of Mechanical Engineering

Thesis Supervisor: Betar M. Gallant
Title: Assistant Professor, Department of Mechanical Engineering

Thesis Supervisor: Ahmed Ghoniem
Title: Professor, Department of Mechanical Engineering

# Acknowledgments

To the people who have supported or collaborated with me in one way or another in the past five years of grad school:

Akin & Deola & Moyo Oyedele, Amara Uyanna, Adanna Chukwuma, Chika Ugboh, Yetunde Alo, Chibueze Amanchukwu, David Kwabi, Pierre Claver Yao and the rest of MIT West African Clan, Prof. Alexie Kolpak, Prof. Sang-Gook Kim, Prof. Betar Gallant, Prof. Ahmed Ghoniem, the Kim Group members especially Prof. Jeehwan Kim, Yunjo Kim and Samuel Cruz, the Kolpak Group members especially Nongnuch Artrith, Jerry (Xi) Rong, Levi Lentz and Brian Kolb, Sam Bhattacharyya, Nwike Iloeje, Mureji Fatunde, Joy Ekuta, Chidube Ezeozue, Xiaoyu Wu, Mrs. Iyabo Attah, Mrs. Ifeanyi Olagbaju, Mrs. Margaret Anyigbo, Darshan Desai, Joshua Eniola, Heather Beem, Sam Perli, Courtney Jean-Baptiste, Kunle Adeyemo, Joan Omijeh, Jerop Kipruto, Chinwe Ibecheozor, Darshan Desai, Lauren Siegel, QeeQee Gao, Kemi Adeyemi, Doreen Ndishabandi, Thomas Richman, Julia & Pedro & Gabriella Reynolds, Donna Levin, Nick Meyer, Bill Aulet, Elaine Chen, Georgie Campbell-Flatter, Julia Turnbull, Linda Baa-Mintah, Natasha Somji, QeeQee Gao, the Alawode family, the Martin Trust Center for MIT Entrepreneurship, the MIT Legatum Center, the PKG Public Service Center, MISTI, D-Lab, the MIT Energy Initiative, S3TEC, the Center for Material Science and Engineering at MIT and the Martin Family.

Thank you.

# Contents

# List of Figures

# List of Tables

# Chapter 1

# Introduction

*A short part of the first section of this chapter was published in a previous work [6].*

## 1.1 Global warming and $CO_2$ conversion

The world currently meets most of its energy needs by burning fossil fuels. [7] Beginning from the industrial revolution, this has resulted in increasing concentrations of greenhouse gases in the atmosphere and concomitant rise in atmospheric temperatures (Fig. 1-2). In an ideal world, switching to renewable energies is desired, but renewable energies are limited by the storage capacity of existing batteries. For example, Fig. 1-1 compares the specific energies of gasoline and diesel to that of Li ion batteries. We see that the fossil fuels are far better for energy storage, both when volume or weight is considered. This advantage, combined with the ease of transportation and low cost, means that we cannot expect to completely end our reliance on fossil fuels in the next few decades. This presents a unique dilemma, as we cannot afford the environmental cost of continous usage of fossil fuels. This means we have to consider means of harnessing the advantages of fossil fuel use (cheap and reliable energy) while avoiding the side effects (global warming).

There are currently three approaches to this: direct usage, sequestration and conversion. In the first case, carbon dioxide has some interesting but rather limited uses in beverages, fire extinguishers, oil recovery, etc. [8] Perhaps a better-studied

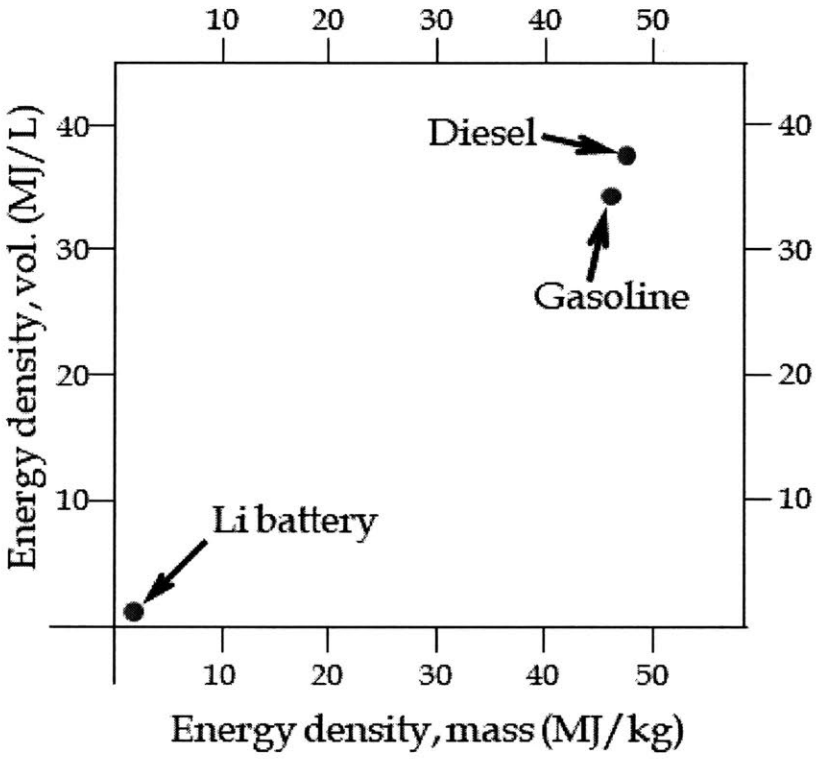


Figure 1-1: Specific volumetric and gravimetric energies of fossil fuels compared to Li-ion batteries.

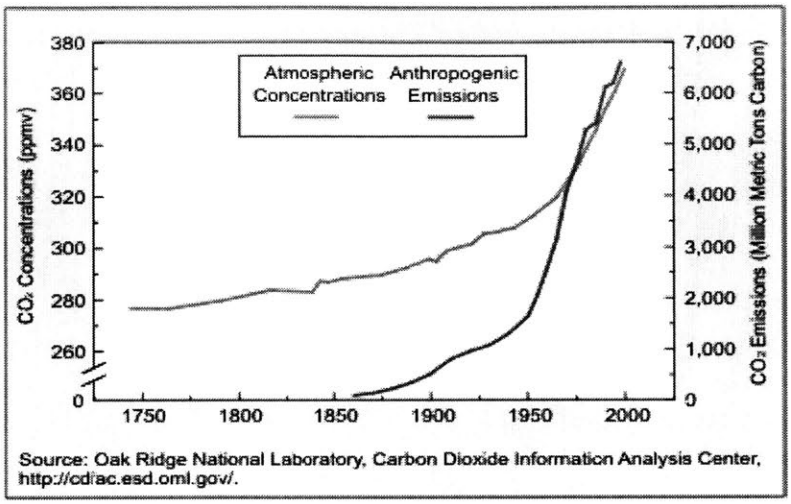


Figure 1-2: Trends in Atmospheric Concentrations and Anthropogenic Emissions of Carbon Dioxide.

case is that of physical capture of the gas. This method, known as Carbon Capture and Storage (capture, compression, transportation, and storage of $CO_2$ in suitable subterranean geological reservoirs) [9] is a large-scale approach which may be limited by cost and our understanding of the long-term capacity of geological formations to hold $CO_2$. Moreover, capturing and compressing $CO_2$ may increase the fuel needs of, for example, a coal-fired CCS plant by 25-40%. [10] These and other system costs are estimated to increase the cost of the energy produced by 21–91% for purpose built plants, and even more for existing ones. [10] There are concerns that safe and permanent storage of $CO_2$ cannot be guaranteed and that even very low leakage rates could undermine any climate mitigation effects. [11, 12, 13]

The third approach, chemical or biological conversion, may be the best option yet if we are able to find cheaper ways to achieve the fixation. Since carbon and oxygen are both key elements in organic chemistry, there are a wide range of chemicals (Fig. 1-4) that can at least theoretically utilize $CO_2$ as a feedstock for production, including organic acids, alcohols, esters, and sugars which have important commercial uses. [14, 9] For example, methanol, which is the basic chemical building block of paints, solvents and plastics, has innovative applications in energy, transportation fuels [15] and fuel cells. It had a global demand of 45.6 million metric tons and generated $36

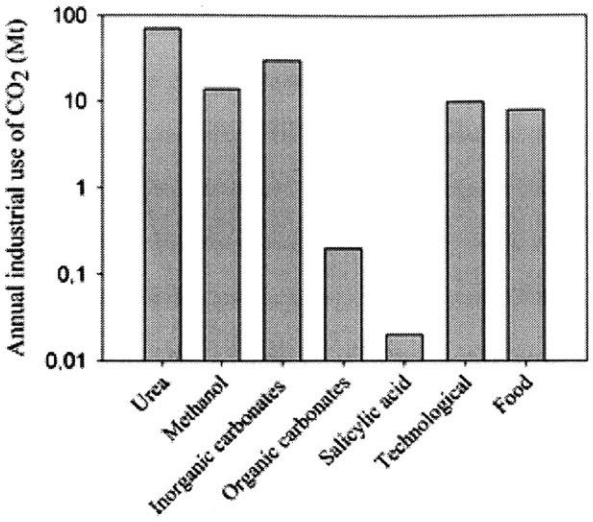


Figure 1-3: Annual industrial use of $CO_2$. Note the vertical axis is logarithmic. Adapted from Ref. [1].

billion in economic activity in 2010 [16].

Another potential large scale use of $CO_2$ is the production of cyclic carbonates. These have several commercial applications due to their use as chemical intermediates (e.g for dimethyl carbonate production) [17] and as aprotic polar solvents. [18] A particularly important and growing application of cyclic carbonates is their use as electrolytes in lithium ion batteries. [19] Practically, however, $CO_2$ is utilized to a very limited extent in industrial production processes. Fig. 1-3 shows some trends in actual $CO_2$ use. We see that scale of conversion to methanol is comparable to that of the technological uses (primarily enhanced oil recovery) though the former has a much greater demand than the latter. This is partly due to the fact that the most efficient reactant for the conversion is frequently not $CO_2$. For example, in the industrial production of methanol, a mixture of CO and $H_2$ (syngas) is the primary feedstock as these are much easier to obtain (by secondary conversion from natural gas) and a relatively small amount of $CO_2$ is only fed into the reactor to ensure conversion of any unreacted $H_2$. Another stumbling block to the adoption of $CO_2$ as a choice reactant is the high energy and financial cost of the conversion process itself. For example, commercial production of cyclic carbonates relies on quaternary ammonium or phosphonium salts as catalysts which require the use of high

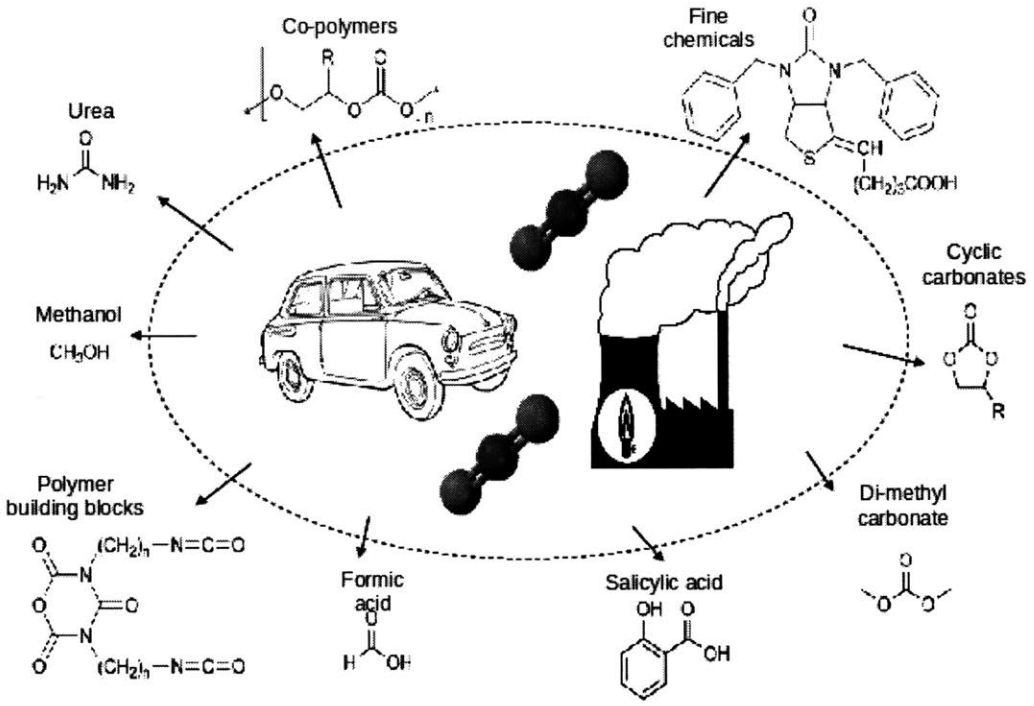


Figure 1-4: Potential products of carbon dioxide conversion.

temperatures and pressures. Under these conditions, $CO_2$ fixation is a net producer rather than consumer of $CO_2$ due to the energy required to heat and pressurize the reactor and reactants. [20] These challenges explain why the current industrial usage of $CO_2$ is only 0.5% of the 24Gt/yr total anthropogenic $CO_2$ we produce.[1] This obvious gap has led many researchers to investigate ways to improve the $CO_2$ fixation process. Since the rate of any chemical process can be increased in theory by utilizing a catalyst, we will next explore why a good catalyst has not been found for $CO_2$ conversion processes.

## 1.2 Introduction: Sabatier's Principle and Dynamically Tunable Catalysis

Efficient solid state catalysis requires materials that can facilitate both the adsorption of reactants and the desorption of products. However, for the same static surface,

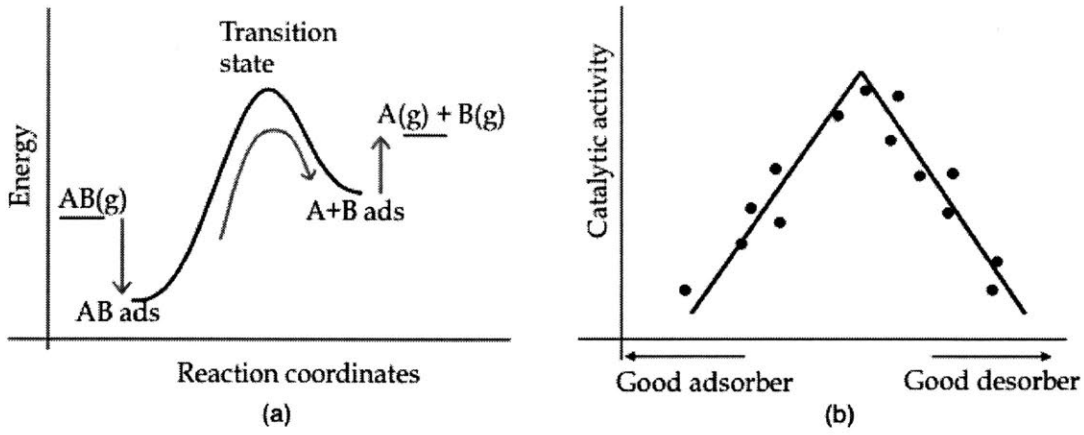


Figure 1-5: Sabatier's principle illustration. In (a), the arrows show the pathway for the dissociation of a gas AB to mono-atomic gases A and B. Fig. (b) illustrates the volcano plot of the catalytic activity versus interaction for a class of materials. The points on the graph represent different materials/surfaces for the same reaction and reaction conditions.

strong binding of the reactants, which leads to a fast first step is generally correlated with strong binding of the products, leading to a slow last step - see Fig. 1-5(a). Since the rate of the reaction is determined by the slowest step, the best catalyst for a given reaction for a given class of materials will have an intermediate level of interaction with reactant, intermediate, and product species. This principle, known as Sabatier's principle, is illustrated by the schematic "volcano plot" in Fig. 1-5(b). Based on this conception, the goal of most catalysis research is to find the least expensive material that is as close as possible to the top of the volcano. [21, 22, 23]

The key objective of tunable catalysis is to combine the advantages of both strong and weak interactions with the various species involved in a reaction in order to overcome Sabatier's principle and obtain rates that are better than those accessible by simply compromising on the catalyst-species interactions. This is illustrated in Fig. 1-6, in which the gas dissociation process $AB \longrightarrow A^{+}B$ is carried out in two steps, each at different states of the catalyst. In the illustration, the adsorption of the gas AB(g) and the dissociation to adsorbed A and B species on the surface of the catalyst all take place at the same surface state. Then another state of the catalyst is induced. This state is assumed to be more favorable for the desorption of gases

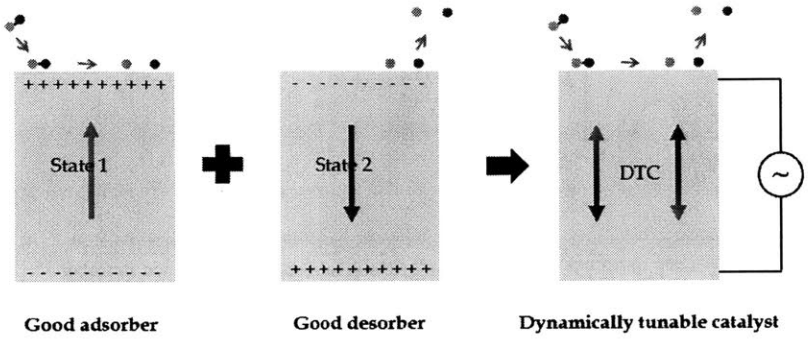


Figure 1-6: Tunable catalysis illustration. Changing the surface chemistry of a catalyst to achieve varied surface states for the dissociation of gas AB to gases A and B.

A(g) and B(g). Fig. 1-7 shows how switching between the reaction pathways that occur on two different states of a catalyst can lead to faster reaction rates (higher catalytic activity), shifting the activity of the tunable catalyst above the top of the volcano curve, which is not accessible to a static catalyst. The varied state of the catalyst could be achieved in a number of different ways, for example, by applying a cyclic electric field across a ferroelectric such as a perovskite, which is the focus of this work, or by temperature modulation.

## 1.3 Objectives of this thesis

To design a tunable catalysis system for a specific reaction, it is necessary to consider the following:

1. The material of the ferroelectric substrate.
2. The material of the film.
3. The orientation of the film.
4. Strain level in the substrate and/or film.

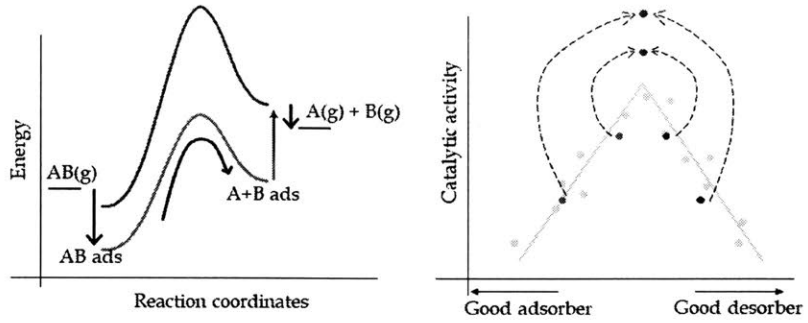


Figure 1-7: Tunable catalysis illustration. In (a), the arrows show the pathway for the dissociation of a gas AB to mono-atomic gases A and B. The adsorption of AB and dissociation to adsorbed A and B take place on one state of the catalyst (red lines) and the desorption of the product takes place at the other state of the catalyst (blue lines). Fig. (b) illustrates the expectation that the activity of the reaction on a tunable catalyst should be higher than the top of the static catalysis volcano.

5. Interface structure.

6. Environmental conditions.

Given such a rich parameter space, there is a lot of research to be done to fully understand tunable catalysis. As we will show in the next chapter, researchers simply select one point in this space and focus on the application of the selected catalyst to *potentially* promote a selected reaction. The knowledge gaps inevitably created by this approach inspired our work. In this thesis, we seek to answer the following questions:

1. What is the mechanism for the changing surface chemistry in a material (the film) when there is an underlying ferroelectric substrate?

2. Is there any limit to the thickness of the film for tunable catalysis to be possible?

3. What are the necessary conditions for tunable catalysis to be possible?

4. How can we extend the influence of the substrate to enable tunable catalysis on thicker films?

5. Can we identify a useful figure of merit for tunable catalysis?

6. What are the guiding principles for material screening in tunable catalysis?

An additional goal of our work is to find possible applications of tunable catalysis to $CO_2$ conversion processes, so we select zinc oxide as the film material and will test all hypotheses using the $CO_2$ dissociation reaction, which is frequently the first step in $CO_2$ conversion processes. ZnO was selected because it is commonly used as a catalyst for the industrially and environmentally important CO and $CO_2$ conversion reactions, frequently in conjunction with a copper co-catalyst [24, 25]. We choose to study hetrostructures of epitaxial non-polar ZnO($11\bar{2}0$) and polar ZnO(0001) films on $PbTiO_3$, as similar systems have previously been grown experimentally [4].

This thesis is laid out as follows. This chapter introduces the work and our objectives. Chapter 2 is a literature review of tunable catalysis. Chapter 3 explains the methods used in this work: Density Functional Theory (DFT) and Micro-kinetic Modeling (MKM). In Chapter 4, we evaluate the effect of a $PbTiO_3$ substrate on the surface of thin-film non-polar ZnO. Chapter 5 explores the possibility of tunability of ZnO polar surfaces, which is in effect a quest to induce ferroelectricity in the material. We show that this is possible and calculate the energetic requirements. In Chapter 6, we explore the tunable catalysis of $CO_2$ reduction on supported ZnO surfaces. We show an important criterion for tunable catalysis to happen and discuss the extension of our results to other oxides. In Chapter 7, we show that tunable catalysis can be applied to more complex $CO_2$ reactions, including the synthesis of methanol and the addition of epoxides to $CO_2$ to form cyclic carbonates. We summarize the thesis in Chapter 8 and suggest follow-on research.

# Chapter 2

# Literature review of dynamically tunable catalysis

*Portions of this chapter were published in the author's master's dissertation [6].*

## 2.1 Introduction

Systematic analysis of tunable catalysis has only recently begun: so far, only three groups have published any work on it in the past 10 years. In 2007, Kolpak *et al.* [3] showed that the surface chemistry of Pt can be tuned by growing a thin layer on a ferroelectric. However, the applicability of the proposed $Pt/PbTiO_3$ catalyst is limited because such thin layers of metal agglomerate rather than form thin films on oxides [26]. Therefore, other researchers have looked into the use of oxides as the active catalyst instead. Lee and Selloni [27] showed that polarization of the perovskite subtrate determined whether or not the reaction efficiency for the oxygen evolution reaction was improved on $TiO_2/SrTiO_3$. Kakekhani and Ismaili-Beigi [28] proposed a NO dissociation mechanism on electric field-actuated tunable $CrO_2/PbTiO_3$ catalyst. Later, they also proposed that temperature actuation is possible for $H_2O$ dissociation on $PbTiO_3$ [29]. In this chapter, we will examine these and related papers and the foundations of polarization-influenced catalysis. We will particularly focus on research on materials that are appropriate for dynamically (real-time) tunable catalysis.

## 2.2 Ferroelectric materials as catalysts - early research

The direction of the ferroelectric polarization has been demonstrated to have an effect on the surface chemistry of ferroelectrics. The first to demonstrate this for a ferroelectric was Parravano in the early 1950s who showed that the rate of CO oxidation over $KNbO_3$ and $NaNbO_3$ significantly increased around the Curie temperatures of the catalysts [30]. In the 1960s, it was demonstrated by Stadler and co-workers that feooelectric polarization of a substrate can influence the physical properties of a supported metal films [31, 32]. Inoue and co-workers *et al.* extended this result in the 1980s by studying the chemical properties of the surface of palladium supported on $LiNbO_3$ [33, 34]. They found that the oxidation rate of CO over the negatively poled structure was higher than on the positively poled structure. Also, in the 1980s, some work was done on the chemical properties of the surfaces of polar ZnO, which has polarization perpendicular to the surface, but this polarization is not reversible. By using temperature programmed desorption (TPD) measurements, Vohs and co-workers studied the adsorption and/or decomposition of formaldehyde, ethanol, 1-propanol, acetic acid and formic acid on the positively polarized Zn-terminated ZnO surface and the negatively polarized O-terminated surface [35, 36, 37]. They found that the Zn-termination is reactive to all the species but the O-termination is not. This insight will be shown to be important later in this thesis.

## 2.3 Tunable catalysis on bare perovskites

The simplest dynamically tunable catalysis scheme utilizes the different surface chemistries on the surfaces of perovskites. The necessary electronic and structural reconstructions [38, 39, 40, 41] on both the positive and negatively polarized perovskite surfaces account for the change in surface chemistry upon polarization switching. The reconstructions are mostly due to the need to constrain the divergence of the internal electric field with increasing thickness of the slab.

An experimental study of catalysis on bare ferroelectric surfaces is that of Yun and co-workers. They measured the TPD data for different kinds of molecules and showed that 2-propanol has a desorption peak temperature 100K greater on the negatively polarized surface compared to the positively polarized one [42]. This means that the adsorption energy is much greater on the negatively polarized surface.

The internal electric field in ferroelectric catalysts and the polar surface terminations can mitigate electron-hole recombinations when used for the photocatalysis and this has resulted in several studies on the possibilities of using ferroelectrics as solar cell materials and photocatalysts [43]. Another interesting catalytic application of bare ferroelectrics such as $BaTiO_3$ and $PbTiO_3$ is the combustion of methane[44]. An exciting phenomenon on these materials for hydrocarbon-related catalysis is the difference in adsorption properties of ethanol and methanol on oppositely poled surfaces. It was found that ethanol adsorbs more rapidly on negatively poled $BaTiO_3$ [45] in contrast to methanol which adsorbs more rapidly on positively poled $BaTiO_3$ [46]. This highlights the intriguing possibility of tuning the surface of the catalyst for selectivity towards methanol or ethanol.

However, the picture is not all-rosy for the case of dynamically tunable catalysis. Several researchers have attempted to use the quite different surface chemistries at the different polarization states of the perovksite catalyst to experimentally design dynamically tunable catalysts. Some of the work includes $BaTiO_3$ and $SrTiO_3$ tunable catalysts for $H_2O$ adsorption [47], $H_2O$ dissociation [2, 48] and CO oxidation [49]. It is found that the progression of the surface adsorption or reaction significantly screens the polarization, degrades the surface or pins the polarization of the ferroelectric slab. Through first principles calculations, it is shown that the polarization pinning is caused by the formation of oxygen vacancies which stabilizes an inward pointing polarization [50]. In effect, the progression of the tuned catalysis on the surface of the catalyst itself degrades the catalyst. An example of this phenomenon is shown in Fig. 2-1, adapted from Ref. [2] which clearly shows the degradation of the ferroelectricity in barium titanate (BTO) when the surface is treated with water. Therefore, bare surfaces of perovskites are ineffective as tunable catalysts.

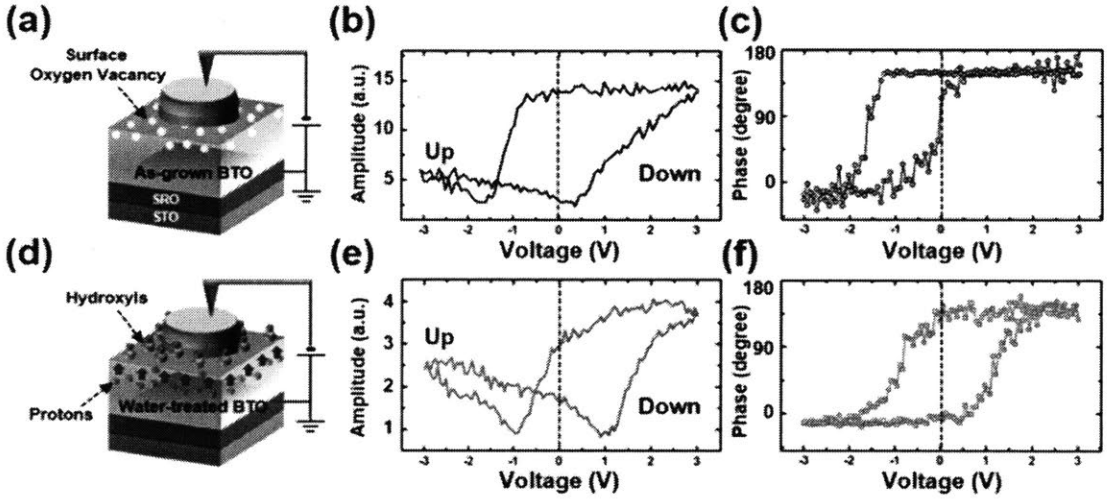


Figure 2-1: (a) Schematics showing the as-grown BTO thin film. Au/Co was used as the top metal electrodes. (b) Piezoresponse Force Microscopy (PFM) amplitude and (c) phase hysteresis loops measured in the structure. (d) Schematics showing the structure based on a water-treated BTO thin film. The chemically induced surface polarization in the top passive layer is depicted by blue arrows. Panels e and f show its PFM amplitude and phase signals, respectively. Adapted from Ref. [2].

## 2.4 Tunable catalysis on perovskite-supported metal films

Since it has been shown by Inoue and co-workers [34] that the tunable catalysis effects are maintained on ferroelectrics even when a thin metal film is grown over them, researchers turned towards this system for inspiration. Inoue and co-workers reported that activation energy (hence kinetic behavior) for CO oxidation over a $LiNbO_3$-supported Pd catalyst significantly changed depending on the polarization of the support and the thickness of the Pb layer. They found that the energy barrier varied over Pd on the positive polar surface changed from 126KJ/mol when the Pd thickness was over 0.2nm to 96KJ/mol at 0.02nm, whereas the Pd deposited on the negatively poled surface showed a constant energy barrier of 128KJ/mol irrespective of thickness. They also showed that the adsorption energy of CO and $H_2$ on NiO deposited on oppositely poled directions of $LiNbO_3$ [33]. This phenomenon was explained using a band bending model in which the polarization of the substrate modifies the electronic distribution on the NiO surface.

Other researchers have also shown similar results. In 1990, Roberts and co-workers carried out CO adsorption on ZnO-supported Pt films [51]. Depending on the polarization direction of the ZnO support, the adsorption energy of CO (determined via a TPD characterization) is greater when the support is positively polarized than when it is negatively polarized. Yun *et al.* [52] also carried out CO adsorption via TPD but this time on Pd *clusters* supported on $LiNbO_3$. Their results showed no difference in adsorption properties of the molecule when the polarization direction is different. This suggests that the surface chemistry on supported metal structures depends on the thickness of the film.

Based on this idea, Kolpak and co-workers carried out theoretical research on the surface chemistry of Pt layers deposited on oppositely poled $PbTiO_3$. Their results showed different chemisorption strength and site preference for the adsorption of CO, O, C, and N, altering the reaction pathways for the dissociation of CO, $O_2$, $N_2$ and NO, but this difference is significant only for very thin Pt films (1-2 layers) [3] - see Fig.

2-2, in agreement with the experimental results discussed in the last paragraph. The researchers explained that the polarization-induced changes in the surface chemistry effects are mitigated by the small electronic screening length of Pt, so that only atomically thick films exhibit significant effects. Since it is also challenging to wet oxide surfaces with catalytically active transition metals [26], manufacturing reliable pervoskite supported catalysts will be a significant engineering challenge, thus we expect that the aggregation of the metal into nanoparticles will supress the effects of substrate polarization on catalytic activity in real catalysts of this design.

## 2.5 Tunable catalysis on perovskite-supported oxide films

Recently, researchers have begun explore the possiblity of replacing metals in the supported tunable catalysis schemes as described above, with binary oxides. This removes the surface degradation effects on the bare ferroelectric and the coagulation effects of metallic films on the perovskite support. Moreover, consistent thin films of oxides have been reported grown experimentally on perovskites (e.g Ref. [4]) through advances in epitaxial growth methods such as Atomic Layer Deposition [53] and Molecular Beam Epitaxy [54]. We now report on recent research on binary oxide-perovskite heterostructures.

Inoue and co-workers [55] studied $H_2$ and $O_2$ adsorption on $LiNbO_3$-supported $TiO_2$ and NiO films respectively. On the supported $TiO_2$ film, the adsorption energy of $H_2$ was 0.15 eV higher on the positively polarized structure. On the otherhand, for $O_2$ adsorption on the supported NiO film, the higher adsorption energy, by 0.57 eV, was observed on the negatively polarized structure. A few decades later, they showed that varying the polarization of the $LiNbO_3$ support influenced the surface chemistry of NiO enough for them to obtain four to seven times increase in oxidation rates of CO, when compared to the oxidation on a static structure [56]. This was the first clear case of dynamically tunablel catalysis in an experiment.

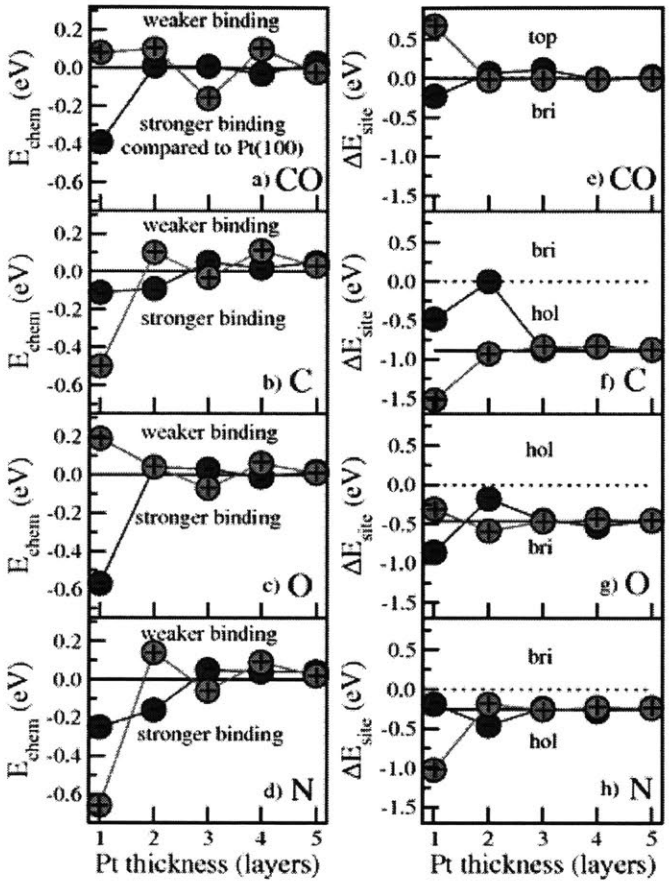


Figure 2-2: (a)âĂŞ(d) Chemisorption energies $E_{\text{chem}}$ for CO, O, C, and N as a function of polarization direction and Pt thickness for the PbO/Pt interfaces. Red plus signs indicate the P+ interface, and blue minus signs represent the P- interface. The zero of energy corresponds to $E_{\text{chem}}$ on unsupported Pt(100). (e)âĂŞ(h) Site-preference energies $E_{\text{site}}$ for CO, O, C, and N. The solid black lines give $E_{\text{site}}$ for the adsorbates on unsupported Pt(100). Points above the dotted lines represent a change in the preferred bonding site relative to Pt(100). Adapted from Ref. [3].

Theoretical work support the conclusions from the experimental studies. In 2013, Garrity and co-workers showed that the the binding energy of $O_2$ on the surface of $PbTiO_3$-supported $RuO_2$ is 1 eV greater on the positively polarized structure compared to the negatively polarized structure [57]. Two years later, the same research group showed that the binding energies of $NO_2$, NO, $O_2$, CO and $CO_2$ on $PbTiO_3$-supported $TiO_2$ were quite different on the positively and negatively polarized structures [28]. Lee and Selloni [27] explored the oxygen evolution reaction (OER) on epitaxial heterostructures of $TiO_2$ on polar SrTiO3 perovskite. They show that the reactivity of the $TiO_2$ surface is tuned by polarization of the substrate and also the extent of the reaction. Compared to the OER on unsupported $TiO_2$, the positively poled surface reduced the thermodynamic barriers and significantly improve the efficiency of the OER reaction. This is similar to the result obtained by Kakekhani and Ismail-Beigi [28] for $NO_x$ decomposition and CO oxidation on $CrO_2/PbTiO_3$. Their model required switching the polarization of the ferroelectric *in situ* by an electric field at roughly the turn-over frequency of the reaction. The same group later designed a catalytic cycle for water splitting that is actuated by cyclic temperature modulation [29].

## 2.6 Summary

We have examined the history of tunable catalysis and showed the recent advances in the field. We explored the catalytic activities on bare ferroelectric surfaces, ferroelectric-supported metal surfaces and ferroelectric-supported oxide surfaces. We see that the polarization of the ferroelectric support in each case affects the adsorption energy and reaction rate of several types of molecules and reactions. The parameter space for the exploration of tunable catalysis is rich, and so far, the approach by researchers has been to select an arbitrary point in the rich parameter space that represent tunable catalysis. This is sub-optimal, and we know that adding a predictive theory for static surface catalysis based on the d-band model and Bronsted-Evans-Polanyi relations [58, 59] led to significant advances in the development of new catalysts. This calls for

a more systematic approach to understanding and designing tunable catalysts. This thesis aims to fill this gap.

# Chapter 3

# Methods

*Portions of this chapter were published in a previous work [6].*

### 3.0.1 Design of the dynamically tunable catalyst

As discussed in Chapter 1, tunable catalysis is necessary to obtain catalytic rates beyond the limitations of Sabatier's principle. One way to achieve this is to perform catalysis on the surface of a perovskite tuned by a constantly changing electric field. As discussed in Chapter 2, this approach is not practical, as the participation of the atoms of the catalyst quickly degrades the ferroelectric properties of the material. Our catalyst is designed to have the strong difference in surface chemistry induced by a perovskite but without the reaction taking place on its surface. This is achieved by the epitaxial growth of a thin film of an oxide on the surface of the perovskite. This scheme is illustrated in Fig. 3-1. Lead titanate ($PbTiO_3$) is chosen as Component 1, and zinc oxide (ZnO) is chosen as component 2. Since both of these materials are earth-abundant, the catalyst is expected to be both effective and cheap if our work is successful.

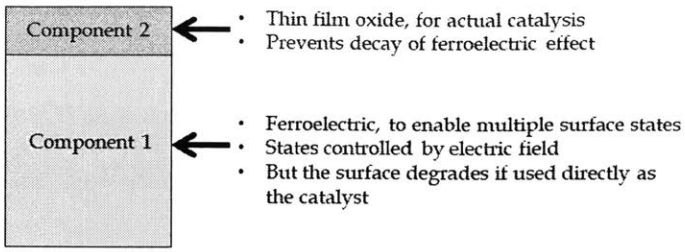


Figure 3-1: Tunable catalyst design

## 3.1 Materials modeling

In this dissertation, we build material, electrostatic and reaction models of the tunable catalyst (as described in Chapter 1 and the previous section) to simulate its performance for carbon dioxide conversion. In this section, we discuss in general terms, the modeling of materials.

In the early 20's materials were modeled by simple spring-like pair potentials holding together atoms in a specified lattice. The holy grail of this method was to figure out the best interatomic potentials for certain systems and improvement of computational times. Lennard-Jones model [60], force-field potentials (e.g Ref. [61]), embedded atom model [62] and the more recent Morse potential [63] were among the most successful approaches. The methods were able to reproduce bulk properties of the materials including lattice constants, bulk modulus, crack propagation, etc and are used in molecular mechanics and dynamics simulations. However, these methods failed when applied to process which had significant involvement of electrons or had changing or complicated potential fields such as in bond-breaking, solid diffusion, epitaxy and chemical reactions.

Gradual developments in Computational Quantum Chemistry beginning in the late 30's eventually solved this problem. Schrodinger's equation (Equation 3.1), a linear partial differential equation which accurately models the behavior of quantum systems, is the starting point for these methods. [64]

$$E\Psi(\mathbf{r}) = \left[\frac{-\hbar^2}{2m}\nabla^2 + V(\mathbf{r})\right]\Psi(\mathbf{r}) \tag{3.1}$$

where $E$ is the total energy in the quantum system (collection of atoms, molecules or fundamental particles), $\Psi(\mathbf{r})$ is the wavefunction (a probability amplitude whose square is the probability density) at a point $\mathbf{r}$, $\hbar$ is the reduced Planck's constant, $m$ is the mass, $\nabla^2$ is the Laplacian and $V(\mathbf{r})$ is the potential energy.

Erwin Schrodinger showed that this equation can be exactly solved for the hydrogen atom. He was able to reproduce the experimental hydrogen spectral series and the energy levels of the Bohr model. However, the equation becomes quickly complicated when more electrons are introduced, per modeling of heavier elements. The many-body Schrodinger Equation,

$$E\Psi = \left[\sum_{i}^{N} \frac{-\hbar^2}{2m_i}\nabla_i^2 + \sum_{i}^{N} V(\mathbf{r}_i) + \sum_{i<j}^{N} U(\mathbf{r}_i, \mathbf{r}_j)\right] \Psi \tag{3.2}$$

where $U(\mathbf{r}_i, \mathbf{r}_j)$ is the interaction energy between electrons $i$ and $j$ becomes complicated for more than one electron.

Methods to solve this equation include Pertubation theory, the variational method, Quantum Monte Carlo, the Wentzel-Kramers-Brillouin (WKB) approximation, the Hartree Fock Method and Density Functional Theory (DFT) method. Of all the listed methods, Density Functional Theory is the most widely used because it provides a way to solve the Schrodinger equation with reasonable computational cost which scales well with system size without sacrificing too much accuracy. We briefly describe the development of DFT next.

## 3.2 Density Functional Theory

Density Functional Theory is a computational method used to calculate the ground state properties of many body systems. It is an implementation of the Schrodinger equation with appropriate approximations that promotes accuracy at reasonable computational costs. DFT approaches the difficult-to-solve interacting electrons problem by mapping it exactly to the easier-to-solve non-interacting electrons problem. The

computational tractability comes from using functionals of the electron density rather than direct calculation of the wavefunctions.

The step that signaled the birth of DFT was the formulation of the two Hohenberg-Kohn (H-K) theorems [65] in 1964. The first H-K theorem proved that the ground-state properties of a many-body electron system are uniquely determined by the electron density that depends on the three spatial coordinates $x$, $y$ and $z$. This makes it possible to reduce the problem of solving the N-electron Schrodinger equation having 3N coordinates to that of solving the N-electron equation having 3 coordinates. To prove the one-to-one mapping between the ground state wavefunction and density, Hohenberg and Kohn used the variational principle: that the expectation value of the Hamiltonian $H$ obtained with the true ground state wavefunction must be less that that obtained with any other wavefunction. We have, for two wavefunctions $\Psi$ and $\Psi$':

$$E_o = \langle \Psi | H | \Psi \rangle \tag{3.3}$$

and

$$E_o' = \langle \Psi' | H' | \Psi' \rangle \tag{3.4}$$

By the variational principle,

$$E_o < \langle \Psi' | H | \Psi' \rangle \tag{3.5}$$

and

$$E_o' > \langle \Psi | H' | \Psi \rangle \tag{3.6}$$

Equations 6.1 and 3.6 can be rewritten as

$$E_o < E_o' + \langle \Psi' | H - H' | \Psi' \rangle \tag{3.7}$$

and

$$E_o' < E_o + \langle \Psi | H' - H | \Psi \rangle \tag{3.8}$$

In real space, $\langle \Psi' | H - H' | \Psi' \rangle = \int \rho_o (V - V') d\mathbf{r}$ and $\langle \Psi' | H - H' | \Psi' \rangle = \int \rho_o (V' - V) d\mathbf{r}$ if we assume $\Psi$ and $\Psi'$ to give the same ground state density $\rho_o$. Therefore if wall of quantum chemistrye sum Equations 6.2 and 6.3, we obtain:

$$E_o + E_o' < E_o + E_o' \tag{3.9}$$

The falseness of Equation 6.4 shows that $\Psi$ and $\Psi'$ cannot give the same ground state density $\rho_o$.

The second H-K theorem defines an energy functional and proves that the correct ground state electron density minimizes this functional. Kohn and Sham[66] in 1965 combined these two theorems to develop a method of finding the ground state energy from the electron density. They showed that the energy can be written as the sum of the kinetic energy of a non-interacting electron gas, energy from an external potential, an Hartree energy and an exchange-correlation energy, viz:

$$E = T + V_{ion}(\mathbf{r})\rho(\mathbf{r})d\mathbf{r} + \frac{e^2}{2}\int \frac{\rho(\mathbf{r})\rho(\mathbf{r}')}{|r - r'|} d\mathbf{r} d\mathbf{r}' + E_{XC} \tag{3.10}$$

The exchange correlation part of the energy is however not known and various approximations are employed. In addition, we need to find the density in order to use the above expression. Kohn and Sham's idea to obtain these is depicted in Fig 3-2. The steps in the DFT scheme are:

1. Construct the nuclear potential given the atomic types and positions in the system.

2. Calculate the Hartree and exchange correlation potentials.

3. Solve the Kohn-Sham equations to obtain the wavefunctions.

4. Use the new wavefunctions to calculate updated values of the spatial electron densities and the total energy.

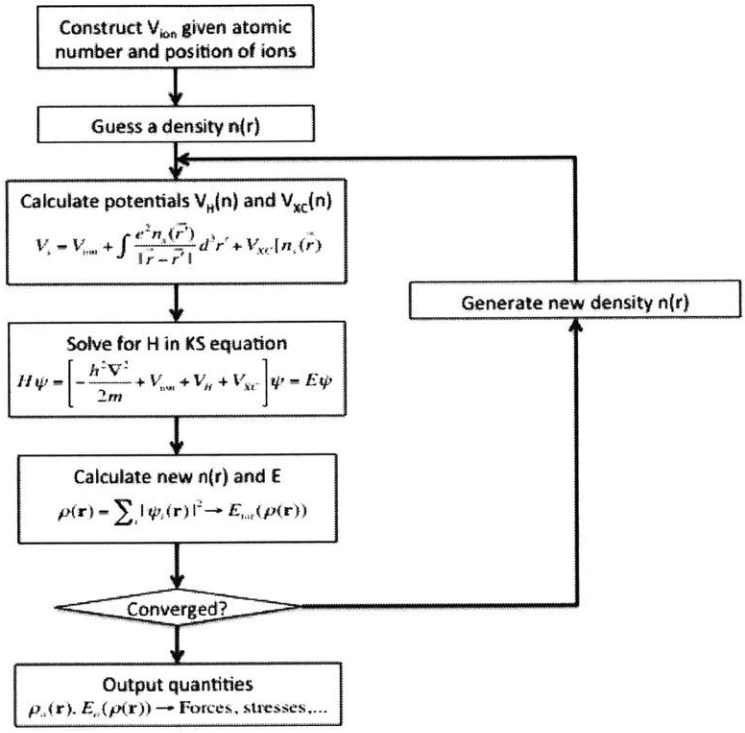


Figure 3-2: DFT self-consistency scheme.

5. Stop the self-consistent field calculation when the difference between the old and new energies are sufficiently small. If only the ground state energy and density of the system are required, the calculation should end here.

6. If calculating the optimized atomic positions of the atoms in the system, also calculate the forces on each atom in step 4. Move the atoms based on the magnitudes and directions of the forces and calculate the new electronic densities and forces. Repeat this until the forces are almost zero.

7. If calculating the optimized lattice parameters and positions of the atoms, also calculate the forces on each atom and the stresses in the cell. Move the atoms and change the lattice parameters based on the forces and stresses respectively and calculate the new electronic densities, energies, forces and stresses. Repeat until the forces and stresses are sufficiently small.

A plane wave basis set is usually used to describe the Kohn-Sham orbitals (wavefunctions) of Equation 3.2. Though other functions are possible, plane waves are the most commonly used to to their simple mathematical nature and that they allow a high numerical accuracy. Plane waves are written as:

$$\psi_i(\mathbf{r}) = \sum_{\mathrm{G<G_c}} \mathrm{C_i e^{iG.r}} e^{i\mathbf{k}.\mathbf{r}} \tag{3.11}$$

### 3.2.1 Exchange Correlation Functionals

A compromise in the computational tractability in the DFT method is having to approximate the electron-electron exchange correlation energy $E_{XC}$ in Equation 3.10 since we do not know its analytical form. The simplest possible approximation of $E_{XC}$ is the local density approximation (LDA) developed by Kohn and Sham. [67]. Here the exchange-correlation energy functional depends solely on the values of the electron density and not on its derivatives.The functional is written as

$$E_{XC}^{LDA}(\rho) = \int \rho(\mathbf{r})\epsilon_{XC}(\rho)\mathrm{d}\mathbf{r} \tag{3.12}$$

where $\epsilon_{XC}$ is the exchange-correlation energy of a homogenous electron gas (a quantum mechanical model of interacting electrons in a field of uniformly distributed positively charged nuclei) with charge density $\rho$. In this approximation, the correlation energy is treated as purely local.

When it is necessary to include spin polarization in the system being modeled, the local spin density approximation (LSDA) performs better than the LDA. Here two spin densities $\rho_\alpha$ and $\rho_\beta$ representing up and down directions respectively are employed, where the total density $\rho$ is $\rho_\alpha + \rho_\beta$. The form of the LSDA is

$$E_{XC}^{LSDA}(\rho_\alpha, \rho_\beta) = \int \rho(\mathbf{r})\epsilon_{XC}(\rho_\alpha, \rho_\beta)\mathrm{d}\mathbf{r} \tag{3.13}$$

From the foregoing, it is clear that the LSDA and LDA will be most accurate when the density changes slowly with position. When this is not the case, it is better to include nth-order variations in the density. A logical first improvement on the LDA is the generalized gradient approximation (GGA) which takes into account the gradient of the electron density at each position. That is, the exchange-correlation energy is written as a function of both $\rho$ and $\nabla\rho$, viz

$$E_{XC}^{GGA}(\rho_\alpha, \rho_\beta) = \int \rho(\mathbf{r})\epsilon_{XC}(\rho_\alpha, \rho_\beta, \nabla\rho_\alpha, \nabla\rho_\beta)\mathrm{d}\mathbf{r} \tag{3.14}$$

This improves the accuracy of many types of calculations. Further improvement can be achieved by including higher derivatives of the density but the improved accuracy comes at a disproportionate computational cost. Therefore in this work, the generalized gradient approximation will be employed.

### 3.2.2 Pseudopotentials

The pseupotential method replaces the complicated behavior of the core electrons and nucleus of each atom with an effective potential. Since the core of the atoms (compared to the valence electrons) are not involved in the bonding properties of the

atoms in the system, approximating the effect of the core by some potential should reduce the computational cost of DFT calculations even further without significant effects on accuracy when optimized for the problem at hand. The highly localized core orbitals, which are normally sharp functions mathematically represented by a large number of plane waves, are replaced with a smoother function so that the electrons in the orbitals are not treated explicitly in the calculation.

A pseudopotential is constructed by first performing an all-electron calculation to determine the potential, wavefunctions and eigenvalues of the atomic reference state. The pseudo-potential is then chosen such that the eigenvalues match that of the reference state and the wavefunction outside some cut-off radius $r_c$ exactly matches that of the reference.

The most common forms of pseudopotentials are the norm-conserving [68] and the ultrasoft [69]. In this dissertation, we will use pseudopotentials of the later type which are less computationally expensive.

### 3.2.3 Dispersion Correction (DFT-D)

Density Functional Theory is yet unable to properly describe intermolecular interactions, especially van der Waal's forces. New DFT methods have been developed to overcome this problem. Among these, the Grimme dispersion correction [70] is the most widely used since it can easily be incorporated as a correction on existing functionals and so does not significantly affect the other properties for which the functional was designed.

For the dispersion correction, the parametrization of the density functional is restricted to short electron correlation ranges and longer ranges are described by damped $C_6 \cdot R$ terms. This correction is added to the usual Kohn-Sham energy, viz:

$$E_{DFT-D} = E_{KS-DFT} + E_{disp} \tag{3.15}$$

The dispersion energy $E_{disp}$ is given by

$$E_{disp} = -s_6 \sum_{i=1}^{N_{at}-1} \sum_{j=i+1}^{N_{at}-1} \frac{C_6^{ij}}{R_{ij}^6} f_{damp}(R_{ij}) \tag{3.16}$$

where $N_{at}$ is the number of atoms in the system, $C_6^{ij}$ and $R_{ij}$ are the dispersion coefficient and interatomic distances for the pair $ij$, $f_{dmp}$ is a damping function and $s_6$ is a functional-dependent global scaling factor. This method has been found to be very successful. Several studies have shown that the performance for non-covalently bound systems including many pure van der Waals complexes is exceptionally good, reaching on the average the level of accuracy of quantum chemistry (e.g CCSD(T)) methods.[71, 72]

### 3.2.4 Density of States

The density of (energy) states describe the number of states available for electron occupation at each energy interval in a system. It is frequently of interest to know the density of states in a system since it provides a key insight into the material's properties, for example, its band gap, electronic effects due to an interface, metallicity, etc. We can also infer or predict bonding interactions between molecules or between a molecule and a surface.

The density of states in a DFT calculation can be computed when the ground state charge density is known. It is formally defined as

$$n(\epsilon) = \int n(\mathbf{r}, \epsilon) d\mathbf{r} \tag{3.17}$$

where the local density of states, $n(\mathbf{r}, \epsilon)$ is defined as

$$n(\mathbf{r}, \epsilon) = \sum_{i}^{N} |\psi_i(r)|^2 \delta(\epsilon - \epsilon_i) \tag{3.18}$$

### 3.2.5 Nudged Elastic Band Calculations

The Nudged Elastic Band (NEB) is a method of calculating the energetics of chemical processes including chemical reactions, solid diffusion, adsorption and desorption and

vacancy formation. The rates of these reactions are estimated by finding the transition states between the initial and final states using the harmonic transition state theory[73]. The minimum energy path (along which the reaction energetics are calculated) is defined as the path that has the greatest statistical weight on the potential energy surface. At any point along this path, the force of the atoms is tangential to the path.

The NEB method is one of the most robust ways of finding the minimum energy path (MEP) and has been used in conjunction with classical potentials and density functional theory. [74] In the method, images of the system between the initial and final states are constructed and 'rubber-bands' are added to adjacent images. Minimizing the force on these bands results in a path that is the MEP.

Consider a system having $N+1$ images including the start and end states, resulting in the use of $N$ bands $[R_0, R_1, R_2, ..., R_N]$ with $R_0$ and $R_N$ fixed. The total force acting on an image is the sum of the forces in the elastic bands along the local tangent a 'true' force perpendicular to it.

$$F_i = F_i^s|_{||} - \nabla E(R_i)|_{\perp} \tag{3.19}$$

We then apply an optimization algorithm to move the images according to the magnitude of the force using for example a Verlet algorithm. From this, we can obtain a reaction or process pathway and hence reaction rates for any system.

### 3.2.6 Limitations of DFT

Even though DFT is in principle an exact reformulation of the many body Schrodinger Equation, approximations are required for the exchange-correlation energy functional. The error in the correlation part results in the local nature of LDA and GGA type functionals. This has been found to explain why common DFT methods tend to underestimate the band gaps of materials, barriers of chemical reactions, dissociation energies of ions and charge transfer ionization energies, and overestimate the bind-

ing energies of charge transfer complexes and material behavior under the action of electric fields. [75] Several methods have been devised to correct these errors. The DFT-D method [70] accounts for long range interactions using a $1/R^6$ correction term and the DFT+U adds an on-site Coulomb repulsion to (usually localized $d$ and $f$) orbitals of specified atoms so as to correctly account for electron-electron interactions. Understanding the limitations (and possible remedies) of DFT is important in evaluating the results and comparing to experiments.

## 3.3 From DFT to reaction rates: microkinetic modeling of heterogenous catalysis

Through a robust body of work in the literature (e.g Refs. [76, 77, 78, 79, 80]), it has been shown that it is possible to correlate the energetics of elementary steps of a reaction to the macroscopic rates and yields of the final products in a reactor. First principles calculations are used to build kinetic models and give a better understanding of reaction mechanisms. The scheme for this process is shown in Fig. 3-3

### 3.3.1 Thermodynamics

After determining a pathway or set of possible pathways, one calculates the total energies of species and their absorbed species on the catalyst surface. The binding energy of each species is given by

$$E_B^X = E_T^{X*} - E_T^* \tag{3.20}$$

where X is the molecule and * represents the energy of the slab. $E_B$ and $E_T$ are the binding and total energies respectively.

The heat of reaction, $\Delta H$ is given by

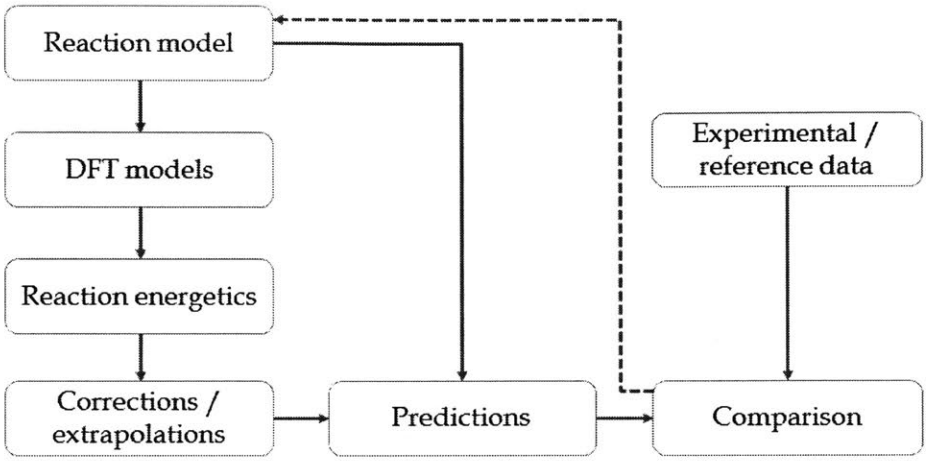


Figure 3-3: Microkinetic modeling scheme

$$\Delta H = \sum_{i=1}^{n} E_B^{products} - \sum_{i=1}^{m} E_B^{reactants} + \Delta H_{gas} \tag{3.21}$$

where $n$ and $m$ are the number of product and reactant species respectively. $\Delta H_{gas}$ is the heat of the reaction in the gas phase.

The activation energy $E_a$ is given by

$$E_a = E_B^{trans*} - \sum_{i=1}^{m} E_B^{reactants*} \tag{3.22}$$

where $trans*$ and $reactants*$ represent the total energies of the transition and initial states of the species for that reaction step. The transition state is usually calculated in DFT using the nudged elastic bank (NEB) method [74].

The rate of the forward or reverse reaction for an elementary step is now given by

$$r = A_0 \exp\left(-E_a/k_B T\right) \prod_{i=1}^{n} a_i^{x_i} \tag{3.23}$$

where $A_0$, $E_a$, $k_B$ and $T$ are the frequency factor, activation energy, Boltzmann constant and reaction temperature respectively. $a_i$ and $x_i$ are the activity and stoichiometric coefficient respectively of the $i$th specie. $A_0$ can be determined from transition state theory [81] which requires the calculation of the vibrational modes of the transition state using DFT.

### 3.3.2 Thermodynamic corrections

The ground state energy calculated from DFT assumed no temperature effects and ignores the error due to the classical nature of the Born-Oppenheimer potential energy surface. The latter is corrected by calculating the zero point energy using the harmonic oscillator approximation. This energy is given by

$$ZPVE = \sum_{i}^{modes} \frac{1}{2} h w_i \tag{3.24}$$

where $h$ is the Planck constant and $w_i$'s are the vibrational frequencies of the molecule.

For temperatures that are greater than 0 K, entropy contributes to the energy. There are translational, rotational and vibrational contributions to the entropy. The formula for these contributions can be found in standard textbooks.

### 3.3.3 Approximations for modeling reaction rates

The formula for the overall rate of reaction depends on the approximation we choose. Where it is reasonable to assume that a particular elementary step is rate-limiting, the rate of all other steps is assumed to be zero. This greatly simplifies the calculation of the coverages. The overall rate of reaction in this case is the rate of progression of the rate limiting step. This is the quasi-equilibrium approximation (QEA).

Where the rate limiting step is unknown, the steady state approximation (SSA) is used. In the SSA, it is assumed that there is no accumulation of any adsorbed species. This means the sum of the rates of production of an adsorbate is equal to

the sum of the rates of consumption of the adsorbate. The rate of reaction is the net rate of reaction of the elementary step(s) that leads to the production of the desired product. Solving the equations that result from the steady state approximation is more involved but should lead to more accurate results.

## 3.4 Conclusion

This chapter introduced the methods we employ in this dissertation. A short introduction to the mostly widely used computational method for materials, the Density Functional Theory, is presented. The self consistent scheme for the implementation is described and the meanings of functionals and pseupotentials are explained. Some of the methods for calculating material properties (e.g Density of States) or improving DFT (e.g DFT-D) are also presented and the general limitations of DFT are discussed. Finally, we discuss the microkinetic modelling of chemical reactions.

# Chapter 4

# Evaluation of non-polar ZnO grown on $PbTiO_3$ as a tunable catalyst for $CO_2$ conversion

*A version of this chapter was published in a previous work [82].*

## 4.1 Introduction

Catalytic conversion of $CO_2$ into fuels or other materials that can be used on an industrial scale is an attractive alternative to expensive carbon capture and sequestration (CCS) methods currently under consideration. As CCS is only feasible when large quantities of $CO_2$ are generated, preferably close to a suitable geological formation [83], this option cannot be used to address the emissions sources with the greatest collective impact: vehicles and small industrial plants. In contrast, since $CO_2$ can be used a precursor for the synthesis of numerous, industrially relevant carbon based compounds, chemical sequestration approaches could in principle be tailored to smaller scale applications, with implementation costs offset by the production of value-added chemicals. Although conceptually appealing, chemical conversion approaches are challenging due to the exceptional stability of the $CO_2$ molecule. As a result, $CO_2$ conversion reactions are performed under energetically costly conditions

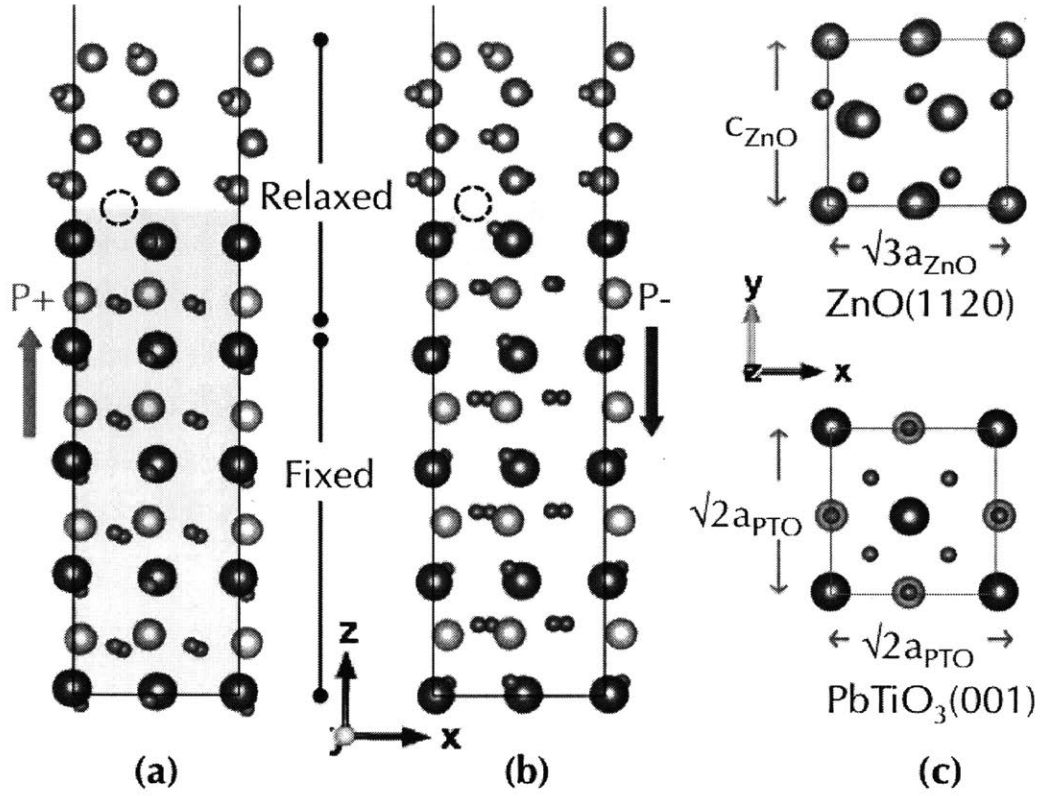


Figure 4-1: Computation supercell and relaxed atomic structure for (a) $ZnO(11\bar{2}0)_n/PbTiO_3\uparrow$ and (b) $ZnO(11\bar{2}0)_n/PbTiO_3\downarrow$ slabs for $n = 4$. The dashed circle represents the position for oxygen insertion at the interface. Fig. (c) shows the parameters and orientations for matching $ZnO(11\bar{2}0)$ to $PbTiO_3$. Grey, red, cyan, and black atoms are Zn, O, Ti, and Pb, respectively.

(i.e., high temperature and/or high pressure) that mitigate the effects of chemical sequestration; in fact, this can lead to some reactions being net carbon positive, generating more $CO_2$ than they consume [20]. In order to make chemical sequestration feasible, new catalysts that can operate under low temperature and pressure conditions need to be developed.

Various studies have shown that the polarization of a substrate can affect its surface properties [31, 30], and this effect has been applied to studies of molecular adsorption [84, 28, 85, 86] and the modulation of the carrier density in conductors [87]. Kolpak *et al.* suggested the possibility of using dynamical control of surface structure and reactivity in the coupling of ferroelectric $PbTiO_3$ with Pt [3]. Performing density

functional theory (DFT) computations of molecular and atomic adsorption to the surface of ultrathin Pt(100) films supported on ferroelectric $PbTiO_3$, they showed that switching the polarization direction of the substrate dramatically changes the chemisorption strength and site preference of CO, O, C, and N, potentially altering the reaction pathways for dissociation of CO, $O_2$, $N_2$ and NO. However, polarization-induced changes in the surface chemistry effects are mitigated by the small electronic screening length of Pt, so that only atomically thick films exhibit significant effects. Moreover, it is challenging to wet oxide surfaces with catalytically active transition metals [26]; thus, aggregation of the metal into nanoparticles is expected to supress the effects of substrate polarization on catalytic activity. In this work, we attempt to mitigate these challenges by considering the use of a ferroelectric substrate to tune the surface properties of thin films of an insulating catalytic oxide. In particular, we use DFT to investigate the surface chemistry of thin $ZnO(11\bar{2}0)$ films supported on ferroelectric $PbTiO_3$.

Zinc oxide is commonly used as a catalyst for the industrially and environmentally important CO and $CO_2$ conversion reactions, frequently in conjunction with a copper co-catalyst [24, 25]. Therefore the properties of the various ZnO surface terminations have been extensively studied [88, 89, 90, 91]. We choose to study the epitaxial interface of non-polar $ZnO(11\bar{2}0)$ films with $PbTiO_3$ (PTO), as similar systems have previously been grown. Wei *et. al.* [4] reported heteroepitaxial growth of $ZnO(11\bar{2}0)$ on $SrTiO_3(001)$ and $BaTiO_3(001)/SrTiO_3(001)$ surfaces, suggesting that $PbTiO_3(001)$, which has the same crystal structure and very similar in-plane lattice constant, will also provide an experimentally feasible substrate for $ZnO(11\bar{2}0)$ films. In the rest of this Letter, we use the notation $(ZnO)_n/PbTiO_3\uparrow$ and $(ZnO)_n/PbTiO_3\downarrow$ for $ZnO(11\bar{2}0)$ grown on positively polarized ("up") and negatively polarized ("down") $PbTiO_3(001)$ slabs, respectively, where $n$ is the number of $ZnO(11\bar{2}0)$ atomic layers.

## 4.2 Computational Methods.

### 4.2.1 Effect of adding an electrode.

An electrode or some kind of support is necessary for most applications involving perovskites. Electrodes have been demonstrated to have significant effects on the perovskite properties. For example, Sai *et al* [92] reported that the Pt electrodes cancel 97% of the depolarizing field in thin $PbTiO_3$ thin films and thus help to maintain some polarization even in films one lattice unit thick. The grounded electrodes provides metallic screening that compensates the polarization charge. Arras *et al.* [93] carried out an interesting study on the effects of metal electrodes on the $LaAlO_3/SrTiO_3$ interface. They showed that changing the type of metal greatly affects the Schottky barrier, carrier concentration and lattice polarization at the interface.

In the light of these, it is imperative to understand how adding a metal electrode in our model of the $ZnO/PbTiO_3$ affects the ZnO surface (hence catalytic) properties. If the electrode has an effect, we will have a better understanding of phenomena at the surfaces. If it does not, then we can get away with modeling a $ZnO/PbTiO_3$ system with fewer atoms hence less computational costs.

We use two ZnO layers, four lattice parameter thick PbO-terminated $PbTiO_3$ slab (bottom three fixed) and four layers of Pt at the bottom. We calculate the ZnO binding energy $PbTiO_3/Pt$ and $PbTiO_3$, density of states of $ZnO/PbTiO_3/Pt$ and $ZnO/PbTiO_3$, and $CO_2$ adsorption energy on $ZnO/PbTiO_3/Pt$ and $ZnO/PbTiO_3$. With the Pt and ZnO layers and the topmost $PbTiO_3$layer relaxed, we calculate the binding energy of ZnO to $PbTiO_3$ in the presence and absence of the electrode. We find that the electrode has no effect of the ZnO binding or $CO_2$ adsorption. The results are presented in Fig. 4-2.

Finally, we examine whether an electrode affects the electronic structure of the surface. As seen in Fig. 4-3, there is no significant change in the electronic structure of the layer both for the up- and down- polarized catalyst when the platinum electrode is removed.

From the foregoing, it is evident the electrode is not important to consider. There-

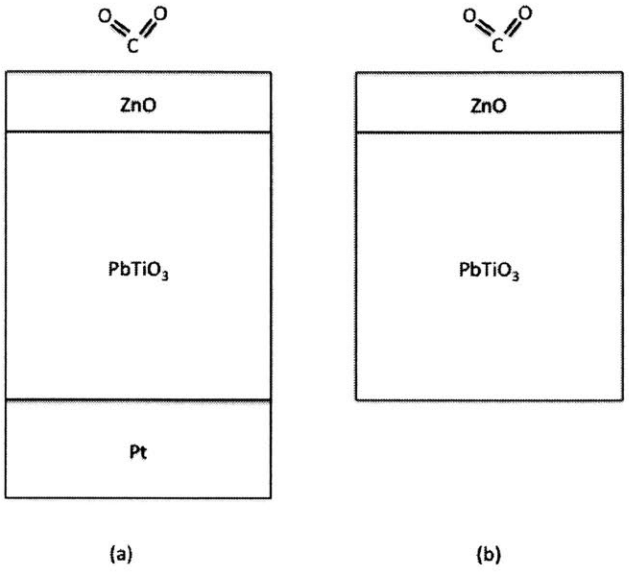


(a) Schematic

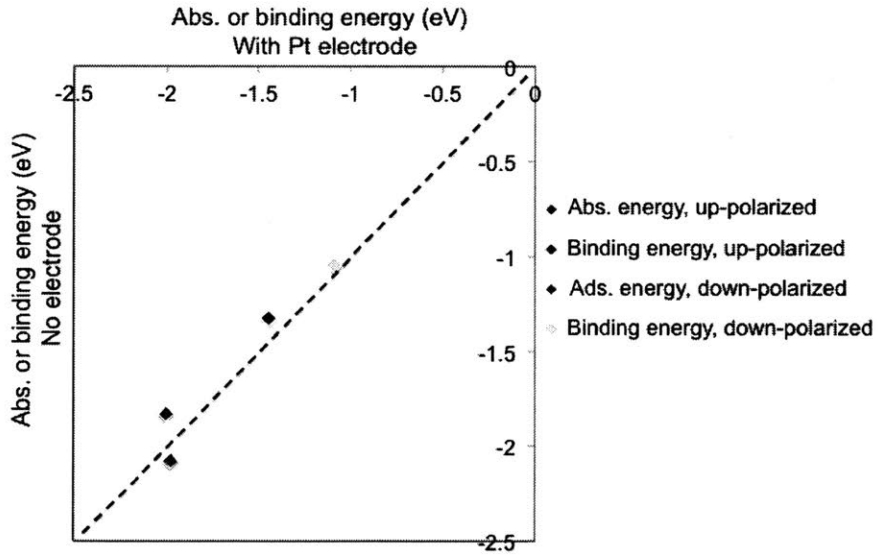


(b) Results

Figure 4-2: (a) Determining the effects of platinum electrodes on surface properties. Calculations were carried out with an electrode support and without an electrode support. (b)Comparing the ZnO binding energy on $PbTiO_3$ and $CO_2$ adsorption energy on $ZnO/PbTiO_3$ with and without a Pt electrode.

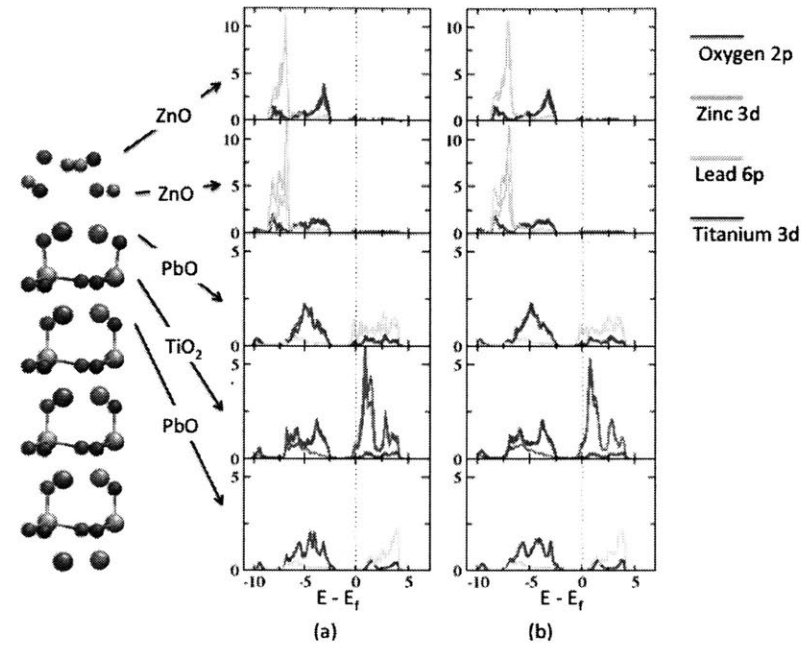


(a) With electrode

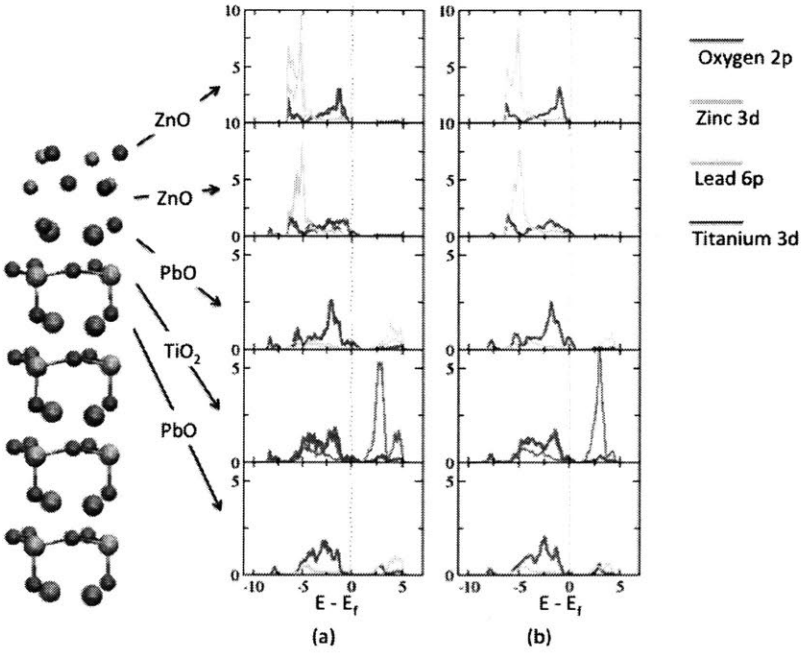


(b) No electrode

Figure 4-3: Projected densities of states for the topmost five layers of a) $(ZnO)_2/PbTiO_3/Pt$ and b) $(ZnO)_2/PbTiO_3$.

fore, in this work, we model $ZnO/PbTiO_3/Pt$ as $ZnO/PbTiO_3$.

### 4.2.2 DFT parameters.

To investigate the $ZnO(11\bar{2}0)/PbTiO_3(001)$ heterostructure, we perform DFT computations using the plane-wave pseudopotential code Quantum Espresso [94] with ultrasoft pseudopotentials [69] and wavefunction and charge density cutoffs of 35Ry and 280Ry respectively. The Wu-Cohen GGA functional [95] is used to describe exchange correlation; this functional has been shown to have equivalent or better performance to the ubiquitous PBE GGA functional for the prediction of structural and energetic properties of ferroelectric perovskite oxides, as well as a range of other solids, surfaces, and molecules [96].

To model the heterostructure, we use the experimentally reported $ZnO(11\bar{2}0)/SrTiO_3(001)$ epitaxial relationship [4]. The PbO-termination of the $PbTiO_3(001)$ slabs is selected, as this has been demonstrated to be the thermodynamically favored slab termination under relevant conditions [57]. The supercell geometry is illustrated in Fig. 4-1. A PbO-terminated cell with nine alternating PbO and $TiO_2$ atomic layers stacked in the (001) direction is used to represent the ferroelectric $PbTiO_3$ substrate. For calculations without $CO_2$ adsorption or dissociation, we use a $c(2\times2)$ PTO cell for which a $4 \times 4 \times 1$ $k$-point mesh is sufficient. For other calculations, we use a $(2\times2)$ PTO cell. A 20Å vacuum was added between periodic images in the $z$-direction and a dipole correction [97] is applied in the center of the vacuum region to remove artificial fields between periodic images in all calculations.

## 4.3 Results and Discussion

An inspection of the relaxed configuration of the heterostructures show changes in the surface Zn-O displacements with respect to the unsupported slab. The mechanism for this is shown illustrated in Fig. 4-5(a) and (b). The attraction of the Pb atoms on the substrate side at the interface of the positively-polarized structure to the O atoms in the ZnO film causes an increase in the Zn-O displacement in that layer.

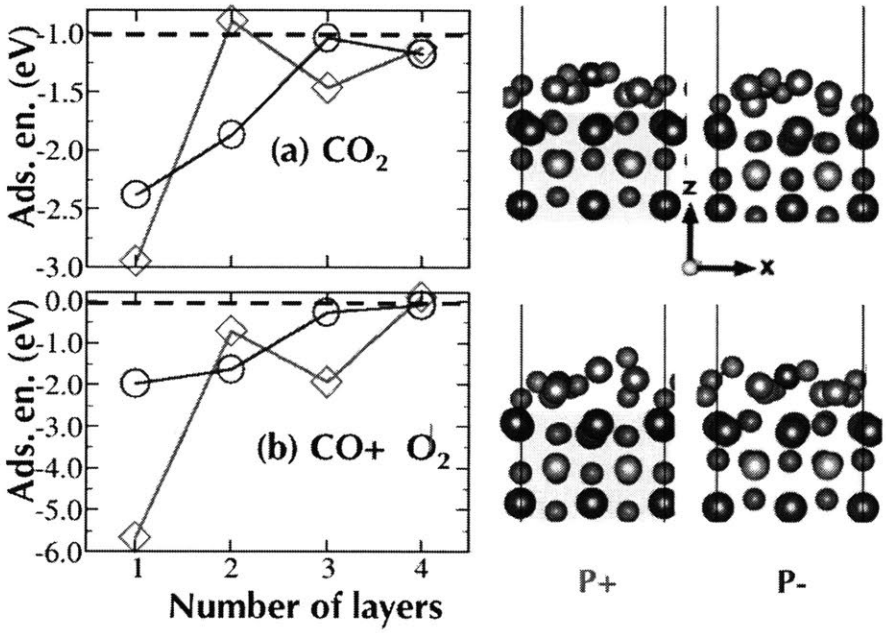


Figure 4-4: Adsorption energies of (a) $CO_2$, and (b) $CO+\frac{1}{2}O_2$, on $(ZnO(11\bar{2}0))_n/[2 \times 2]PbTiO_3$ as a function of $n$. Diamonds and circles represent adsorption on the positively and negatively polarized structures, respectively. horizontal dashed lines represent the adsorption energy of the molecules on an unsupported ZnO slab. Structures on the right show the adsorption configurations for the corresponding molecule on stoichiometric structures with $n$ =1. Oxygen atoms in the adsorbates are colored magenta for clarity.

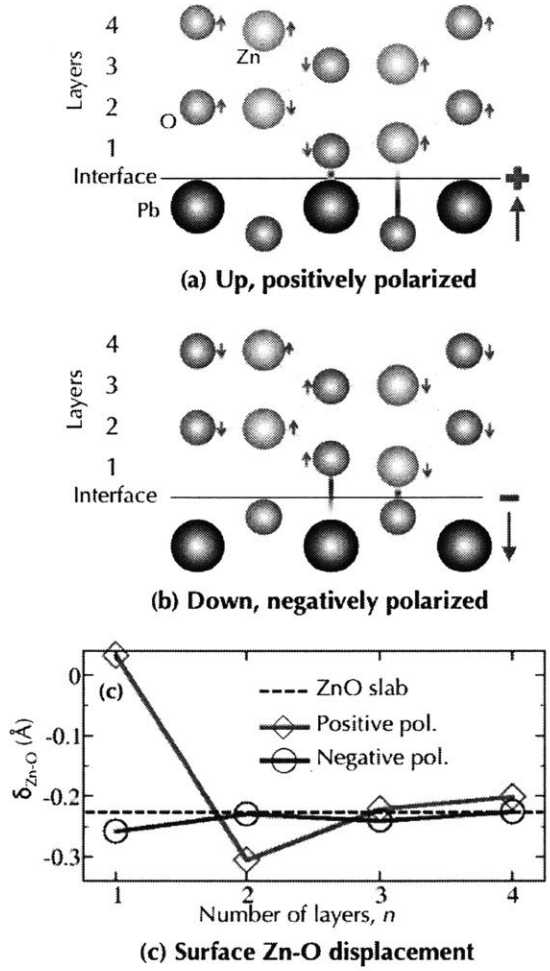


Figure 4-5: Mediation of the interface chemistry by the (a) positively polarized (b) negatively polarized substrates. (c) is a plot of the surface displacements.

The next layer however experiences a decrease in its Zn-O displacement, and so on. The opposite effect explains the trend for the negatively polarized structure. The effect of the interface mediation gets weaker as the surface layers gets farther from the surface. The data plotted Fig. 4-5(c) suggests that the interface mediated mechanism is correct.

However, we do not suggest that the surface chemistry on the surfaces is entirely determined by the positioning of the ZnO atoms. Since the surfaces of the polarized surfaces of $PbTiO_3$ are charged, we expect some distortion in the electronic density in the ZnO layer even if the relative atomic positions do not change. A calculation of the

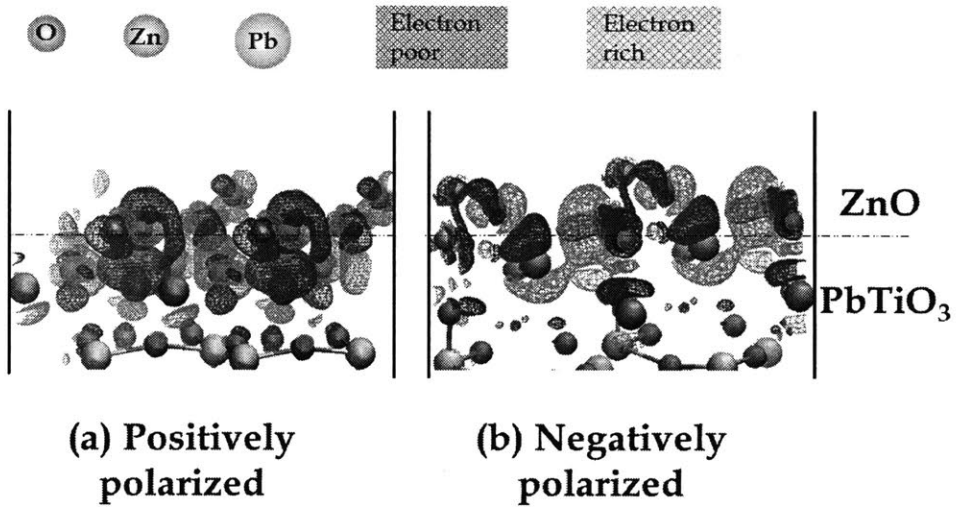


Figure 4-6: Redistribution of charges in one-layer ZnO($11\bar{2}0$) when the $PbTiO_3$ substrate is (a) positively polarized (b) negatively polarized.

redistribution of charges in the ZnO layer due to the presence of the $PbTiO_3$ substrate is visualized in Figure 4-6. This calculation is done by first separately calculating the electronic density in 3D for the ZnO and the perovskite and substracting the results from a the electronic density of the combined system. We interlayed the atomic positions with the electronic density information to obtain the figures. We see that the surface of the ZnO is primarily electron deficient or has an electron surplus depending on whether the substrate is positively or negatively polarized respectively. In addition to the atomic positions, these charges will invariably have some effect on the surface chemistry.

We perform calculation of the adsorption energies of $CO_2$ and $CO+\frac{1}{2}O_2$ on the surfaces using a coverage of one molecular adsorbate per 2×2 $PbTiO_3$ surface cell, starting from a range of initial adsorbate positions and geometries. The reported adsorption energies in Fig. 4-4(a) are for the minimum energy adsorption geometry on the indicated surface. As the figure demonstrates, changing the polarization direction of the substrate leads to a difference of $\sim$ 0.6eV in the $CO_2$ adsorption energy for the thinnest ZnO film. The results demonstrate the changing surface chemistry as a function of substrate polarization and film thickness. The difference tapes off, with

the heterostructure behaving very similarly to the unsupported ZnO slab for $n \geqslant 4$ ZnO layers. Similar behavior is seen for $CO+\frac{1}{2}O_2$, as shown in Fig. 4-4(b).

The flip-flop pattern in the adsorption energies in the plots in Fig. 4-4 can be directly correlated to the cation displacements at the slab surface, which has the same form with respect to number of ZnO layers and substrate polarization (see Fig. 4-5). We find that the magnitude of the displacement in each ZnO layer depends on the distance from the $PbTiO_3$ surface and its polarization, becoming approximately the same as that in surface of the unsupported thick ZnO after the third layer for both substrate polarization directions. In other words, the magnitude and degree of decay of the surface zinc-oxygen displacements away from the substrate are directly related to the dipole at the interface. Therefore, by changing the magnitude of the displacement at the interface, it may be possible to modify the displacement at the ZnO surface and thus the sensitivity of the tunable catalyst. To confirm this hypothesis, we perform calculations using the less stable [57] $TiO_2$-terminated surface, which exhibits smaller displacements than the PbO termination. We find that $CO_2$ adsorption on one-layer of ZnO supported on the $TiO_2$-terminated substrate is ~10% (~54%) as strong as that on the positively (negatively) polarized PbO-terminated substrate, suggesting that an important design principle for a tunable catalyst with ZnO is to find subtrates with reversible polarizations and large surface displacements. We predict, for example, that the ferroelectricity-induced ZnO surface chemistry changes will be greater for $BiMO_3$ (where M is for example, Fe) than $BaTiO_3$ or $PbTiO_3$ substrates.

### 4.3.1 Detailed adsorption properties of adsorbed $CO_2$ on $(ZnO)_1/PbTiO_3$ and ZnO slab.

We examine in detail $CO_2$ adsorption as shown in Figure 4 in the main paper. Figure 4-7 shows the bond lengths and $CO_2$ angles for the chemical adsorptions on ZnO slab and $(ZnO)_1/PbTiO_3$.

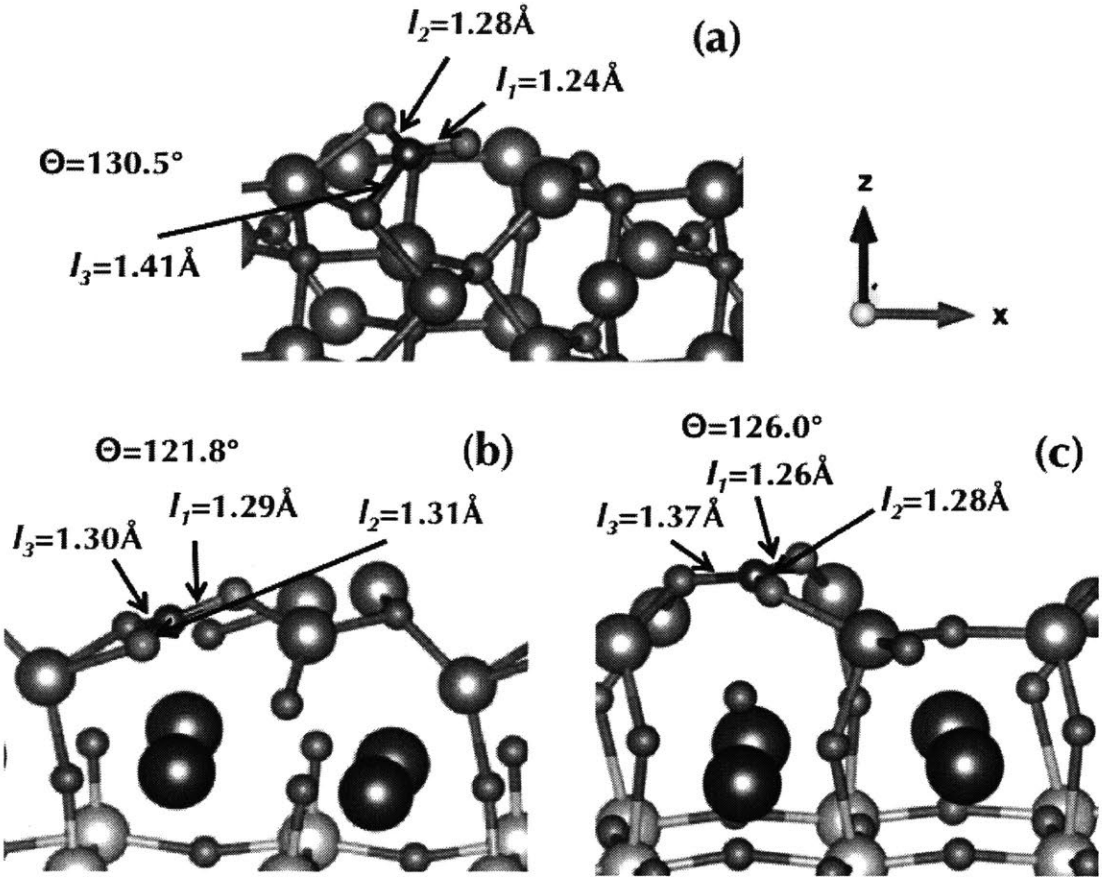


Figure 4-7: $CO_2$ adsorption geometry on (a) ZnO slab (b) $(ZnO)_1/PbTiO_3\uparrow$ (c) $(ZnO)_1/PbTiO_3\uparrow$.

| Substrate | $l_1$ (Å) | $l_2$ (Å) | $l_3$ (Å) | $\theta$ ( |
|---|---|---|---|---|
| ZnO slab | 1.28 | 1.24 | 1.41 | 130.5 |
| $(ZnO)_1/PTO\uparrow$ | 1.29 | 1.31 | 1.30 | 121.8 |
| $(ZnO)_1/PTO\downarrow$ | 1.26 | 1.28 | 1.37 | 126.0 |
| $(ZnO)_2/PTO\uparrow$ | 1.18 | 1.18 | 2.83 | 176.6 |
| $(ZnO)_2/PTO\downarrow$ | 1.26 | 1.28 | 1.39 | 128.9 |
| $(ZnO)_3/PTO\uparrow$ | 1.26 | 1.27 | 1.39 | 126.8 |
| $(ZnO)_3/PTO\downarrow$ | 1.25 | 1.26 | 1.43 | 128.8 |
| $(ZnO)_4/PTO\uparrow$ | 1.25 | 1.28 | 1.39 | 129.5 |
| $(ZnO)_4/PTO\downarrow$ | 1.25 | 1.28 | 1.39 | 129.5 |

Table 4.1: $CO_2$ adsorption geometries on the substrates. $l_1$ and $l_2$ are the lengths of the C-O bonds in the $CO_2$ molecule and $l_3$ is the length of the bond between the carbon atom and the nearest O atom on the surface. $\theta$ is the O-C-O angle in the adsorbate.

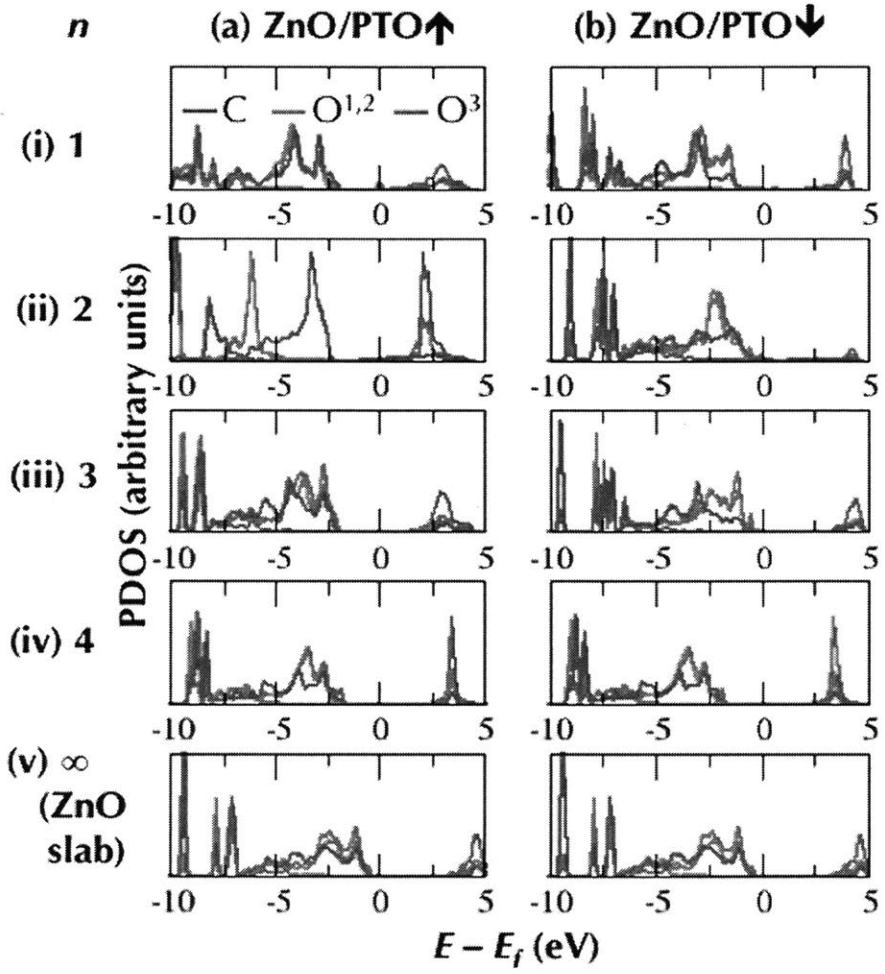


Figure 4-8: Projected density of states (PDOS) of C and the two O atoms of $CO_2$ after adsorption on (a) ZnO slab (b) $(ZnO)_1/PbTiO_3\uparrow$ and (c) $(ZnO)_1/PbTiO_3\uparrow$.

## 4.4 Conclusion

In conclusion, we have shown that the configuration at the interface is dependent on the growth conditions and polarization of the substrate. We also show that the surface chemistry of stoichiometric $(ZnO(11\bar{2}0))_n/PbTiO_3$ is dependent on both the polarization direction of the $PbTiO_3$ substrate and the number of $ZnO(11\bar{2}0)$ layers $n$, with the effect of the substrate polarization becoming negligible for $n \geq 4$. The large changes in $CO_2$ adsorption energy with polarization switching reported in this work suggest the possibility of controlling reaction energetics and pathways of $CO_2$ reactions, as indicated by the proposed dynamic polarization-switching scheme for a $CO_2$ dissociation reaction on $ZnO(11\bar{2}0)/PbTiO_3$. Finally, we note that this approach can be applied to many other reactions in heterogenous catalysis, potentially opening new avenues for controlling reaction energetics.

# Chapter 5

# Reversible Polarization in Thin-Film ZnO

## 5.1 Introduction

ZnO is one of the most well-studied metal oxides, with technological importance as a gas sensor [98], a transparent electrode [99, 100], and a co-catalyst for methanol production from syngas [101]. ZnO has a permanent spontaneous polarization of 0.057 $C/m^2$ [102, 103], one of the highest among III-IV oxides. On the other hand, $ABO_3$ perovskites such as $PbTiO_3$, $BaTiO_3$, and $BiFeO_3$, can exhibit a large, reversible ferroelectric polarization, and also generally have piezoelectric, pyroelectric and electro-optical properties that allow for many applications, including thin film capacitors, displays, memory devices and pyroelectric detectors. Creating ZnO-perovskite heterostructures has the potential to lead to new, multi-functional materials that exhibit a variety of interesting new physical phenomena.

Due to their increased gas sensitivity [104], morphology-control characteristics [105], and photocatalytic [106] and catalytic [107] activities, the polar (0001) surfaces of ZnO have received special attention in recent studies compared to the non-polar $(11\bar{2}0)$ and $(10\bar{1}0)$ surfaces. Furthermore, the lack of inversion symmetry in ZnO(0001) slabs gives it piezoelectric properties and a spontaneous polarization.

However, polar ZnO does not undergo any phase transitions at atmospheric pres-

sures and its polarization cannot be switched with an electric field until its melting temperature of 2248 K [108], making it impossible to use the intrinsic polarity in ZnO in a ferroelectric device. Successful attempts to induce reversible polarization in ZnO at mild temperatures [108, 109, 110] have included Li-doping, resulting in a ferroelectric transition at 330-360K at 6-10% Li concentration. In this method, the smaller dopant atoms substitute Zn and occupy off-center positions, forming local electric dipoles which lead to ferroelectric behavior. However, the largest remnant polarization obtained with this approach has been only 0.008 $C/m^2$ [111, 112, 113], which is seven times less than the calculated spontaneous polarization in ZnO.

In the present work, we investigate a different approach, showing that it is possible to attain reversible polarization in ZnO thin films without doping by making use of a ferroelectric substrate. In addition, we discuss the potential applications of this system as a tunable catalyst.

Normally, thick *c*-axis ZnO(0001) slabs have an intrinsic electrostatic instability due to the presence of macroscopic electric fields induced by the electric dipoles [114]. This instability is counteracted by surface reconstructions [115], surface metallization, or surface passivation [39]. When the slab is sufficiently thin, however, another compensation mechanism becomes more important. Results from theoretical [116, 117, 118, 119] and experimental [120, 121] studies show that the dipole moments in each ZnO bi-layer disappear when the slab is sufficiently thin, thereby requiring no compensation mechanism; instead, the Zn and O atoms in each bilayer align so that they form one graphitic layer in ABAB formation with respect to other layers.

The spontaneous transition from a graphitic slab in thin ZnO(0001) films to a polar slab when more layers are added suggests there is a low energy pathway between the graphitic and polar states in thin films. The expected mechanism for this process is the buckling of $Zn_3O_3$ rings, as proposed by Claeyssens *et al.* [120]. In this work, we explore how a transition from one ZnO polarization to another can be achieved by inducing the buckled phase $\rightarrow$ graphitic phase $\rightarrow$ reverse buckled phase transition in thin films using a ferroelectric substrate (see Fig. 5-1).

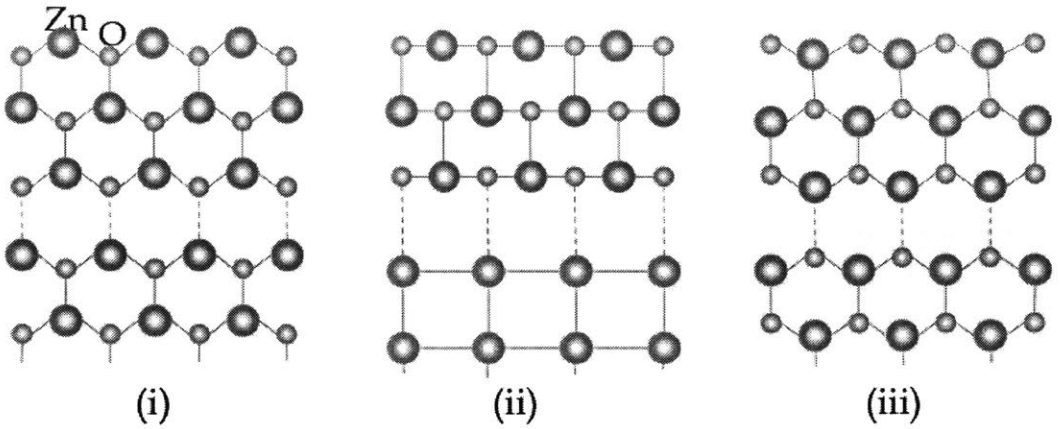


(a) ZnO epitaxy on ZnO and non-polarized substrate

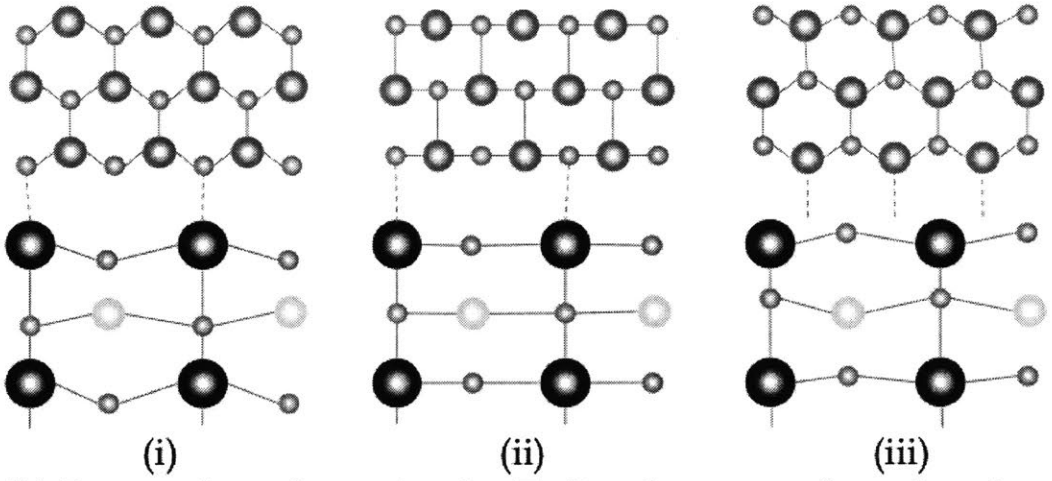


(b) Expected configuration for ZnO epitaxy on a ferroelectric

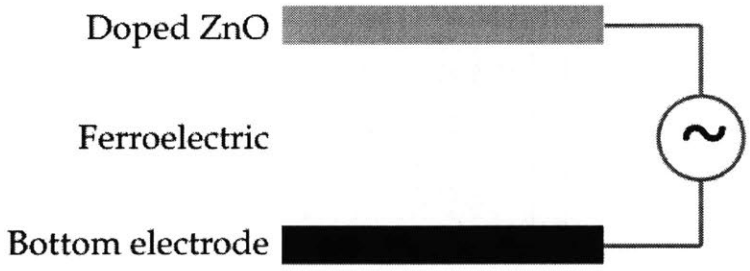


(c) Scheme for polarization switching in thin-film ZnO

Figure 5-1: (a) ZnO epitaxy on *c*-axis oriented ZnO ((i) and (iii)) and an arbitrary lattice-matched non-polar substrate ((ii)). (b) Expected ZnO epitaxy on (i) positively polarized ferroelectric, (ii) neutral ferroelectric (iii) negatively polarized ferroelectric. (c) Scheme for switching the polarization of thin-film ZnO. The doping of the ZnO is to enable its use as an electrode.

## 5.2 Computational Methods

We model ZnO(0001) epitaxy on $PbTiO_3$ assuming the epitaxial relationship obtained in the experimental work of Wei *et al.* [122]. DFT computations are performed using the plane-wave pseudopotential code Quantum Espresso [94]. A PbO-terminated centered 3 × 3 cell with 9 alternating PbO and $TiO_2$ layers stacked in the (001) direction is used for the $PbTiO_3$ substrate, with 1-4 layers of ZnO oriented in the 0001 or $000\bar{1}$ directions. All the ZnO layers and the topmost PbO and $TiO_2$ layers were fully relaxed; the other PbTiO3 layers were fixed to the bulk atomic positions to simulate a thick substrate. All calculations were performed with an energy cutoff of 35 Ry and a $k$-point mesh of $1 \times 1 \times 1$. Heterostructures composed of $ZnO(0001)_n$ and $ZnO(000\bar{1})_n$ epitaxial layers on $PbTiO_3$ positively and negatively polarized slabs with $n$ =1, 2, 3 and 4 were considered, for a total of 16 systems. For each system, the different starting configurations for ZnO(0001) epitaxy on the perovskite were considered, as represented for $n = 4$ in Figure 5-2. In addition, we calculated the ground state structure for freestanding ZnO starting from a bulk-like configuration was determined. In all calculations, the starting configuration did not include a graphitic ZnO phase; however, as shown below, such phases were observed upon relaxation to the ground state or as one of the states along a polarization switching path.

## 5.3 Results and Discussion

### 5.3.1 Ground States

To test our hypothesis that, in the ground state, the polarization of the ZnO film will be aligned with that of the ferroelectric substrate, we first consider two initial configurations with the polarization of epitaxial ZnO in parallel and anti-parallel direction to that of the substrate. For each substrate polarization and each film thickness. The starting configurations are illustrated for the case of $n = 4$ in Fig. 5-2 (see pairs [(a), (b)] and [(c), (d)] in the upper panels). The lower panels in the figure show the final

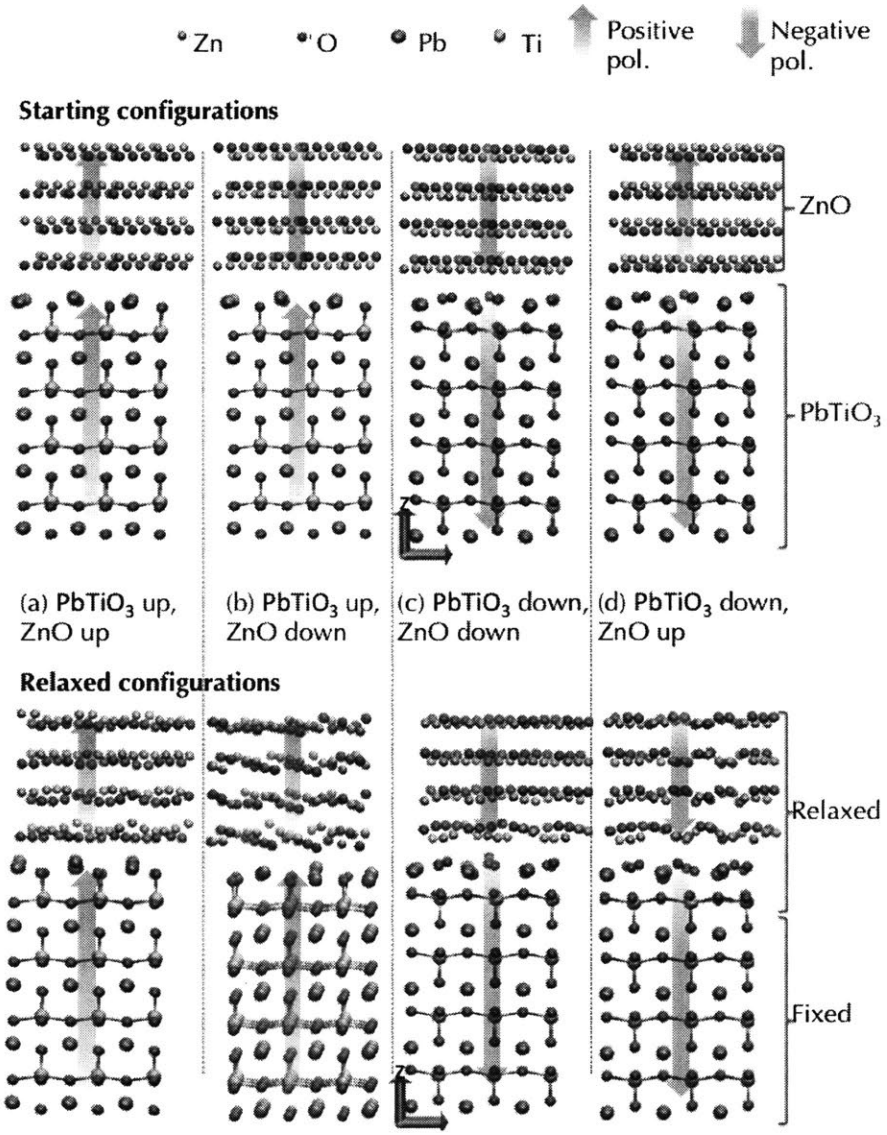


Figure 5-2: Starting (top) and final (bottom) configurations for the calculation of the ground states of $ZnO(0001)_n/PbTiO_3$ for $n = 4$. For each direction of substrate polarization, we did relax calculations with the polar ZnO film in the same ((a) and (c)) and opposite ((b) and (d)) polarization directions.

| $n$ | Transformation | $\lvert\Delta G\rvert$ (eV) | $E_a$ (eV) |
|---|---|---|---|
| 3 | (b)→(a) | 0.005 | 0.037 |
| | (d)→(c) | 0.013 | 0.009 |
| 4 | (b)→(a) | 0.015 | 0.030 |
| | (d)→(c) | 0.030 | 0.038 |

Table 5.1: Free energy $|\Delta G|$ and upper bound of activation energy $E_a$ for the relaxed configurations of Fig. 5-2(b) and (d) to reach absolute minima. $n$ is the number of layers. The energy values are normalized per ZnO pair.

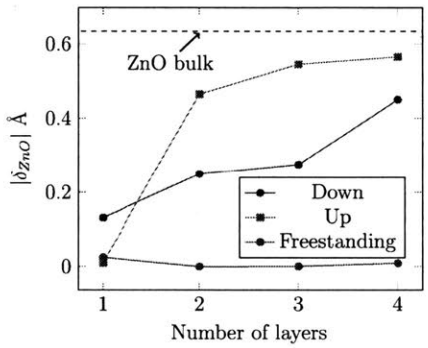


Figure 5-3: Absolute value of the average buckling in the ZnO bi-layers.

relaxed configurations. As hypothesized, the polarization of the epitaxial ZnO layer aligns with that of the substrate irrespective of the initial configuration. The two final positively polarized configurations (a) and (b) are essentially identical, as are the two final negatively polarized configurations (c) and (d), as confirmed by calculation of the activation energy $E_a$ and the free energy $|\Delta G|$ for interpolated pathways between stuctures (a) and (b) and structures (c) and (d) (see Table 5.1). Therefore, in the rest of this work, we use the lower-energy ground state in Fig. 5-2(a) for the positively polarized case and Fig. 5-2(c) for the negatively polarized case.

Figure 5-3 shows the magnitude of the average difference between the $z$-positions of the Zn and O atoms in each bi-layer of ZnO for films with 1-4 layers. We compare these to corresponding values for the freestanding ZnO films. We can clearly infer that the polarization of the perovskite substrate induces a similarly oriented polarization in the thin film which would have been in a graphitic phase without the influence of the substrate.

### 5.3.2 Energy Considerations

Because some of atoms in the perovskite layers are fixed to simulate a thick substrate, the full, relaxed $ZnO/PbTiO_3$ heterostructures are not at their minimum energies. Therefore, traditional nudged elastic band calculations cannot be used straightforwardly to determine the additional energy for switching the ZnO polarization. To determine this energy, we perform a series of calculations optimizing the atomic structure of the interfacial $PbTiO_3$ and ZnO thin film layers with the atoms in the bottom layers of the simulated $PbTiO_3$ substrate fixed at fractions of the $PbTiO_3$ polarization transformation vector between the positively and negatively polarized states. We then substract the energy of the $PbTiO_3$ layers calculated in a separate self-consistent field calculation.

If we define $\delta$ as the matrix of total differences between corresponding atomic positions of any two end states, and $0 < x < 1$ as a fraction denoting how far the switching has progressed, then the energy at each point along the transition pathway is given by

$$E(\mathrm{ZnO})_{\delta x} = E(\mathrm{ZnO/PbTiO_3})_{\delta x} - E(\mathrm{PbTiO_3})_{\delta x} \tag{5.1}$$

The energy cost for switching the ZnO film is thus given by the difference between $E(\mathrm{ZnO})_{0\delta}$ and $E(\mathrm{ZnO})_{0.5\delta}$. We find this value to be 0.065 eV/Å. Normalized to the same surface area, this energy is of the same order as the computed energy required to switch the perovskite bulk (0.067 eV/Å). This shows that the ZnO film does not introduce a significant additional energy cost if, for example, the $ZnO/PbTiO_3$ heterostructure were to be used in a ferroelectric device.

### 5.3.3 Application to Tunable Catalysis

One interesting potential application of the reversible polarization in ZnO thin films is in tunable catalysis. In a switchable ZnO polar slab, the surface will switch between Zn-terminated (0001) and O-terminated $(000\bar{1})$, which are known to have very different chemical properties [123, 124]. Figure 5-4 shows the projected density of

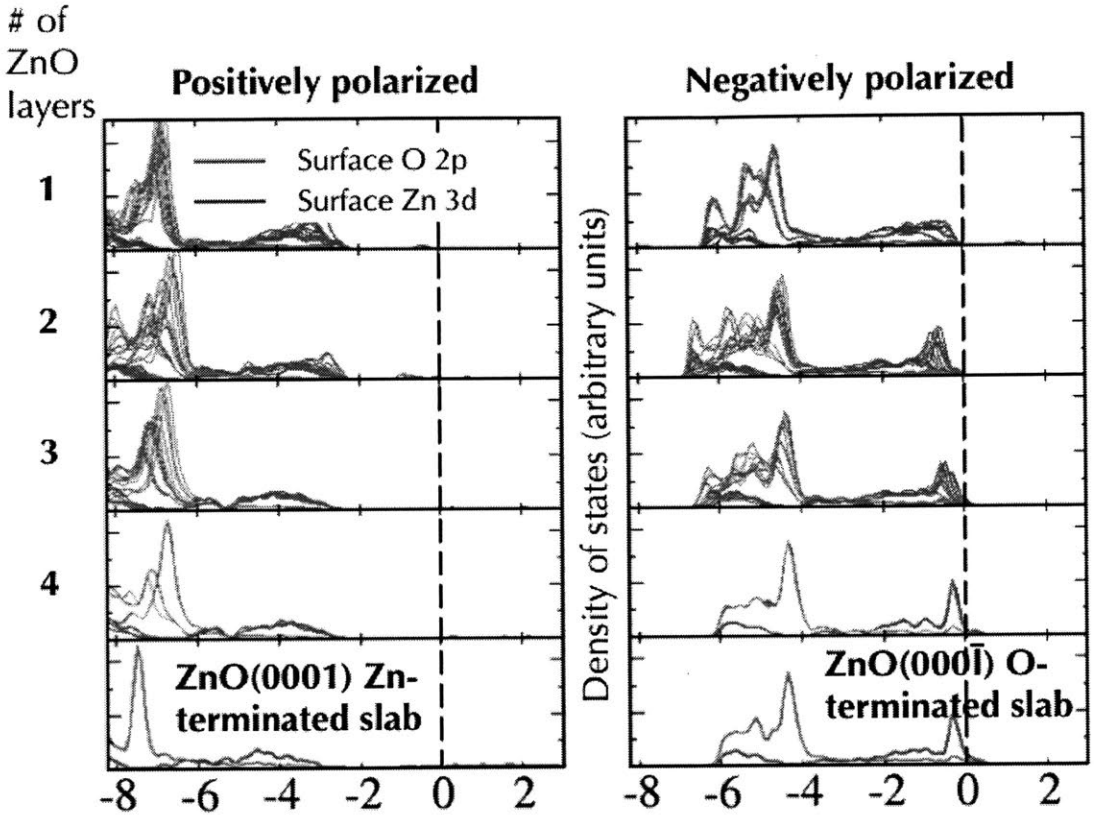


Figure 5-4: Densities of states projected on the topmost Zn and O atomic layers in $ZnO(0001)_n/PbTiO_3$ for $n$ =1, 2, 3 and 4. The bottom graphs are for unsupported *thick* ZnO slabs.

states of the atoms in the top ZnO layer in each orientation of the substrate polarization and ZnO film thickness. Due to the similarities in the electronic structures of the terminations for each polarization direction, we can infer that polar ZnO grown on positively polarized $PbTiO_3$ will display characteristics similar to that of a Zn-terminated ZnO(0001) slab. In contrast, polar ZnO grown on negatively polarized $PbTiO_3$ will display characteristics similar to that of an O-terminated ZnO(0001) slab. Based on our previous work, we hypothesize that if the different surfaces can be cyclically switched to interact with the chemical species, the rate of reaction may significantly increase. [3, 82]

As a simple test, we calculate $CO_2$ adsorption energies on $ZnO(0001)_n/PbTiO_3$ and compare these to adsorption energies on ZnO(0001) slabs (Fig. 5-5). The difference in adsorption energies for the different polarizations is as high as 1.65 eV and

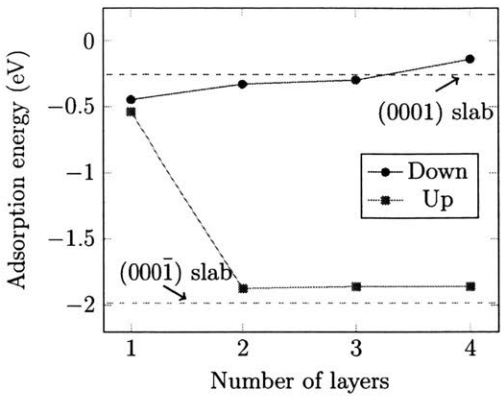


Figure 5-5: Adsorption energies of $CO_2$ on $ZnO(0001)_n/PbTiO_3$ for $n$ =1, 2, 3 and 4. Lines denoting the adsorption of $CO_2$ on $ZnO(000\bar{1})$ slabs are added.

shows remarkable consistency as the number of layers increases. This is important for tunable catlaysis because it relies on predictable but very different surface chemistry at the different states of a catalyst.

## 5.4 Conclusion

In conclusion, we have investigated the $ZnO(0001)/PbTiO_3$ heterostructure and showed that it is possible to switch the polarization of the ZnO film when the polarization of the underlying perovskite is switched. The ZnO film does not introduce any new energy requirement for polarization switching. Finally, we showed that the polarization reversal is sufficient to enable a consistent surface chemistry depending on the polarization, providing an excellent basis for a dynamically tunable catalyst.

# Chapter 6

# The development of a framework for the analysis of dynamically tunable catalysis of $CO_2$

## 6.1 Introduction

In the last two chapters, we saw that the $CO_2$ adsorption energy, $CO_2$ adsorption geometry and the surface charges (dipoles) change between the polarization states of perovksite-supported ZnO. These properties have been shown to affect reaction pathways and energetics [125, 126, 127]. Therefore our results strongly suggest that the polarization-induced changes in these properties will affect $CO_2$ conversion processes in some way, leading to tunable catalysis as the polarization is cycled. In this chapter, we investigate this idea by determining the reaction pathway and energy barrier for a simple conversion process, thermally-activated dissociation of $CO_2$(g) into CO(g) and $O_2$(g), over a reversibly tunable surfaces of $ZnO/PbTiO_3$.

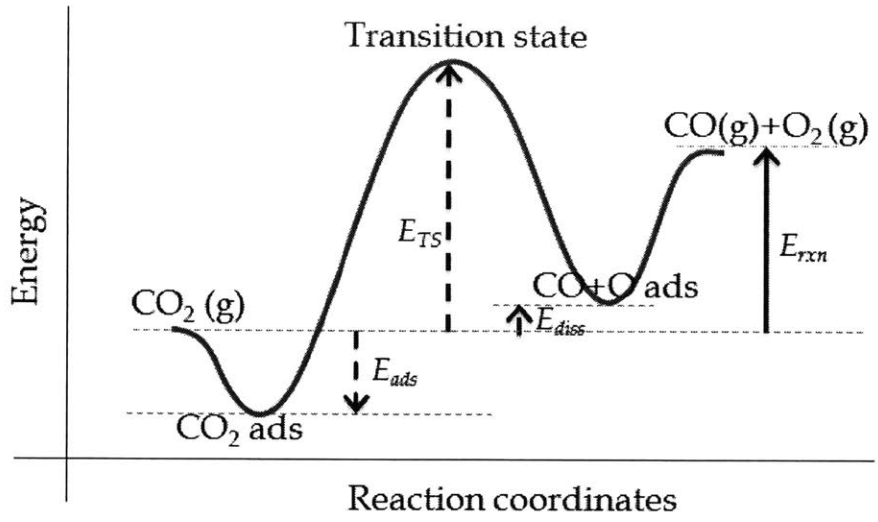


Figure 6-1: Parameters calculated in the reaction pathway for $CO_2$ dissociation.

## 6.2 Methods

### 6.2.1 Computational methods

The reaction pathway and energy barriers for $CO_2$ dissociation to CO and $O_2$ can be completely mapped by calculating adsorption energies of $CO_2$, CO and $O_2$ and the pathway for the formation of CO+O surface species from adsorbed $CO_2$ species. The adsorption energies are taken from previouly reported results. To compute the energy profile for the formation of the CO+O intermediate, we use nudged elastic band calculations [74, 128] or the fixed bond length method which when carefully calculated are equivalent for this simple one degree of freedom process.

The energies we calculate for are shown in Fig. 6-1. All energies are relative to the free $CO_2$ molecule. $E_{ads}$ is the adsorption energy of $CO_2$. The adsorbed molecule dissociates to CO and O on the surface. The activation energy for the dissociation is $E_a = E_{TS} - E_{ads}$. The dissociative adsorption energy is the energy of adsorbed CO+O relative to the $CO_2$ molecule. The energy change of the overall reaction, $E_{rxn}$ is taken from the thermodynamic tables for $CO_2$, CO and $O_2$ at 300 K in the NIST Chemistry Webbook [129].

### 6.2.2 Microkinetic model

We build a microkinetic model assuming that the $CO_2$ binds strongly to the surface in a tridentate manner, occupying three sites per an area equivalent to the $2 \times 2$ $PbTiO_3$ surface. Similarly, the CO molecule occupies two sites and the O atom occupies one site when adsorbed. The microkinetic model steps are as follows:

Step 1 ($CO_2$ adsorption): $CO_2 + 3* \longrightarrow CO_2***$

Step 2 ($CO_2$ dissociation): $CO_2*** \longrightarrow CO** + O*$ . This is the rate limiting step

Step 3 (CO desorption): $CO** + O* \longrightarrow CO + 2** + O*$

Step 4 (Oxygen desorption): $O* \longrightarrow \frac{1}{2}O_2 + *$

We apply quasi-static approximation (all steps except the rate limiting step are in equilibrium). We define the rate constants at equilibrium for each step except the rate limiting one.

$$K_1 = \frac{\theta_{CO_2}}{\frac{P_{CO_2}}{P_{ref}}\theta_*{}^3} \tag{6.1}$$

$$K_3 = \frac{\theta_*{}^2 \frac{P_{CO}}{P_{ref}}}{\theta_{CO}} \tag{6.2}$$

$$K_4 = \frac{\theta_* \left(\frac{P_{O_2}}{P_{ref}}\right)^{1/2}}{\theta_O} \tag{6.3}$$

The coverages $\theta$ are related by:

$$\theta_{CO_2} + \theta_{CO} + \theta_O + \theta_* = 1$$

which gives

$$K_1 \left(\frac{P_{CO_2}}{P_{ref}}\right) \theta_*{}^3 + \frac{1}{K_3}\left(\frac{P_{CO}}{P_{ref}}\right) \theta_*{}^2 + \frac{1}{K_4}\left(\frac{P_{O_2}}{P_{ref}}\right)^{1/2} \theta_* + \theta_* = 1 \tag{6.4}$$

We can find the coverages by solving this equation.

The overall rate of reaction, in number of $CO_2$converted per site per second, is

given by the rate of the limiting step

$$\begin{aligned} R_{overall} = R_2 &= k_2\theta_{CO_2} - k_{2-}\theta_O\theta_{CO} \\ &= k_2\theta_{CO_2} - \frac{k_2}{K_2}\theta_O\theta_{CO} \\ &= k_2\theta_{CO_2} - k_2\theta_{CO_2}\frac{\theta_O\theta_{CO}}{K_2\theta_{CO_2}} \\ &= k_2\theta_{CO_2}(1-\beta) \\ &= k_2K_1\left(\frac{P_{CO_2}}{P_{ref}}\right)\theta_*{}^3(1-\beta) \end{aligned}$$

where $\beta$ is the approach to equilibrium for the rate limiting step.

In the final expression, we note that:

$$\beta = \frac{\theta_O\theta_{CO}}{K_2\theta_{CO_2}}$$

$$k_2 = v_2 e^{-E_a/kT}$$

$$K_1 = e^{-\Delta G_1/kT}$$

$$K_3 = e^{-\Delta G_3/kT}$$

$$K_4 = e^{-\Delta G_4/kT}$$

where $v_2$ is the attempt frequency, $k_2$ and $E_a$ are the rate constant and activation energy of the forward reaction for the RLS respectively, and $K_1$, $K_3$ and $K_4$ are the equilibrium constants of the corresponding steps. With reference to the notation in Fig. 6-1, we note that $G_1 = E_{ads}$, $G_3 = a(E_{rxn} - E_{diss})$ and $G_4 = b(E_{rxn} - E_{diss})$, where $a$ and $b$ are such that $a + b = 1$ and are separate calculated or estimated.

The rate of reaction, in g/s is then given by:

$$R_{mass} = M_{CO_2} * R_{overall} * A_s * N_s/N_A \tag{6.5}$$

where $R_{mass}$, $M_{CO_2}$, $A_s$, $N_s$ and $N_A$ are the mass flow rate in g/s, molar mass of $CO_2$, number of sites available per area and the Avogradro number respectively. Solving

| Substrate | Notation | $E_{ads}$ (eV) | $E_{TS}$ (eV) | $E_{diss}$ (eV) |
|---|---|---|---|---|
| ZnO(1120) slab | Non polar slab | -1.00 | 5.55 | 5.64 |
| $ZnO(1120)_1/PbTiO_3\uparrow$ | 1L + | -2.95 | -0.25 | -0.57 |
| $ZnO(1120)_1/PbTiO_3\downarrow$ | 1L - | -2.38 | 3.76 | 3.53 |
| $ZnO(1120)_2/PbTiO_3\uparrow$ | 2L + | -0.90 | 4.06 | 3.89 |
| $ZnO(1120)_2/PbTiO_3\downarrow$ | 2L - | -0.96 | 5.15 | 5.15 |
| $ZnO(1120)_3/PbTiO_3\uparrow$ | 3L + | -1.47 | 4.23 | 4.33 |
| $ZnO(1120)_3/PbTiO_3\downarrow$ | 3L - | -1.04 | 5.64 | 5.27 |
| Zn-terminated $ZnO(0001)/PbTiO_3\uparrow$ | Polar + | -1.10 | 1.77 | 1.53 |
| O-terminated $ZnO(0001)/PbTiO_3\downarrow$ | Polar - | -0.23 | 4.70 | 4.58 |

Table 6.1: $E_{ads}$, $E_{TS}$ and $E_{diss}$ values for $CO_2$ dissociation on all surfaces considered.

these equations at fixed values of effective surface area $A_s = 2 \times 10^7 m^2$, $CO_2$ partial pressure of 10 atm, a frequency factor of $5 \times 10^{13}$ and $\beta = 0.1$ yields the results reported in the paper. Varying these values over a wide range do not significantly affect the results since we are concerned with the ratio of the rates.

## 6.3 Results

Figure 6-2 shows the computed reaction pathways for $CO_2$(g) adsorption and conversion to CO(g) and $O_2$(g) over the ferroelectric-supported one-layer $ZnO(11\bar{2}0)$ films and on the unsupported $ZnO(11\bar{2}0)$ slab. The rest of this section applies to these surfaces but a similar analysis can be done for the rest. The values of the energies corresponding to the parameters in Fig. 6-1 for all the other surfaces considered are shown in Table 6.1.

In Fig. 6-2, the first step of the reaction, $CO_2$ adsorption, is a spontaneous process on all three surfaces. The dissociation of adsorbed $CO_2$ into adsorbed CO and adsorbed O is endothermic for all three surfaces, but is significantly more favorable on the positively polarized structure (red line), with an activation energy barrier less than half that of the reference unsupported ZnO slab (dashed line). The last step, desorption of CO + $\frac{1}{2}O_2$, however requires a large energy input for the positively polarized structure, but occurs spontaneously for the reference surface and requires only minimal energy for the negatively polarized structure.

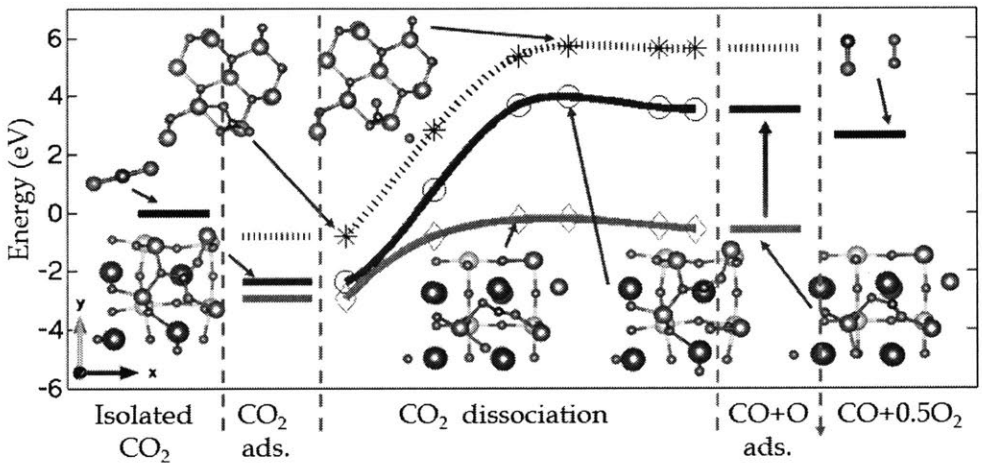


Figure 6-2: Reaction pathway for $CO_2$ dissociation over unsupported ZnO (gray stars) and ZnO supported on positively and negatively poled $PbTiO_3$ (red diamonds and blue circles, respectively). The vertical axis is energy with respect to an isolated $CO_2$ molecule. The vertical arrow indicates switching of the substrate polarization from P+ to P-. Atom colors are the same as in Fig. 4-1, with adsorbate O atoms shown in magenta for clarity.

Our results suggest a possible approach for increasing the rate of $CO_2$ dissociation on ZnO surfaces: grow a ZnO thin film on a positively polarized substrate, on which the first few steps of the reaction take place, switch the polarization (depicted by the arrow in the figure) to induce the desorption of the products, then switch back and repeat.

In the rest of this section, we will discuss how rate of the $CO_2$ dissociation reaction and how it is affected by a static or cyclically polarized substrate. Using data from Table 6.1, we calculate the rate of reaction (turn-over frequency) $R$ of the dissociation reaction on each of the surfaces (see Equation 3.15). In Fig. 6-3, we plot the reaction rates against the dissociative adsorption energy $E_{diss}$ defined as the energy of adsorbed CO+O relative to an isolated $CO_2$ molecule. This choice of parameter is made because it has been shown that an appropraite proxy for the strength of the interaction of a surface with the species is the dissociative adsorption energy of the key species [130], in this case $CO_2$.

It is of interest to compare the rate in a tunable catalysis scheme as depicted in Fig. 6-2. We assume that the first two reaction steps ($CO_2$ adsorption and dissociation) proceed on the positively polarized surface. Afterwards, the polarization of the heterostructure is switched and the desorption of the adsorbates proceeds on the negatively polarized surface. The rate of reaction for this tunable catalysis scheme on each of the structures considered is shown in Fig. 6-4 as magenta points. The red and blue points correspond to the catalysis rates on the static positively and negatively polarized structures respectively. We see that the rate of catalysis is significantly improved for the supported one-layer non-polar ZnO and polar ZnO films. For the two-layer and three-layer non-polar ZnO structures, there is little improvement in the catalysis rate by using a tunable catalysis scheme. This result is important as it shows that a difference in adsorption properties of the species on the differently polarized surfaces is not a sufficient condition for a tunable catalysis scheme to enable an increase in reaction rates.

If we draw a volcano plot on the points in Fig. 6-3 as shown in Fig. 6-5, we see that only two structures have points on both sides of the volcano. These are the

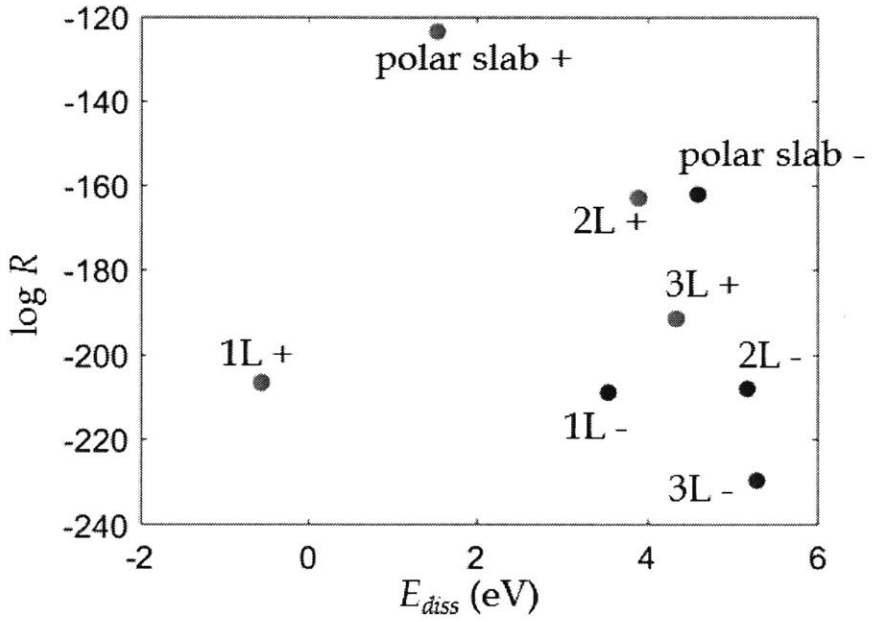


Figure 6-3: Reaction rates for $CO_2$ dissociation over thin-film ZnO supported on positively and negatively poled $PbTiO_3$ (red and blue points, respectively). The notations correspond to the surfaces listed in Table 6.1. The rates are plotted against the dissociative adsorption energy (energy of adsorbed CO+O relative to an isolated $CO_2$ molecule). The point corresponding to the unsupported non-polar slab is not shown in this plot for simplicity, but its value is close to the "3L -" point.

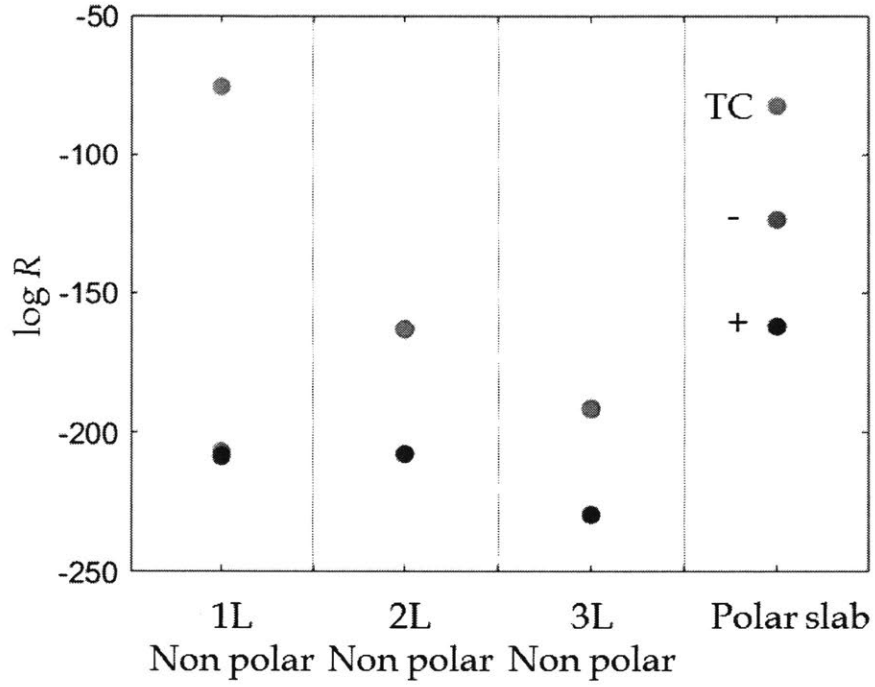


Figure 6-4: Reaction rates for $CO_2$ dissociation over one, two and three-layer non-polar ZnO and polar ZnO. Red, blue and magenta points represent reactions on positively poled, negatively poled and dynamically poled structures respectively.

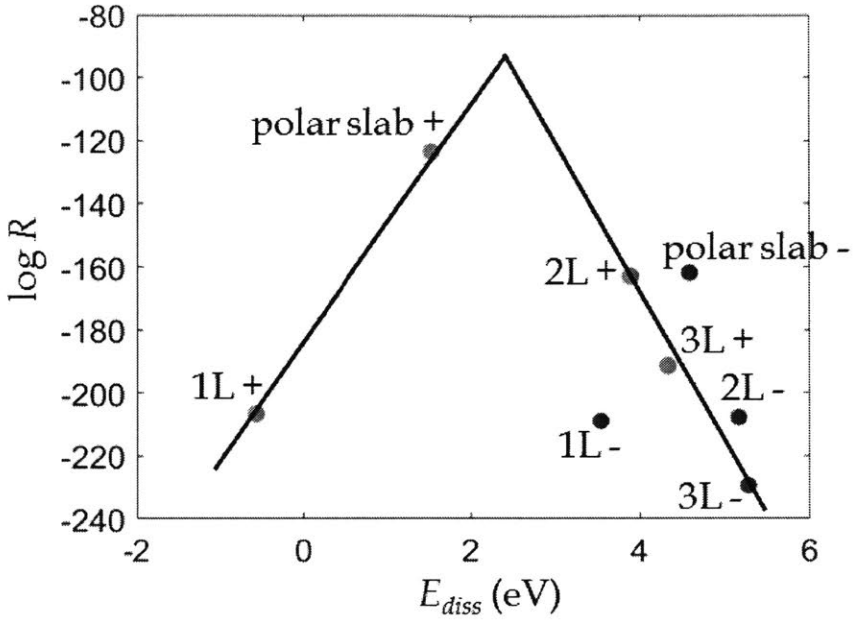


Figure 6-5: Volcano plot drawn over the plot of Fig. 6-3 to develop a hypothesis for the prediction of tunable catalysis.

supported one-layer non-polar and the polar ZnO structure and these are the same points that showed dramatically increased rate of reaction in the tunable catalysis scheme. This leads us to an hypothesis:

**Hypothesis 1.** *A sufficient condition for tunable catalysis is to have the two points corresponding to the activity on the two static surfaces on different sides of the volcano describing the reaction.*

We expound on this hypothesis in detail below.

First, we attempt to understand why the volcano slopes are able to predict the increase in rates in a tunable catalysis scheme. We start with finding a Bronsted-Evans-Polanyi [131, 132] linear relation between the transition state energy $E_{TS}$ and the dissociative adsorption energy $E_{diss}$ for all ZnO surfaces considered, irrespective of the underlying polarization or surface orientation. This BEP plot is shown in Fig. 6-6. We see that there is a near perfect relationship between these quantities, and the relationship is given by $E_{TS} = 0.96E_{diss} + 0.30$. Since the rate of catalysis is a function of only three parameters ($R = R(E_{ads}, E_{TS}, E_{diss})$) of which we can

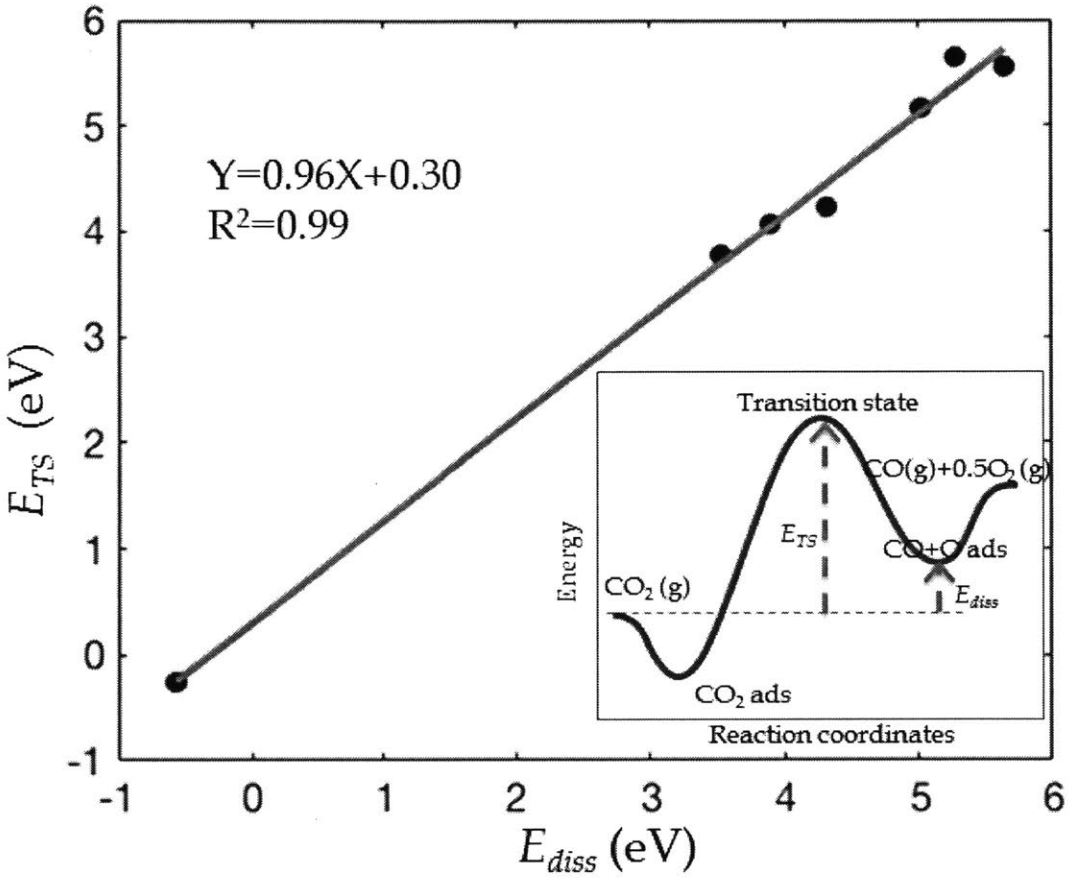


Figure 6-6: Bronsted-Evans-Polanyi relation for catalysis on supported ZnO. The inset shows a definition of the quantities $E_{TS}$ and $E_{diss}$.

relate two of the parameters through a BEP relation. Therefore, we can write $R$ as a function of just two parameters, $E_{ads}$ and $E_{diss}$ which are the easiest to calculate of the three parameters. A plot of $R = R(E_{diss}, E_{ads})$ is shown in Fig. 6-7. We see that this is a 3-D volcano having an absolute peak at around $(E_{diss}, E_{ads}) = (2.65, 0)$ which is the point at which there is zero barrier to desorbing the products after dissociation (i.e $E_{diss} = E_{rxn}$, see Fig. 6-1) while minizing the value of the activation energy $E_a = E_{TS} + E_{ads}$. This is precisely a statement of Sabatier's principle. The rate of reaction (directly correlated with $E_a$) is a competition between the adsorption energy of $CO_2$ and the dissociative adsorption energy, which are both proxies for the activity of the catalyst surface.

For each value of the $CO_2$ adsorption energy $E_{ads}$, there is a value of $E_{diss}$ that results in a peak reaction rate. These series of points are connected by the dashed line in Fig. 6-7(b). The dashed line is the locus of points $E_{ads} = 2.86E_{diss} - 7.57$. When points on the left of this line $(E_{diss}, E_{ads}) = (E^+_{diss}, E^+_{ads})$ are combined with points on the right of the line $(E_{diss}, E_{ads}) = (E^-_{diss}, E^-_{ads})$ to obtain a rate $R_{TC} = R(E^-_{diss}, E^+_{ads})$, the rate is several orders of magnitude greater than both of $R_+ = R(E^+_{diss}, E^+_{ads})$ and $R_+ = R(E^-_{diss}, E^-_{ads})$. When the two points are on the same side of the line, the tunable catalysis rate $R_{TC}$ is not significantly greater than $R_+$. This means that the dramatically increased reaction rates associated with tunable catalysis occurs only when the two points are on either side of the volcano plots, that is, $E^+_{ads} > 2.86E^+_{diss} - 7.57$ and $E^-_{ads} < 2.86E^-_{diss} - 7.57$ for two points $(E^+_{diss}, E^- + _{ads})$ and $(E^-_{diss}, E^-_{ads})$ corresponding to the adsorption properties on the positively and negatively polarized substrates respectively. These conditions are fulfilled by the supported one-layer non-polar ZnO structure and the supported ZnO structure as shown in Fig. 6-7(b), proving our hypothesis 1.

In Fig. 6-8, we show that, for the supported ZnO structures, a relationship between adsorption properties at the two different polarization states of the catalyst is possible. While we do not currently have an explanation for why the relationship should be linear (indeed, we found a quadratic fit to be more appropriate for our data), we do expect a positive correlation between adsorption properties on two structures

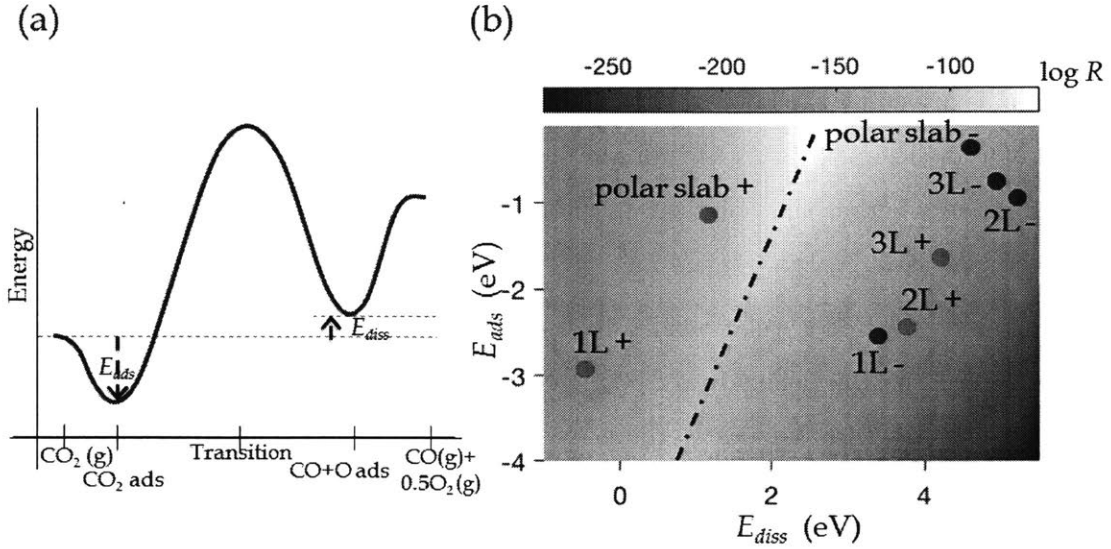


Figure 6-7: 3-dimensional plot of the rate of reaction for all values of $E_{ads}$, the energy of adsorbed $CO_2$, and $E_{diss}$, the energy of adsorbed CO+O. These parameters are depicted in (a) and the rate plot is in (b). The dashed line in (b) is the locus of peak rates for each $E_{ads}$ and is given by $E_{ads} = 2.86E_{diss} - 7.57$.

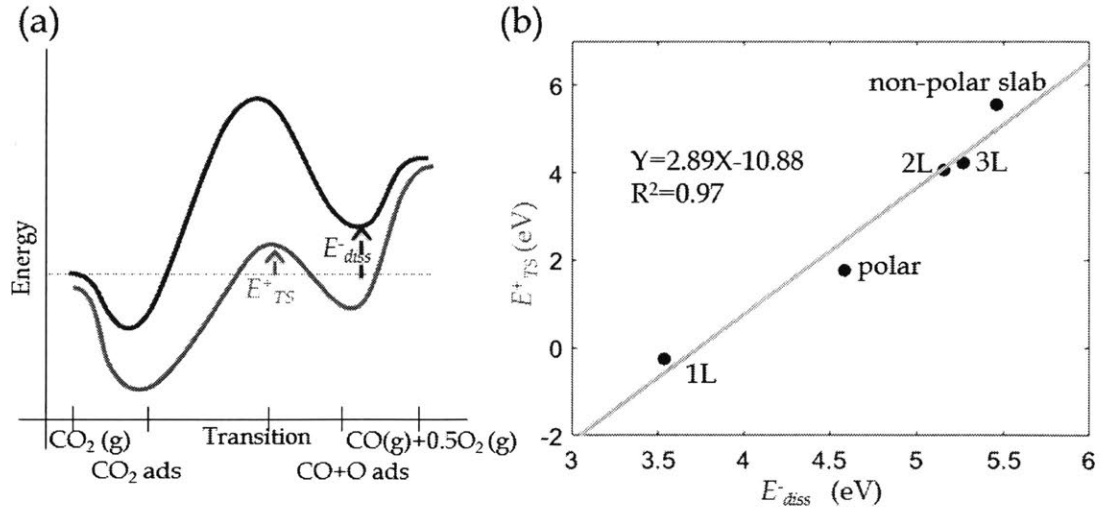


Figure 6-8: An assumed linear relation between $E^+_{TS}$ and $E^-_{diss}$. These quantities are defined in (a) where the red and blue lines represent reaction pathways on positively and negatively polarized structures respectively. The "non-polar slab" point is the special case of a sufficiently thick or non-supported ZnO($11\bar{2}0$) slab for which the substrate polarization has no effect on surface properties, i.e $E^+_{TS}$=$E^-_{TS}$ and $E^+_{diss}$=$E^-_{diss}$.

when the only difference between them is the polarization state. As established in the previous chapter, the difference is surface chemistry on the surfaces at the same polarization is driven by the polarization at the interface, and charges therefore increase or decrease in the epitaxial ZnO thin film layer, relative to a free-standing ZnO film, depending on whether the polarization of the underlying ferroelectric is negative or positive respectively.

As stated, we find a relationship between the transition state energies for the positively polarized and negatively polarized structures, $E_{TS}^{+}$ and $E_{TS}^{-}$ respectively. Since at each polarization state, there is the same BEP relationship between the transition state energy $E_{TS}$ and dissociative adsorption energy $E_{diss}$, this means there is a relationship any two of the parameters in the set ($E_{TS}^{+}$, $E_{TS}^{-}$, $E_{diss}^{+}$, $E_{diss}^{-}$) for the same structure. For simplicity, we show the assumed linear relationship between $E_{TS}^{+}$ and $E_{diss}^{-}$ in Fig. 6-8. This is a dramatic result, as it means the tunable catalytic properties of a structure for $CO_2$ can be completely determined by the adsorption energy of $CO_2$, $E_{ads}$, and the dissociative adsorption energy, $E_{diss}$, *on only one of the polarization states.* This is illustrated in Fig. 6-9. We see the likelihood of a structure to be good tunable catalyst can be predicted by which side of the dashed line (which is the same as in Fig. 6-8) the point falls. That is, improved reaction rates occurs only when $E_{ads}^{+} > 2.86E_{diss}^{+} - 7.57$.

## 6.4 Energy considerations

Below, we perform an analysis of the energetics of the switching process in lieu of increasing the temperature to achieve the same rate of reaction. This analysis builds on the discussion in the previous section.

We define $f_{switch}$ and $E_{switch}$ as the switching frequency and energy required to obtain a rate of reaction $R_{mass}$ respectively:

$$f_s = k_2$$

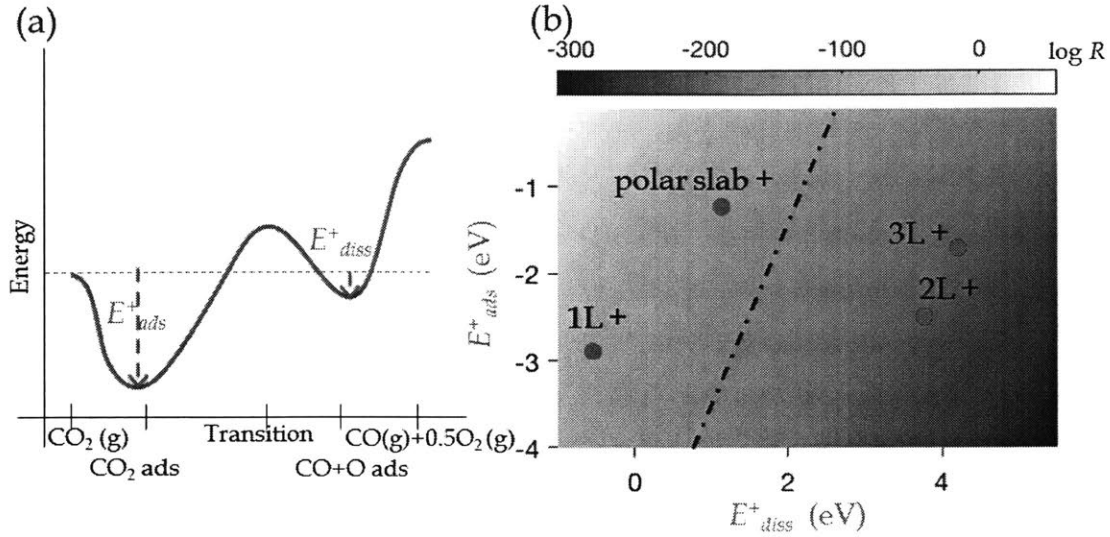


Figure 6-9: Prediction of tunable catalysis rates by calculating adsorption properties on just the positively polarized structure. The definitions of $E^+_{ads}$ and $E^+_{diss}$ are shown in (a) and the calculated reaction rates using the relationship discussed in Figs. 6-6 and 6-8 is shown in (b). The dashed line is the same as in Fig. 6-8. Improved reaction rates occurs only when the point ($E^+_{diss}$, $E^+_{ads}$) is to the left of the line.

because there is no need to switch the slab faster than the rate (turn-over frequency) of the forward reaction.

$$E_{switch} = f_s * d_w * (A_s/a_s) * n_l$$

where $d_w$ is the "well depth" or the energy cost of switching one unit cell thickness of the $2 \times 2 \times n_l$ $PbTiO_3$ subtrate, the surface area of which is $a_s$. $n_l$ is assumed to be 4, a very reasonable value since it is theoretically possible to maintain the polarization in a perovksite film of one unit cell thickness [92].

We calculate the mass flow rate $R_{mass}$ at the given temperature using Eq. 6.5 and the values of $G_1$, $G_3$, $G_4$ and $E_a$ corresponding to the dynamic switching scheme. Instead of using the dynamic switching scheme to achieve this mass flow rate, we can raise the temperature for the reaction chamber and use unsupported ZnO as the catalyst. This temperature can be calculated by fixing the value of $R_{mass}$ and using values of $G_1$, $G_3$, $G_4$ and $E_a$ corresponding to the reaction on the unsupported

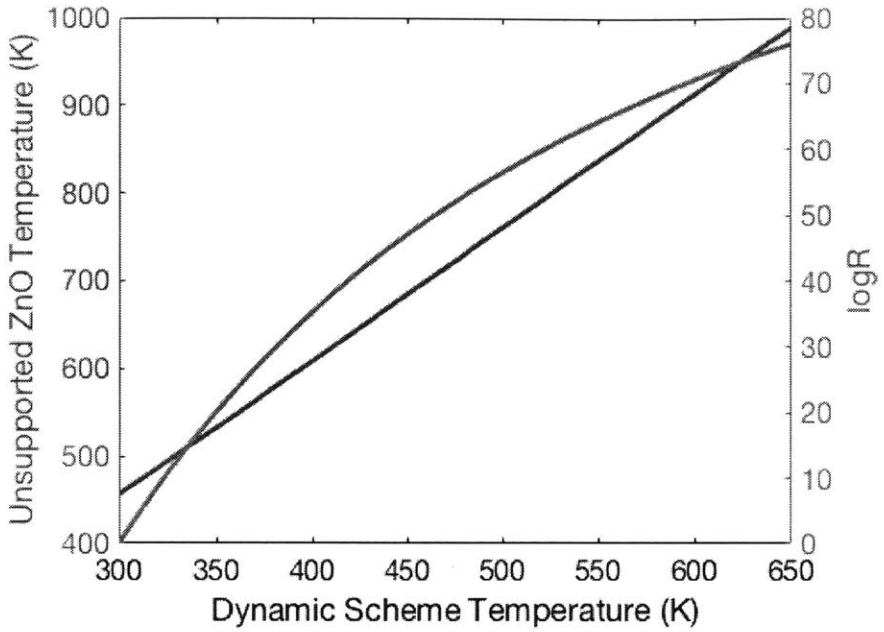


Figure 6-10: Temperatures required to achieve the same rate of reaction on the unsupported ZnO slab (left $y$ axis) and the supported switchable slab (horizontal $x$ axis). The temperature range of the horizontal axis was chosen so that the substrate is always below its Curie point. The reaction rate (right $y$ axis) is shown on a logarithmic scale and normalized so the rate calculated at T=300K is 1.

slab. The temperature for the reaction on the unsupported slab is always higher than on the supported swtichable slab, the difference varying between 157K and 339K at corresponding supported switchable slab ("Dynamic Scheme") temperatures of 300K and 650K respectively. The relationship between the two temperatures are shown in Fig. 6-10.

Next, we calculate the extra energy $E_{heat}$ required to keep the reactants at the higher temperatures on the unsupported ZnO catalyst. Note that we ignore the heat taken up by the catalyst itself and any supporting structures in a real-life reaction chamber.

$$E_{heat} = R_{mass} * c * \Delta T$$

where $c$ is the specific heat capacity of $CO_2$ as obtained from Ref. [133] and $\Delta T$ is the temperature rise required.

We define $F$ as the ratio of $E_{heat}$ to $E_{switch}$. The variation of $F$ with temperature

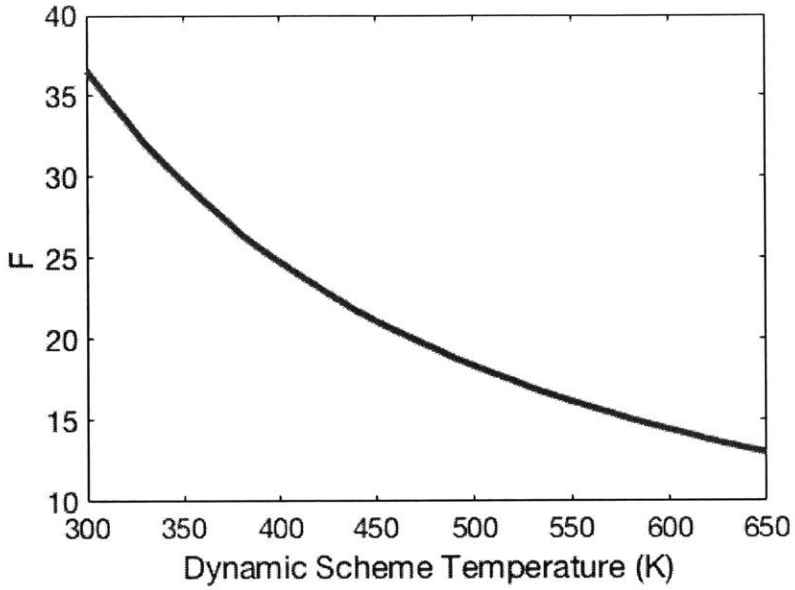


Figure 6-11: Ratio of heating energy to switching energy, $F$ as a function of temperature of the supported switchable slab ("Dynamic Scheme Temperature").

on the dynamic catalyst is shown in Fig. 6-11. We see that there is an advantage in using a dynamic switching scheme in the temperature range considered.

## 6.5 Conclusion

Using a quasi-equilibrium approximation, we show that the dynamic switching scheme will result in several orders of magnitude increase in reaction rates compared to the dissociation on the unsupported slab only for the one-layer non-polar structure and the polar structure. We show that this is because of the points describing the catalysis on those tunable surfaces are on either side of a volcano plot. In addition, we show that it might be possible to reduce the parameter space for evaluating a tunable catalysis scheme from six to two, potentially enabling faster screening of tunable catalysts. Finally, we show that at a given rate, the reaction on the unsupported slab proceeds at 1.5 times the temperature and up to 37 times the energy requirement as that on the unsupported slab. These results clearly demonstrate the potential advantages of dynamically switching the surface properties of a catalyst to enhance the turnover of

a product.

# Chapter 7

# Tunable catalysis of $CO_2$ conversion to methanol and cyclic carbonates

## 7.1 Introduction

As had been explained elsewhere in this thesis, a large energy input is generally required to transform $CO_2$. We could achieve a lower energy requirement for the $CO_2$ conversion by utilizing a high energy co-reactant (e.g $H_2$ rather than $H_2O$) and optimize the reaction towards a low-energy product such as methanol. This is precisely one process we will be studying in this chapter. Even with a careful selection of the reaction, there might be some barrier for the process and the use of a tunable catalysis process as described in previous chapters might be necessary to reduce the activation energy of the reaction. In addition, certain $CO_2$ conversion processes do not have a simple pathway that involves $H_2$ as a reactant. One of these is the cycloaddition of epoxides to $CO_2$ to form cyclic carbonates. However, we find that $CO_2$ is frequently not used in industrial processes. For example, in the industrial production of methanol, a mixture of CO and $H_2$ (syngas) is the primary feedstock. These are are higher in energy and are obtained by secondary conversion from natural gas. Another stumbling block to the adoption of $CO_2$ as a choice reactant is the high energy and financial cost of the conversion process itself. For example, commercial production of cyclic carbonates relies on quaternary ammonium or phosphonium salts

as catalysts which require the use of high temperatures and pressures. This means that $CO_2$ fixation is a net producer rather than consumer of $CO_2$ due to the energy required to heat and pressurize the reactor and reactants. [20].

We will be exploring the tunable catalysis of both processes, methanol and cyclic carbonate synthesis. Methanol is a basic chemical building block of paints, solvents and plastics, and has applications in energy, transportation fuels [15] and fuel cells. It had a global demand of 70 million metric tons and generated $55 billion in economic activity in 2015 [16]. Cyclic carbonates on the other hand are used as chemical intermediates (e.g for dimethyl carbonate production) [17], as aprotic polar solvents [18] and as electrolytes in lithium ion batteries [19].

## 7.2 Methanol synthesis

Previous research has shown experimentally the difference in adsorption properties of methanol on oppositely poled surfaces. Methanol adsorbs more rapidly on positively poled $BaTiO_3$ [46] compared to the negatively poled surface. This is a promising indication of the possible tunable catalysis of the methanol synthesis process. We also know that methanol synthesis can be catalyzed by Cu/ZnO based catalysts [134], which provides a strong reason to attempt tunable catalysis on the tunable ZnO surface. The chemical equation for the synthesis is:

$$CO_2 + 3\,H_2 \longrightarrow CH_3OH + H_2O$$

where $\triangle H^o$ for this reaction is -137.8KJ/mol [135]. However, the formation of methane ($CO_2{}^+{}_4H_2 \longrightarrow CH_4 + 2\,H_2O$, $\triangle H^o = -259.9$KJ/mol) is even more favorable, methane evolution is almost always a competing process in methanol synthesis from $CO_2$ depending on the conditions [136]. Another competing process is the reverse water-gas-shift reaction ($CO_2 + H_2 \longrightarrow CO^+H_2O$, $\triangle H^o = 41.2$KJ/mol) which may be favorable at high temperatures and pressures. In this work, we will be exploring the tunable catalysis of methanol synthesis from $CO_2$ and $H_2$ on tunable

$ZnO(0001)/PbTiO_3$ catalyst and the competing reverse water-gas-shift reaction.

### 7.2.1 Computational methods

As shown in Chapter5 the surface of $ZnO(0001)/PbTiO_3$ is chemically the same as that of a ZnO(0001) slab. Therefore, in our calculations, the catalyst is modeled using an eight-bilayer ZnO slab. Our DFT computations are performed using the plane-wave pseudopotential code Quantum Espresso [94]. Zn- and O-terminated (positively and negatively polarized respectively) $2a \times 2\sqrt{3}a$ surface cell were simulated with 20 Åof vacuum separating the repeating units in the $z$-direction and a dipole correction [97] is applied. The first two ZnO bilayers are fully relaxed and the rest fixed to simulate a thicker slab. For adsorption of molecules on the surface, the adsorbate is placed on several different high-symmetry sites as an initial guess and the minimum energy site is taken. All calculations were performed with an energy cutoff of 35 Ry and a $k$-point mesh of $4 \times 2 \times 1$. We did not passivate the O-termination of the ZnO slab as has been done elsewhere [90, 137, 138], as our calculations with and without the passivation are exactly the same for the surface densities of states and adsorption of all intermediates considered in this work. This can be explained by the self-passivation of the slab as reported in Ref. [139].

We consider the adsorption of $CO_2$, CO, O, COOH, $OCH_2O$, OH, H, $H_2O$, $CH_3OH$, HCOO, HCOOH, $OCH_2OH$, $CH_2O$, $CH_3O$, HCO and $CO_3$. These are the expected intermediates in the $CO_2$ conversion process to methanol or syngas.

### 7.2.2 Results and discussion

#### Adsorption properties on Zn- and O- terminated surfaces

As expected, we find differences in energy and molecular orientation or configuration of the adsorbed species on the Zn- and O-terminated surfaces. Figure 7-1 shows the configuration of the $CO_2$ molecule adsorbed on either surface. We see that the molecule maintains its linear form when adsorbed on the O-terminated surface, compared to its buckling when adsorbed on the Zn-terminated surface. This indicates

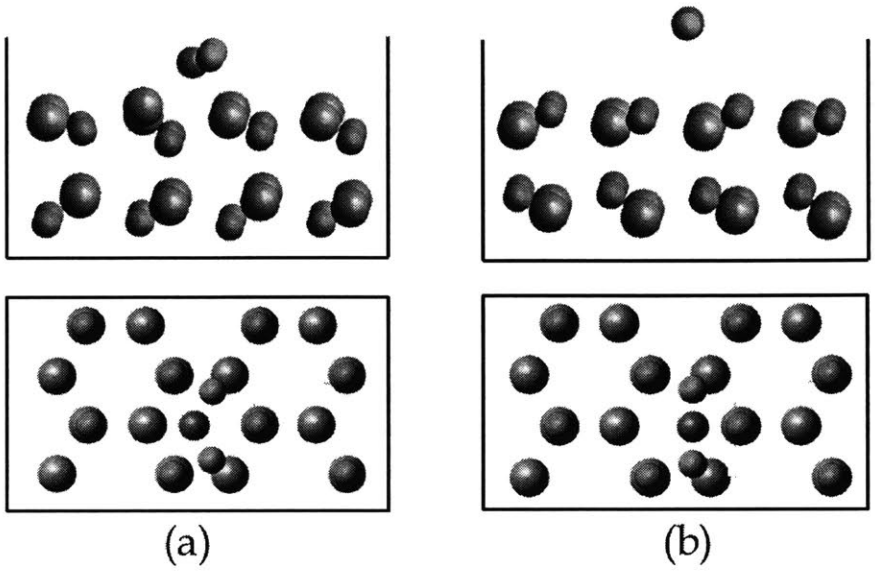


Figure 7-1: Atomic geometry of $CO_2$ adsorption shown with side and top views of all unconstrained atoms for (a) Zn-terminated ZnO(0001) and b) O-terminated ZnO($000\bar{1}$). The geometry for other adsorbates are shown in figures in Appendix A.

stronger adsorption on the Zn-terminated surface. The values of the formation energies for all adsorbed species is shown in Table 7.1, where $E_f$ is defined as:

$$E_f = E_{slab+ads} - E_{slab} - \sum n_i \mu_i \tag{7.1}$$

where $E_{slab+ads}$ is the ground-state energy of the surface and adsorbate, $E_{slab}$ is the ground state energy of the surface slab, and $n_i$ is the number of atoms of species $i$ in the adsorbate. The reference energies, $\mu_i$ are given by:

$$\mu_C = E_{\mathrm{CO_2}} - 2 \times \mu_O$$
$$\mu_H = \tfrac{1}{4}(E_{\mathrm{CH_3OH}} - \mu_C - \mu_O)$$
$$\mu_O = E_{\mathrm{H_2O}} - E_{\mathrm{H_2}}$$

where we obtain the $E_{mol}$'s from the DFT energies of the isolated molecules.

In our calculations, we ignore all entropy corrections for simplicity.

| Species | $E_f$ (eV) \| Zn-ZnO(0001) | $E_f$ (eV) \| O-ZnO(0001) | Difference (eV) |
|---|---|---|---|
| $CO_2$ | 0.00 | 0.00 | 0.00 |
| CO | 0.91 | 0.91 | 0.00 |
| $H_2$ | 0.55 | 0.55 | 0.00 |
| $O_2$ | 4.89 | 4.89 | 0.00 |
| $H_2O$ | 0.55 | 0.55 | 0.00 |
| $CH_3OH$ | 0.00 | 0.00 | 0.00 |
| $CO_2*$ | -2.17 | -1.07 | -1.10 |
| $CO*$ | -0.72 | -0.11 | -0.62 |
| $O*$ | -0.06 | 3.37 | -3.44 |
| $COOH*$ | -1.46 | -2.33 | 0.87 |
| $OCH_2O*$ | -2.22 | -0.28 | -1.94 |
| $OH*$ | -0.74 | 3.26 | -4.00 |
| $H*$ | 0.05 | -1.70 | 1.75 |
| $H_2O*$ | 0.34 | 0.69 | -0.35 |
| $CH_3OH*$ | -0.79 | -0.39 | -0.41 |
| $HCOO*$ | -2.69 | 1.35 | -4.04 |
| $HCOOH*$ | -0.70 | -0.60 | -0.10 |
| $OCH_2OH*$ | -1.48 | 0.87 | -2.34 |
| $CH_2O*$ | -1.64 | -0.01 | -1.63 |
| $CH_3O*$ | -1.52 | 0.55 | -2.07 |
| $HCO*$ | -1.01 | -2.36 | 1.35 |
| $CO_3*$ | -3.23 | 3.52 | -6.75 |

Table 7.1: Formation energies of all species with respect to the two surfaces (Zn-terminated ZnO(0001) and O-terminated ZnO(000$\bar{1}$)).

### Surface thermodynamics

The configuration of exposed surfaces depend on the environment, or more specifically, the chemical potentials of species interacting with the surfaces. In environments containing water, for example, it has been shown that the Zn-termination will be covered by hydroxyl ions [140]. For methanol synthesis however, the surface configuration will be different as there are C species in addition to O and H species. In Figure 7-2, we show the surface phase diagram depicting the most stable adsorbate at varying potentials, directly correlated to pressures, of $H_2$ and $CO_2$. The temperature is 300K and all gases have pressure of 1 bar. The chemical potentials of C, H and O are related to those of $CO_2$, $H_2$ and $H_2O$ by:

$$\mu_C = \mu_{CO_2} + \Delta\mu_{CO_2} - 2 \times \mu_O$$
$$\mu_H = \tfrac{1}{2}(\mu_{ceH2} + \Delta\mu_{H_2})$$
$$\mu_O = \mu_{H_2O} + \Delta\mu_{H_2O} - 2 \times \mu_H$$

which are plugged into the earlier equations to obtain the formation energy for each surface. The relationship between $\Delta\mu_f$'s and pressures is given by:

$$\Delta\mu_j = k_B T \ln \frac{P_j}{P_0} \tag{7.2}$$

where $k_B$ is Boltzmann's constant, T is the temperature and $P_0$ is the reference pressure.

Fig. 7-2 shows that at low $CO_2$ pressures the Zn-terminated surface will be terminated with adsorbed oxygen, or hydroxyl while the O-terminated surface will be terminated with H or $H_2O$. As expected, species containing all of H, C and O, such as $CO_3$, $CH_3O$ and CHO are stabilized at higher $CO_2$ and $H_2$ pressures. This is consistent with experimental work which show the presence of these species on ZnO surfaces [141, 142, 35, 143]. We use this information to guess the most likely pathway for methanol synthesis on the surfaces.

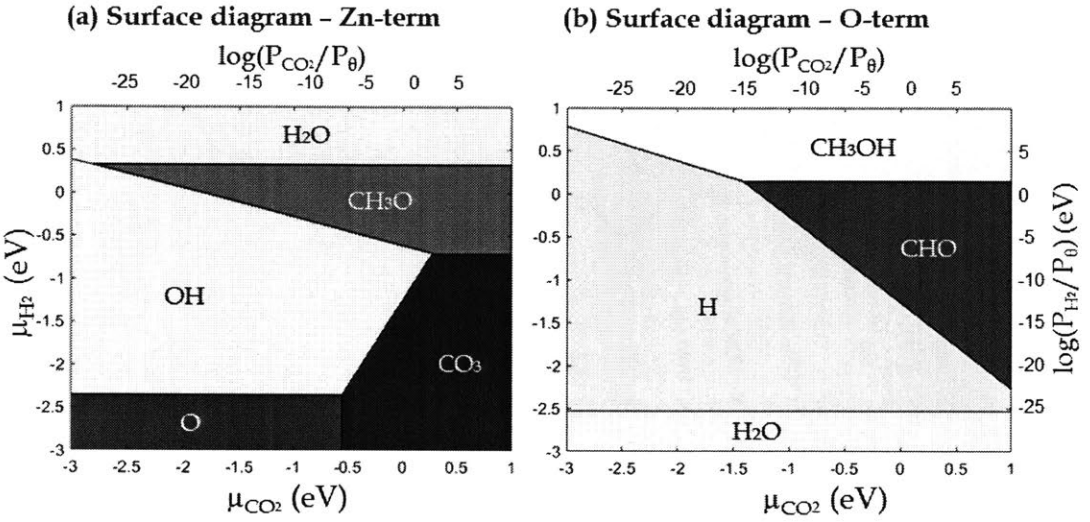


Figure 7-2: Surface phase diagram as a function of $CO_2$ and $H_2$ chemical potential for (a) Zn-terminated ZnO(0001) and (b) O-terminated ZnO(000$\bar{1}$). $\Delta\mu = 0$ corresponds to the standard pressure of 1 bar.

### Energy profiles and tunable catalysis analysis

The pathway for methanol synthesis on metals and oxides is quite involved. We have chosen pathways that have been shown to be feasible on Zn-terminated ZnO [138]. The intermediates along the pathways are also preferred surface species at reasonable reaction temperatures and pressures as shown in Fig. 7-2. The reaction steps are:

$H_2 + 2\,*_h \longrightarrow 2\,H*$

$CO_2 + * \longrightarrow CO_2*$

$CO_2* + H* \longrightarrow COOH* + *_h$

$CO_2* \longrightarrow CO* + O*$

$HCOO* \longrightarrow HCO* + O*$

$HCOO* + H* \longrightarrow HCOOH* + *_h$

$HCOOH* \longrightarrow CH_2O* + O*$

$HCOOH* + H* \longrightarrow CH_2OOH* + *_h$

$CH_2OOH* \longrightarrow CH_2O* + OH*$

$CH_2O* + H* \longrightarrow CH_3O* + *_h$

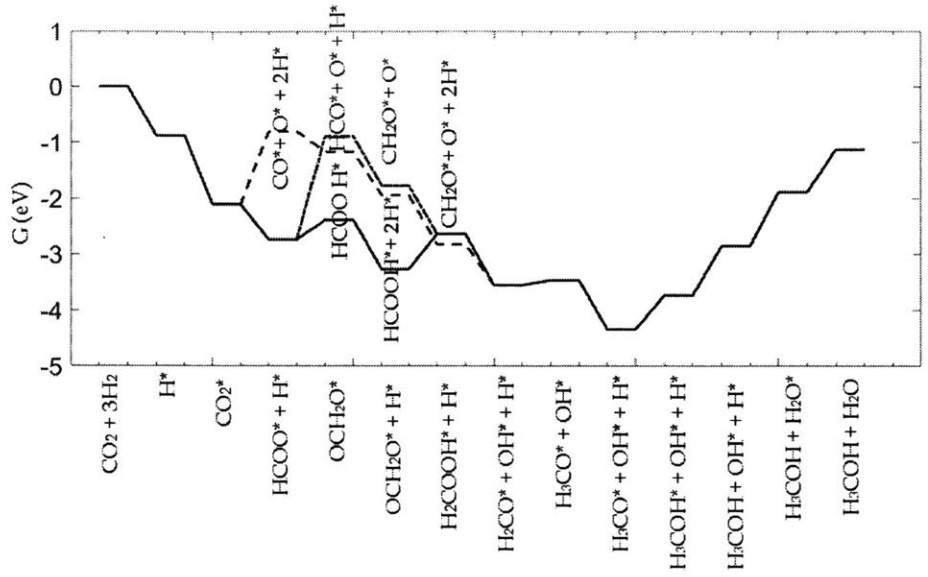


Figure 7-3: Reaction pathways for methanol synthesis over Zn-terminated ZnO(0001). The $x$-axis denote the pathway along the solid line.

$CH_3O* + H* \longrightarrow CH_3OH* + *_h$

$CH_3OH* \longrightarrow CH_3OH + *$

$OH* + H* \longrightarrow H_2O* + *_h$

$H_2O* \longrightarrow H_2O + *$

where $*$ is a regular surface site and $*$ is a special site for H adsorption.

Three pathways are shown in 7-3 and 7-4 for the Zn-terminated and O-terminated surfaces respectively. The energetics for the expected dominant pathway in a tunable catalysis scheme is shown in Fig. 7-5. We see that the energetics are very different on either surface, and a tunable catalysis scheme (denoted by the upward arrow) can be designed. The effective pathway for the dynamically tunable catalysis scheme is shown in Fig. 7-6. The net effect of the scheme is to present a downhill pathway that reduces the free energy of the overall reaction by an impressive 14.5 eV. For a regular non-tunable catalyst, such a change in the free energy of a reaction is achieved by increasing the temperature and pressure of the system. As discussed in Chapter 6, this could be energetically unfavorable, undesirable or both.

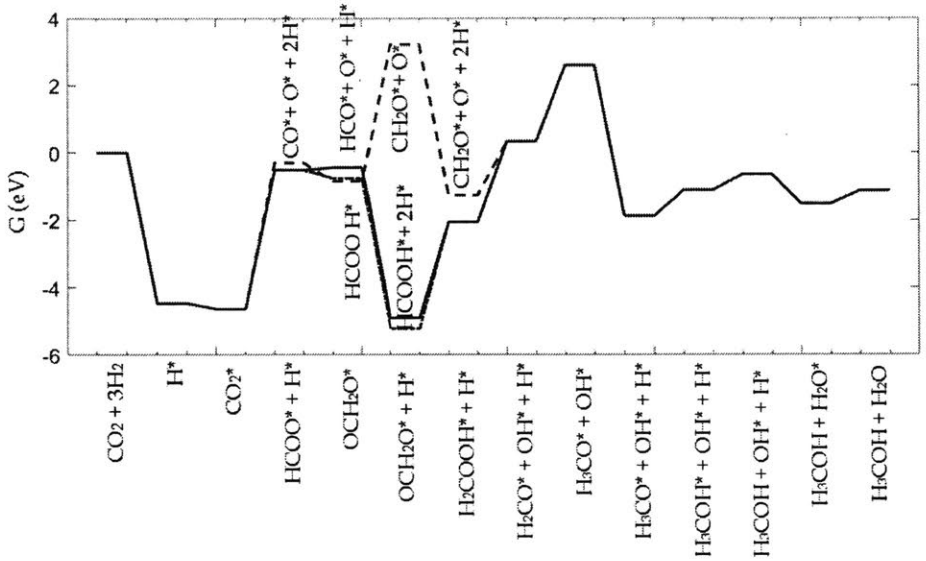


Figure 7-4: Reaction pathways for methanol synthesis over O-terminated ZnO($000\bar{1}$). The $x$-axis denote the pathway along the solid line.

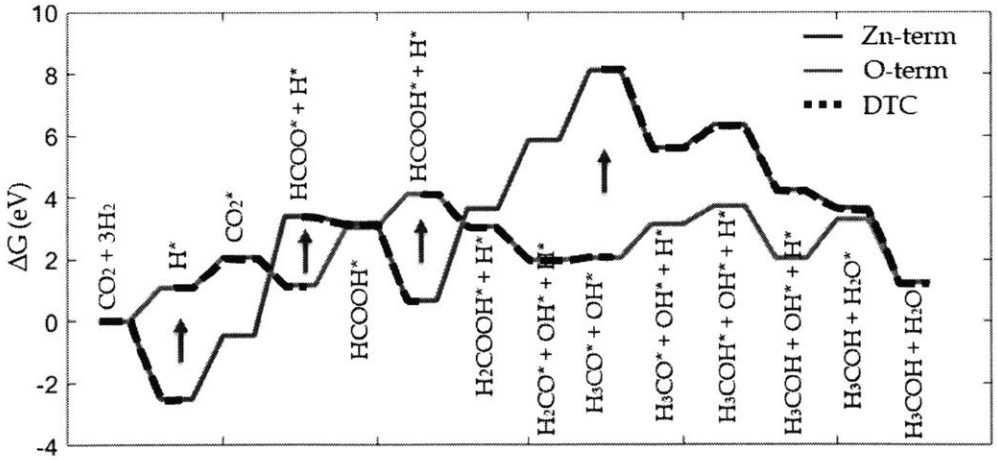


Figure 7-5: Comparison of the energetics of a selected pathway for methanol synthesis over Zn- and O-terminated ZnO(0001) surfaces, and the minimum-energy dynamically tunable catalysis (DTC) pathway when the surface states of the ZnO are constantly switched.

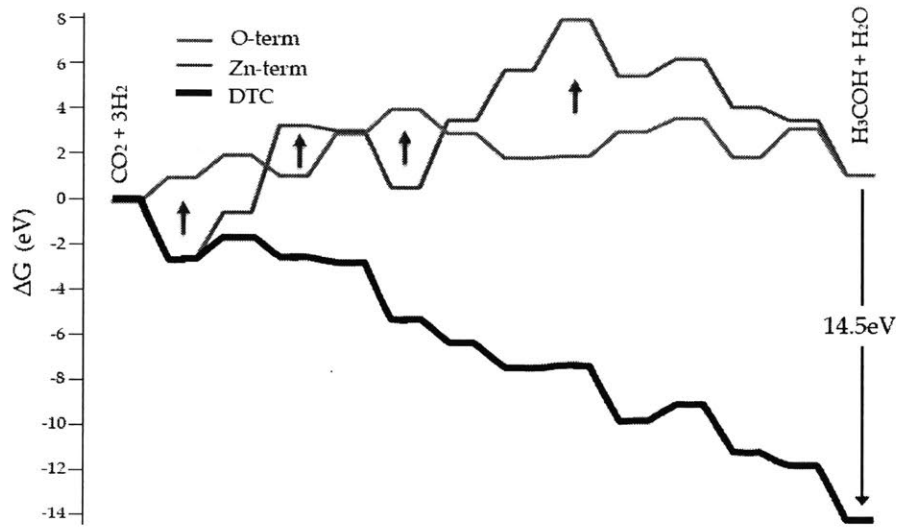


Figure 7-6: This is similar to Fig. 7-5 except that the effective DTC pathway is explicitly illustrated. We see the DTC enabled a 14.5 eV reduction in the free energy of the reaction without a change of the temperature.

## 7.3 Cyclic carbonate synthesis

A fairly large number of catalysts have been studied for the conversion of $CO_2$ to cyclic carbonates. These can be roughly classified into ionic liquids (such as 1-n-butyl-3-methylimidazolium [144] and solid catalysts such as magnesium oxide [145]. In the latter, the conversion process is a simple adsorption and addition, as shown in Fig. 7-7. We assume that the reaction is similar on ZnO surfaces. The scheme relies on the activation of $CO_2$ which is better on the Zn-terminated polar surface than the O-terminated surface on which the $CO_2$ molecule is still linear. We therefore expect more favorable energetics on the Zn-terminated surface as we have found for $CO_2$ dissociation and methanol synthesis.

### 7.3.1 Computational methods

The DFT calculation setup for the cyclic carbonate synthesis is similar to that described for methanol synthesis in the previous section. We perform adsorption cal-

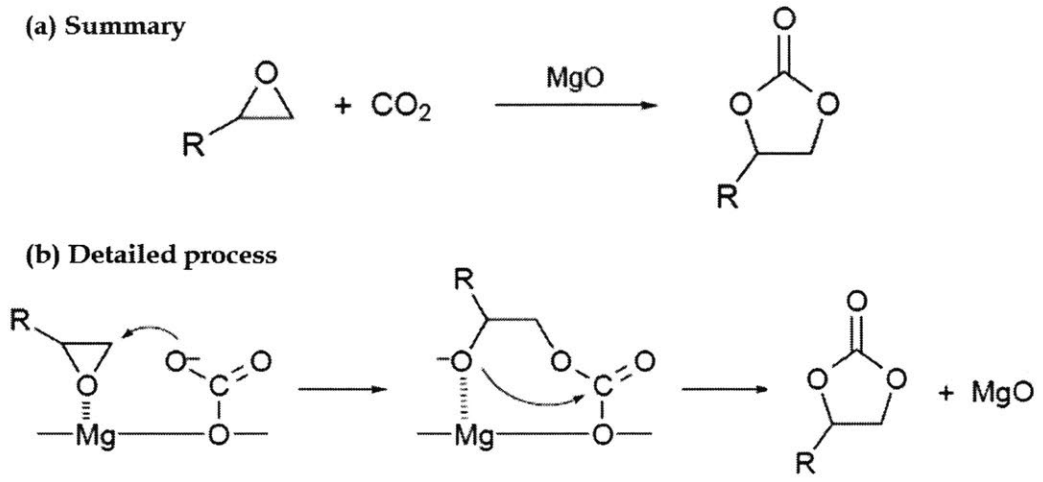


Figure 7-7: Scheme for the synthesis of cyclic carbonates from epoxides and $CO_2$ on a MgO catalyst.

culations for $CO_2$, $(CH_2)_2O$ (ethene oxide) and $(CH_2O)_2CO$ (ethene carbonate) and compare the energetics at each step to that of the isolated reacting molecules. In our calculations, we ignore all entropy corrections for simplicity.

### 7.3.2 Results and discussion

#### Adsorption properties and energy profiles on Zn- and O- terminated surfaces

As expected, we find differences in energy and molecular orientation or configuration of the adsorbed species on the Zn- and O-terminated surfaces. The pathway for ethene carbonate synthesis is as follows: $CO_2 + * \longrightarrow CO_2*$

$(CH_2)_2O + * \longrightarrow (CH_2)_2O*$

$CO_2* + (CH_2)_2O* \longrightarrow (CH_2O)_2CO*^+*$

$(CH_2O)_2CO* \longrightarrow (CH_2O)_2CO + *$

where $*$ is a surface site.

The energetics for the expected dominant pathway in a tunable catalysis scheme

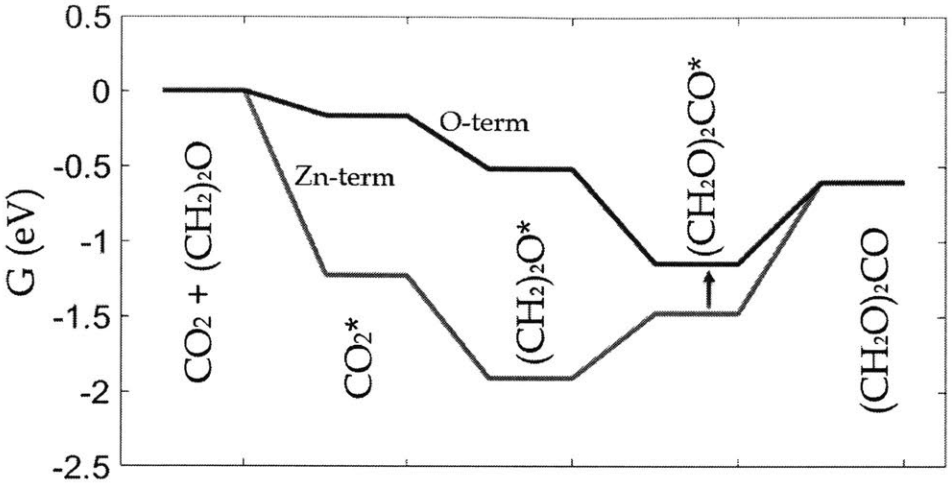


Figure 7-8: Comparison of the energetics of of ethene carbonate synthesis over Zn- and O-terminated ZnO(0001) surfaces.

is shown in Fig. 7-8. We see that the energetics are different on either surface, and a tunable catalysis scheme (denoted by the upward arrow) can be designed.

## 7.4 Conclusion

We have demonstrated the potential utilization of tunable catalysis to enable faster reaction rates for methanol and cyclic carbonate synthesis at mild conditions. Further work needs to be done to correct the energies for accurate calculation of reaction rates comparable to expected experimental measurements.

# Chapter 8

# Summary, limitations and outlook

*A few paragraphs of this chapter were published in a previous work [82].*

## 8.1 Summary

$CO_2$ is a very stable molecule and does not partake in reactions without some form of activation, usually on a catalyst. Chemical conversion of $CO_2$ is however important to avoid global warming as we continue to rely on fossil fuels for some of our energy needs. Like for other chemical reactions, the selection of a catalyst for $CO_2$ conversion processes is limited by Sabatier's Principle.

We proposed a dynamically tunable catalyst for $CO_2$ conversion which should enable catalytic activity beyond that predicted to be the maximum based on Sabatier's Principle. Tunable catalysis is not a new concept, but it is not well understood and most already-proposed tunable catalysts are not practical. We design around the limitations of the proposed catalysts. Our ZnO/$PbTiO_3$ catalyst is practical and the growth has even been demonstrated experimentally. In our work, we evaluated the possible configuration of ZnO on $PbTiO_3$. We find that the catalytic activity on non-polar ZnO supported on $PbTiO_3$ is dependent on the thickness of the oxide thin film and the polarization of the perovskite support. Unfortunately, beyond four atomic layers of the ZnO film, we find no potential for tunable catalysis for the orientation of ZnO.

We next evaluated the potential of polar ZnO grown on $PbTiO_3$ as a tunable catalyst. We show that the surface chemistry of the film consistently follows the polarization of the substrate. This is effectively the first theoretical demonstration of ferroelectricity in ZnO, which has important implications for device applications. For both the polar and non-polar films, we evaluated $CO_2$ reduction to CO and to $CH_3OH$ to demonstrate the utility of tunable catalysis to improve reaction rates at mild conditions.

Finally, we proposed criteria and methods for evaluating *a priori* the effectiveness of a proposed tunable catalyst using just two DFT calculations. This contribution is important for the acceleration of tunable catalysis research, reducing the time taken to evaluate a particular catalyst from 2-3 years to just a month or two.

## 8.2 Limitations and implied approximations

### 8.2.1 Rate and effect of polarization reversal in the perovskite

In our work, we took it for granted that the polarization of the catalyst can be switched as fast as we need it to. This was for mathematical convenience but it cannot be ignored in practice. Another area for further exploration is the effect of the fast polarization reversal on the integrity of the ZnO film. Does the film deform by "lift off" or agglomeration on the substrate during fast switching of the electric field? How fast is "fast" for the deformation to happen? These are largely experimental questions which we hope our experimental colleagues can work on.

### 8.2.2 Effect of the non-stoichiometric composition of the catalyst

In our work, we assumed that the ZnO film and the $PbTiO_3$ substrate are pristine, and do not have interstitials, vacancies or atom substitutions. This is of course unlikely in practice. Since we expect that there will be excess oxygen during growth and operation of our catalyst, below, we evaluate the case of the non-stoichiometric

$ZnO(11\bar{2}0)/PbTiO_3$ catalyst where there is an oxygen interstitial at the interface between the film and substrate.

We first investigate possible thermodynamic ground states of the heterostructure . Figure 8-1 is a plot of the free energy of formation for inserting an oxygen into the space created at the interface by the unmatched stacking of atomic layers. Our results show that under growth regular conditions (T=400-700  and P=$10^{-5}$Pa [4] at which $\mu_O \approx -1.1 - -1.5$eV) an extra oxygen will remain at the interface when the subtrate is positively polarized. On the negatively polarized structure, this non-stoichiometric structure is only stable at lower temperatures.

In order to decide whether or not the structure with an extra oxygen is relevant for our $CO_2$ dissociation calculations, we perform calculations for the energy required to have an oxygen vacancy in each ZnO layer in the 4-layer-thick supported-ZnO case. Figure 8-2(a), which shows the O vacancy formation energy in each layer for this film, suggests that after a number of layers have been grown, the configuration at the interface will be maintained irrespective of the thermodynamic stability of the structure. If an oxygen is already trapped at the interface (for example, if the film is grown over a positively polarized substrate and the polarization was later switched), its removal will involve a series of steps that include the removal of one of the topmost oxygen atoms. Given the high vacancy formation energies of ~3.5eV, this process will be kinetically limited. Conversely, if there is no oxygen at the interface (for example, growing the under a negatively polarized substrate and the polarization was later switched), oxygen insertion will involve one of the oxygen atoms in the lowest ZnO layer moving to the interfacial O location and leaving behind a vacancy. In our calculations, we do not observe a stable system with this configuration.

However, the above considerations do not take into account the effect of other gas phase molecules in the environment. For $CO_2$ dissociation, for example, CO adsorption also occurs. Our calculations show that if an oxygen atom exists at the interface, it can be easily removed by adsorption of a CO molecule, as illustrated in figure 8-2(b) for $n = 1$ and 2. This suggests an interesting application of non-stoichiometric $(ZnO)_n/PbTiO_3\uparrow$ for small $n$: catalytic oxidation of CO to $CO_2$, since

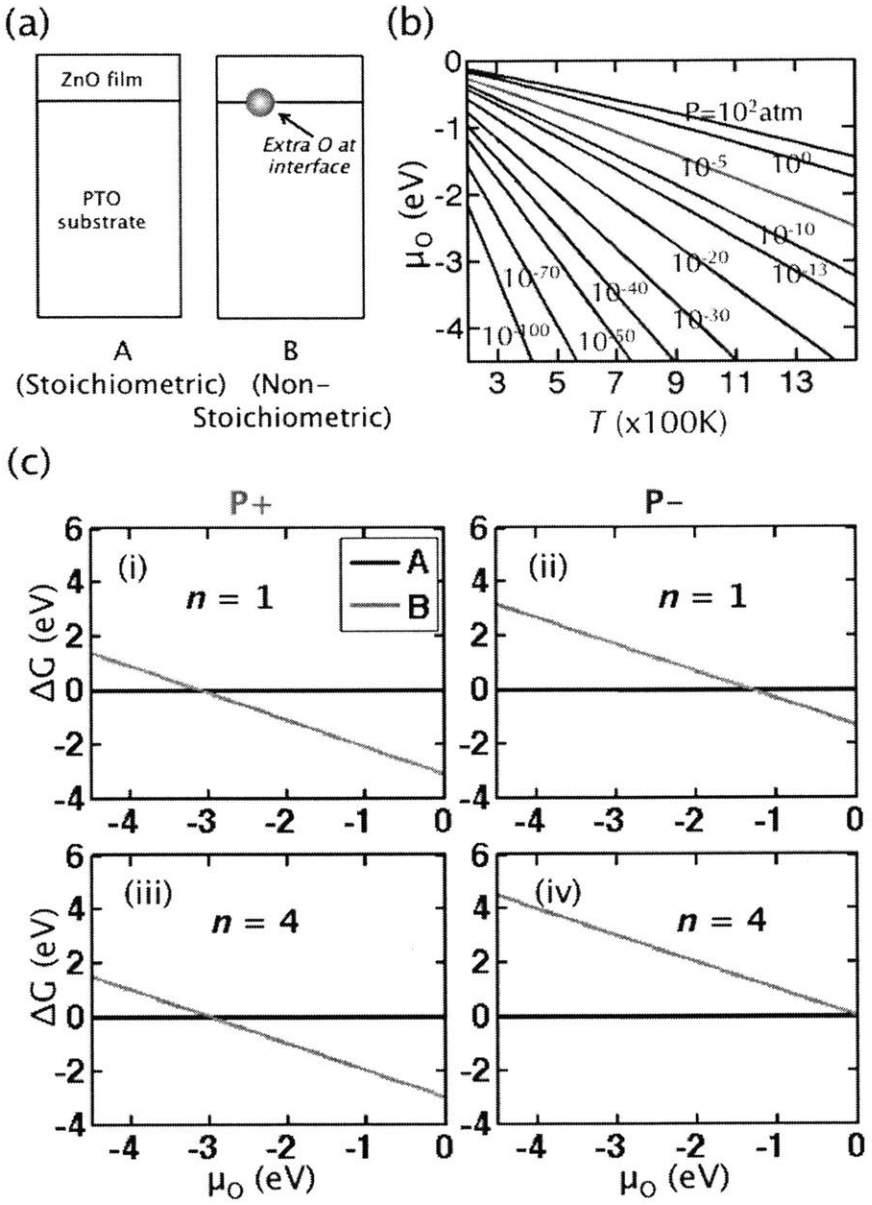


Figure 8-1: (a) Possible configurations in an oxygen-rich environment. (b) Oxygen chemical potential as a function of temperature and pressure. (c) Free energy versus oxygen chemical potential for $n = 1$ and $n = 4$. Shaded regions represent the range of $\mu_O$ under the growth conditions reported in Ref. [4] is $10^{-5}$Pa (highlighted line) and $400 < T < 700$ . $\mu_O$ can be decreased by reducing pressure and increasing temperature.

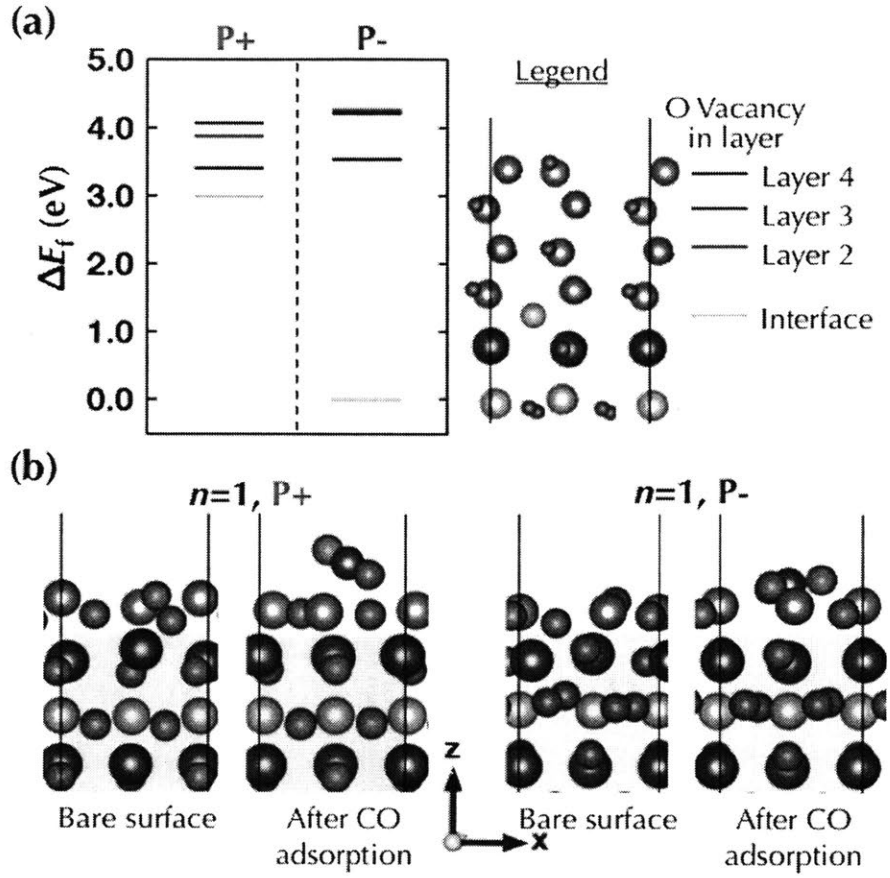


Figure 8-2: (a) Oxygen vacancy formation energy, $\Delta E_f$, as a function of distance from the interface. The presence of an extra O at the interface is predicted to be determined by the initial growth configuration. (b) Atomic structure of CO on the non-stoichiometric $(ZnO)_1/PbTiO_3\uparrow$ and $(ZnO)_1/PbTiO_3\downarrow$, demonstrating the selective removal of interfacial O by the adsorbing CO. Atom colors are the same as in Fig. 4-1, with adsorbate O atoms shown in magenta for clarity.

interface stability dictates that the non-stoichiometric interface will exist as long as there is $O_2$ gas in the atmosphere at most conditions encountered in practice, and this structure easily oxidizes CO.

The foregoing also suggests that it is possible to obtain a stoichiometric interface if the ZnO thin film is grown at the negatively-polarized structure under conditions of lower oxygen partial pressure and/or higher temperature (i.e., lower oxygen chemical potential, $\mu_O$). This configuration will be trapped when the polarization of the substrate is switched with an electric field. In the following, we perform calculations to

explore $CO_2$ dissociation on the surfaces of this structure as a function of polarization direction and ZnO film thickness. We then show that a dynamically tunable scheme using this heterostructure can enable a much lower overall activation energy for the $CO_2$ dissociation process.

Therefore, we conclude that even though the presence of a single oxygen interstitial in a centred $2 \times 2$ cell is sufficient to give dramatically different results from that reported in Chapter 4, there is a way to ensure stoichiometric growth in practice.

## 8.3 Outlook and future work

Our work is just the beginning of deep explorations into the potential applications of dynamically tunable catalysis. To expand the body of work, we suggest the following directions for future researchers:

1. The evaluation of other oxide-perovskite systems, to determine the universality or otherwise of the results obtained in this thesis, especially those of Chapter 6.

2. Experimental work to determine the effect of fast polarization reversal on the integrity of the oxide film.

3. A more rigorous address of the question of impurities in the oxide-perovskite catalyst system. In this chapter, we evaluated the case of the presence of oxygen interstitials. In real systems, the imperfections in the system will be largely dependent on the method of growth of the catalyst and the enviromental conditions. This creates a wide variety of possibilities for the catalyst configuration.

4. Theoretical and experimental work to extend our results to other important chemical reactions.

We explore the first item, the evaluation of thin-film oxide-perovskite systems, in some detail. Obvious systems to explore are 1. Bare surfaces of $PbTiO_3$ slabs which are effectively single layer $TiO_2$ or PbO supported on PbO- or $TiO_2$-terminated $PbTiO_3$ substrates respectively, and 2. 1, 2 and 3-layer non-polar ZnO and few layer

| Material | Lattice constant (Å) | Space group |
|---|---|---|
| Nickel oxide | 4.17 | Fm3m |
| Niobium (II) oxide | 4.2 | Pm3m |
| Lead oxide | 4.0 | P4/nmm |
| Magnesium oxide | 4.2 | Fm3m |
| Germanium dioxide | 4.1 | Pbcn |
| Molybdenum oxide | 3.9 | Pbnm |

Table 8.1: Sample binary oxides which have epitaxial matching to the surface of typical tetragonal perovskites. Hexagonal perovskite have a fairly wide range of lattice constants and can be matched to even more oxides.

polar ZnO supported on $TiO_2$-terminated $PbTiO_3$ substrate. (Recall that all the calculations reported in the previous chapters had PbO-terminated substrates.) By performing $CO_2$ adsorption and dissociation calculations on the suggested surfaces, we add another 12 points to the graphs in Chapter 6.

The research can be extended by considering binary oxides that can be grown on perovskites, as shown in Table 8.1. The choice of the perovskite substrate depends on the desired polarization and the expected feasibility of the epitaxial growth on the substrate. More oxide-perovskite epitaxial pairs can be found by considering hexagonal perovskites (e.g $BiFeO_3$ or $ZnSnO_3$) and matching oxides.

# Appendix A

# Appendix for Chapter 7

## A.1 Adsorption geometries on Zn- and O-terminated ZnO(0001)

All the atomic geometries are presented in Figures A-1-A-15. Energies of all structures are provided in Chapter 7. In all the figures, the oxygen atoms are colored magenta to differentiate them from oxygen atoms in the substrate which are colored red.

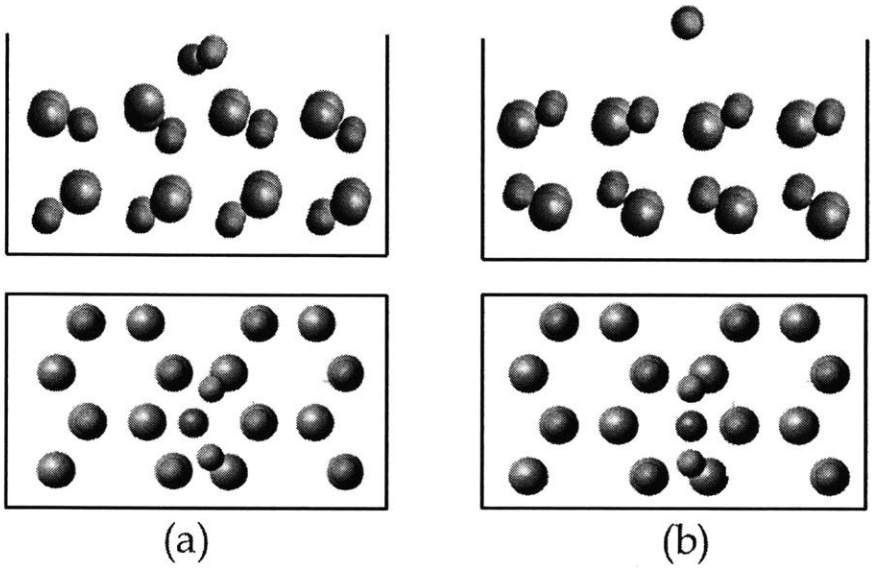


Figure A-1: Atomic geometry of $CO_2$ adsorption shown with side and top views of all unconstrained atoms for (a) Zn-terminated ZnO(0001) and b) O-terminated ZnO($000\bar{1}$).

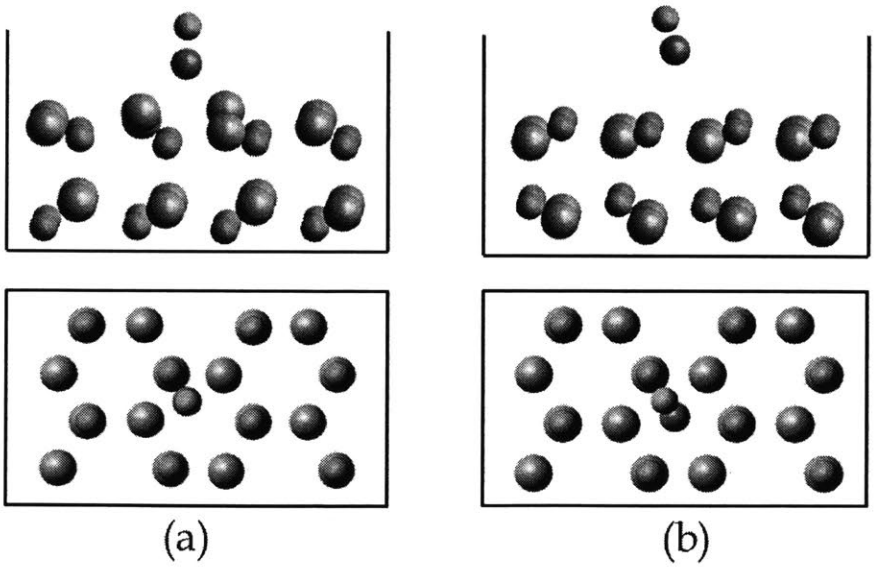


Figure A-2: Atomic geometry of CO adsorption shown with side and top views of all unconstrained atoms for (a) Zn-terminated ZnO(0001) and b) O-terminated ZnO($000\bar{1}$).

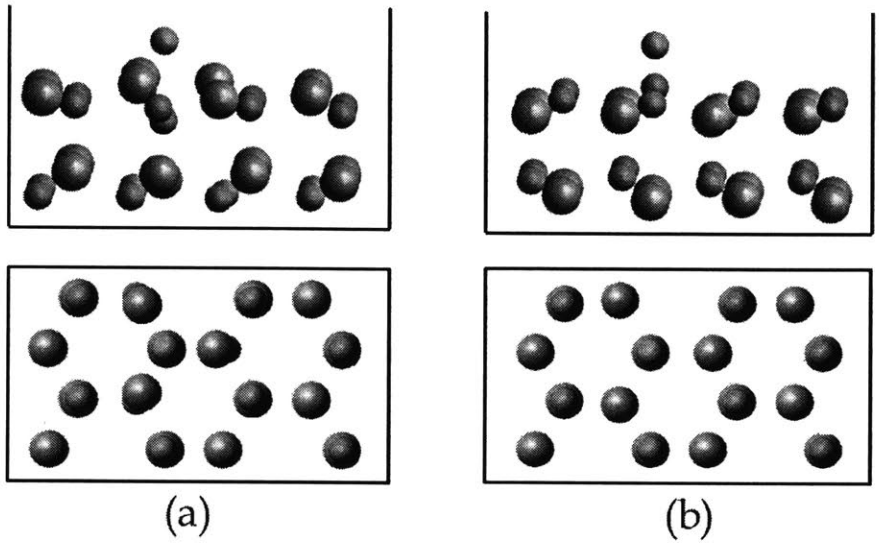


Figure A-3: Atomic geometry of O adsorption shown with side and top views of all unconstrained atoms for (a) Zn-terminated ZnO(0001) and b) O-terminated ZnO($000\bar{1}$).

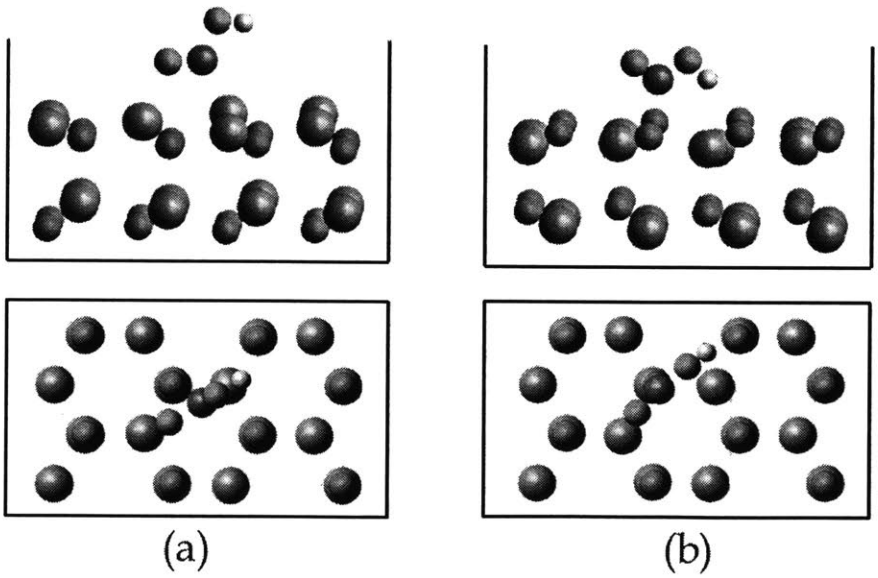


Figure A-4: Atomic geometry of COOH adsorption shown with side and top views of all unconstrained atoms for (a) Zn-terminated ZnO(0001) and b) O-terminated ZnO($000\bar{1}$).

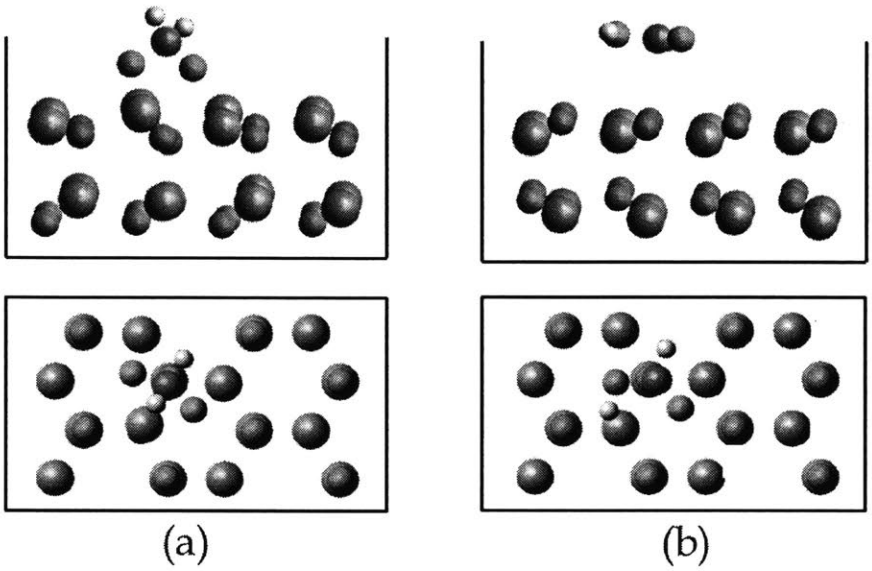


Figure A-5: Atomic geometry of $OCH_2O$ adsorption shown with side and top views of all unconstrained atoms for (a) Zn-terminated ZnO(0001) and b) O-terminated ZnO(000$\bar{1}$).

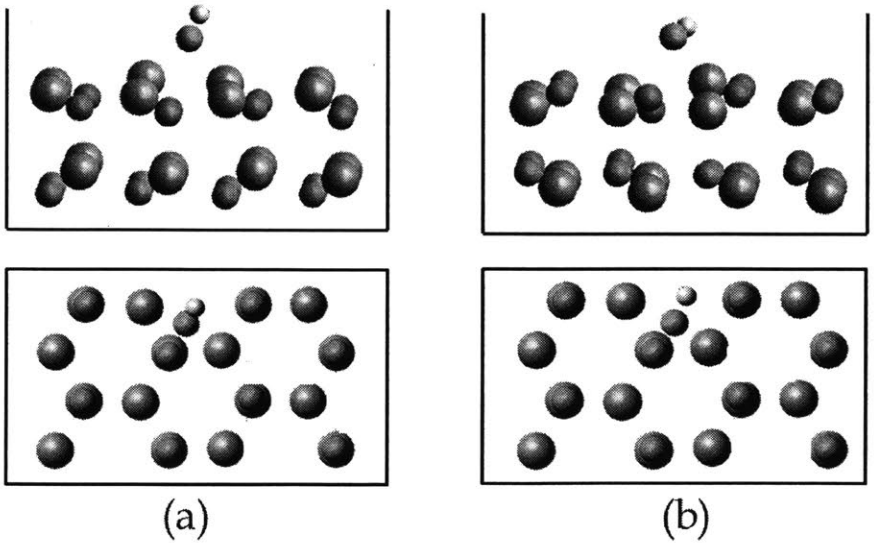


Figure A-6: Atomic geometry of OH adsorption shown with side and top views of all unconstrained atoms for (a) Zn-terminated ZnO(0001) and b) O-terminated ZnO(000$\bar{1}$).

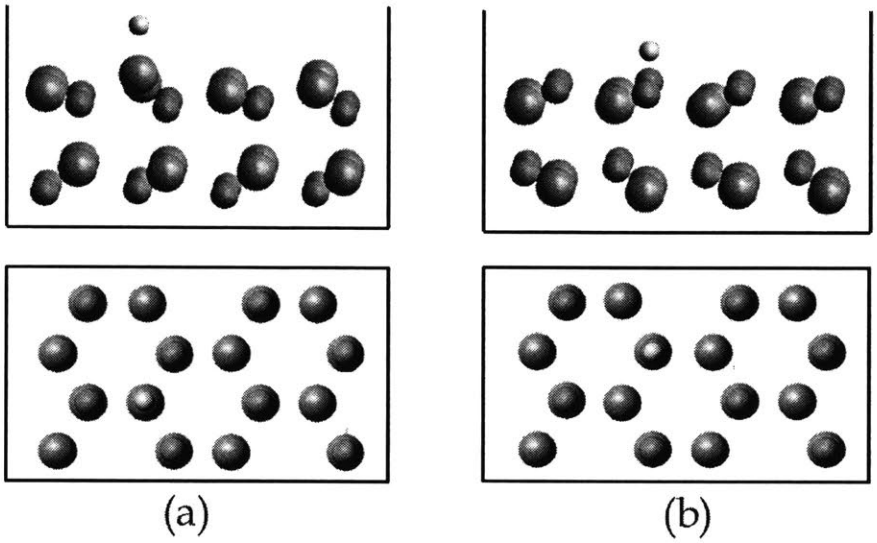


Figure A-7: Atomic geometry of H adsorption shown with side and top views of all unconstrained atoms for (a) Zn-terminated ZnO(0001) and b) O-terminated ZnO($000\bar{1}$).

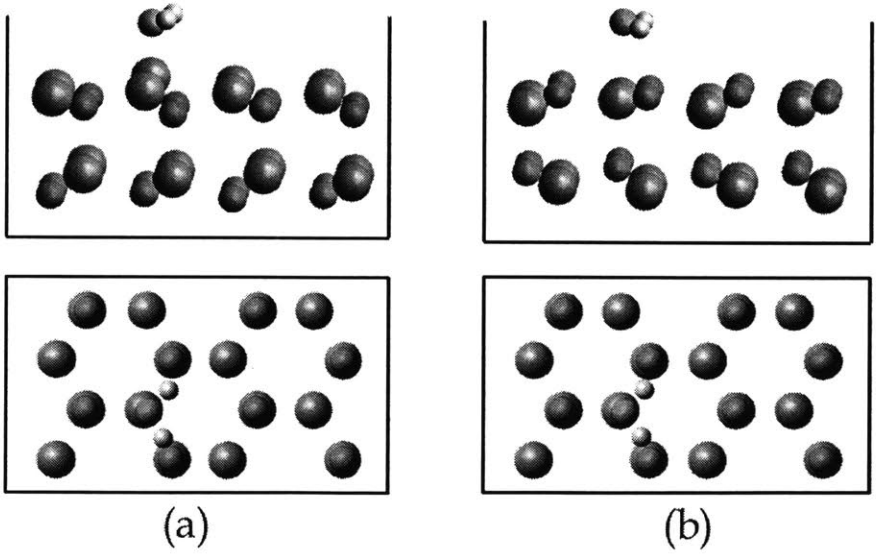


Figure A-8: Atomic geometry of $H_2O$ adsorption shown with side and top views of all unconstrained atoms for (a) Zn-terminated ZnO(0001) and b) O-terminated ZnO($000\bar{1}$).

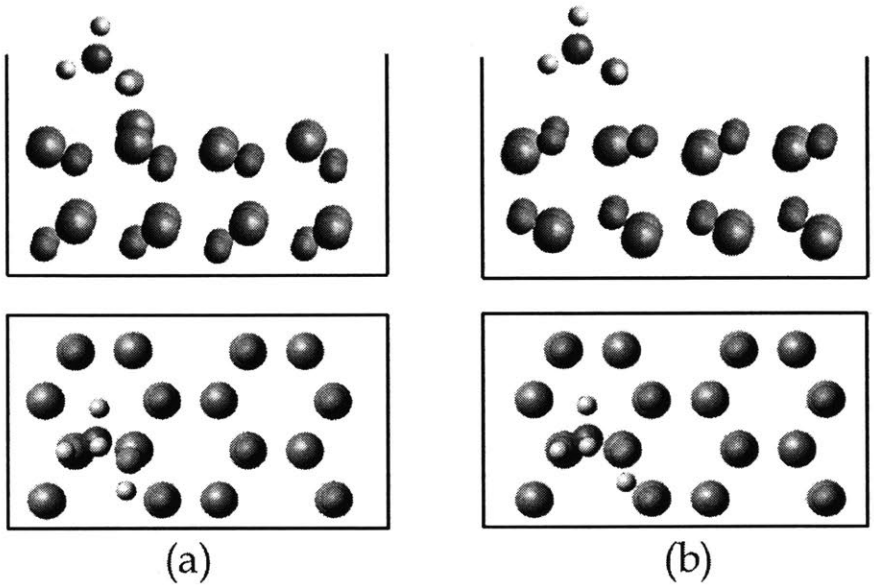


Figure A-9: Atomic geometry of $CH_3OH$ adsorption shown with side and top views of all unconstrained atoms for (a) Zn-terminated ZnO(0001) and b) O-terminated ZnO($000\bar{1}$).

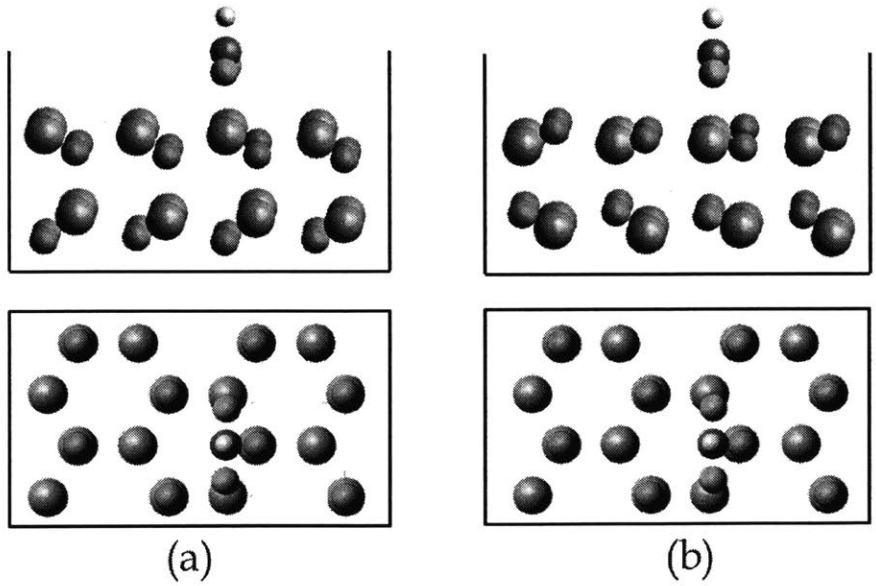


Figure A-10: Atomic geometry of HCOO adsorption shown with side and top views of all unconstrained atoms for (a) Zn-terminated ZnO(0001) and b) O-terminated ZnO($000\bar{1}$).

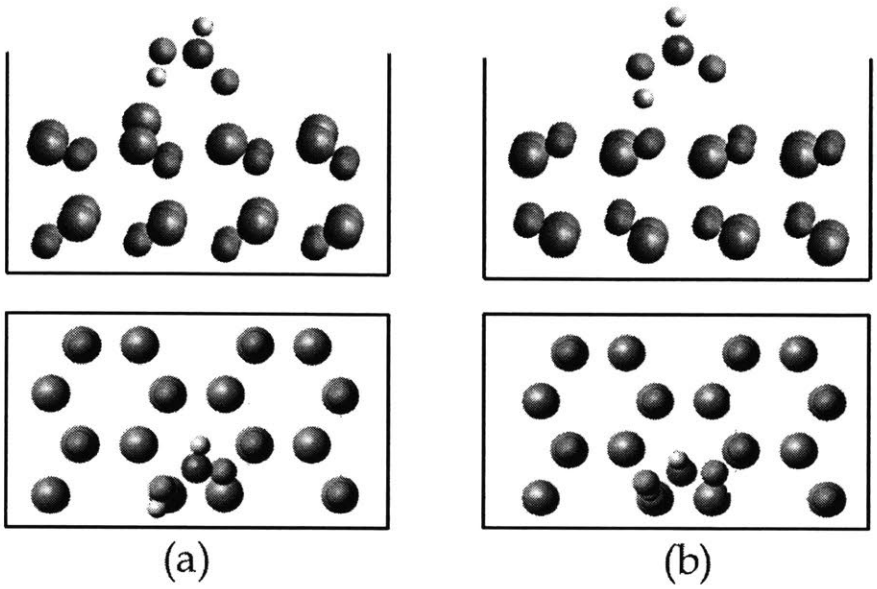


Figure A-11: Atomic geometry of HCOOH adsorption shown with side and top views of all unconstrained atoms for (a) Zn-terminated ZnO(0001) and b) O-terminated ZnO($000\bar{1}$).

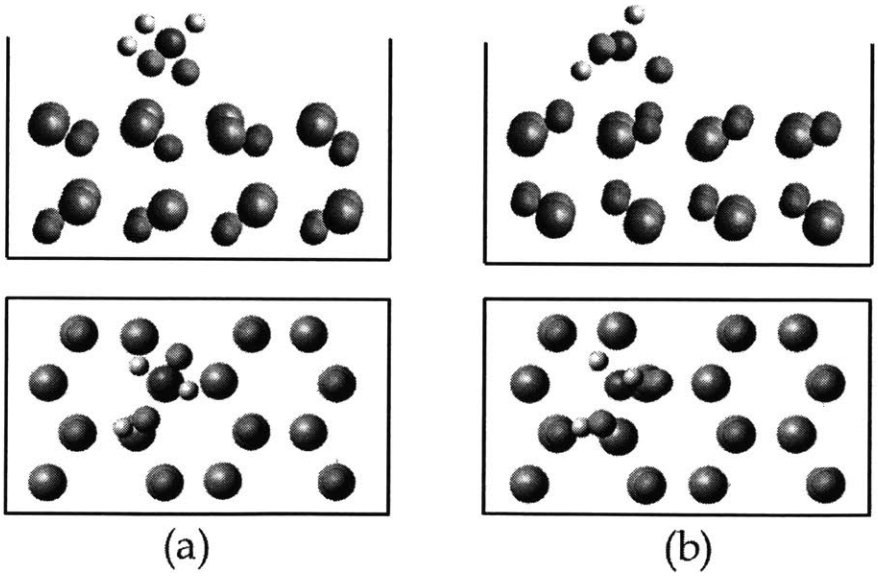


Figure A-12: Atomic geometry of $OCH_2OH$ adsorption shown with side and top views of all unconstrained atoms for (a) Zn-terminated ZnO(0001) and b) O-terminated ZnO($000\bar{1}$).

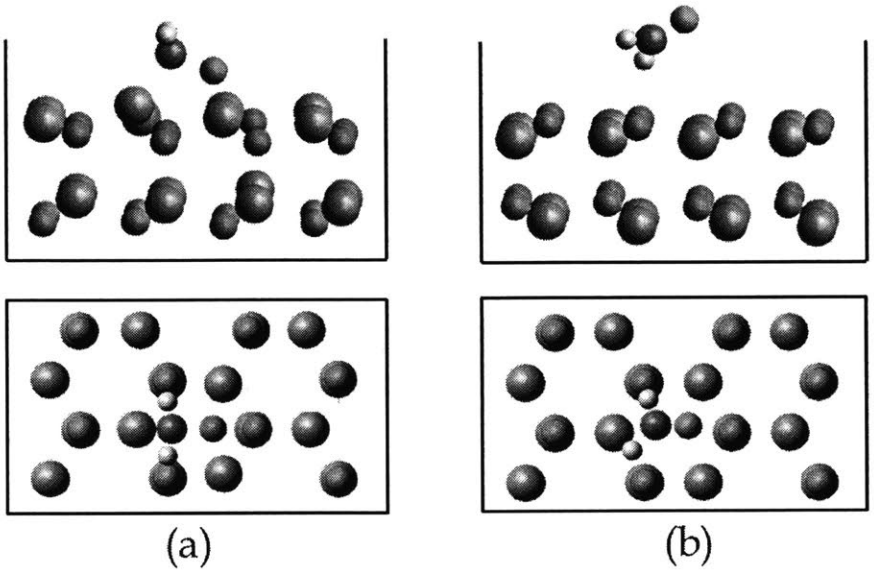


Figure A-13: Atomic geometry of $CH_2O$ adsorption shown with side and top views of all unconstrained atoms for (a) Zn-terminated ZnO(0001) and b) O-terminated ZnO($000\bar{1}$).

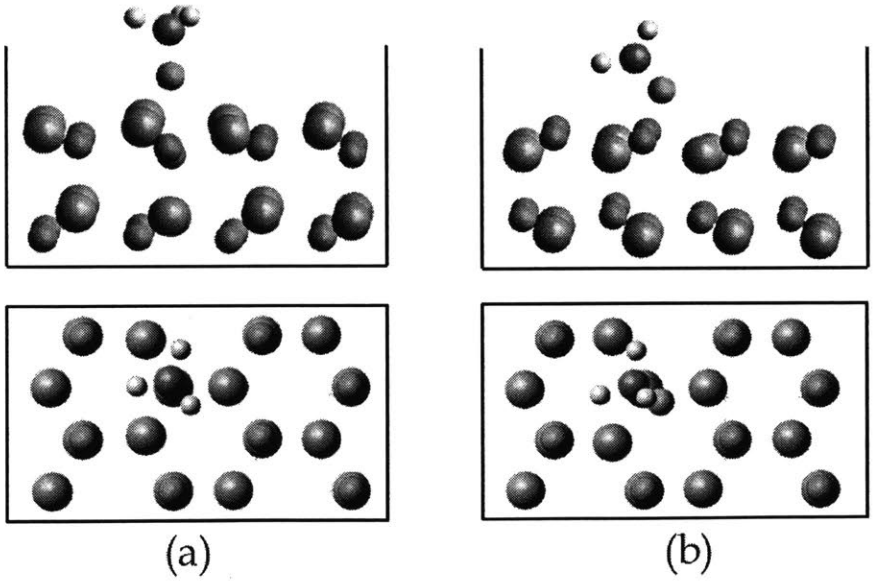


Figure A-14: Atomic geometry of $CH_3O$ adsorption shown with side and top views of all unconstrained atoms for (a) Zn-terminated ZnO(0001) and b) O-terminated ZnO($000\bar{1}$).

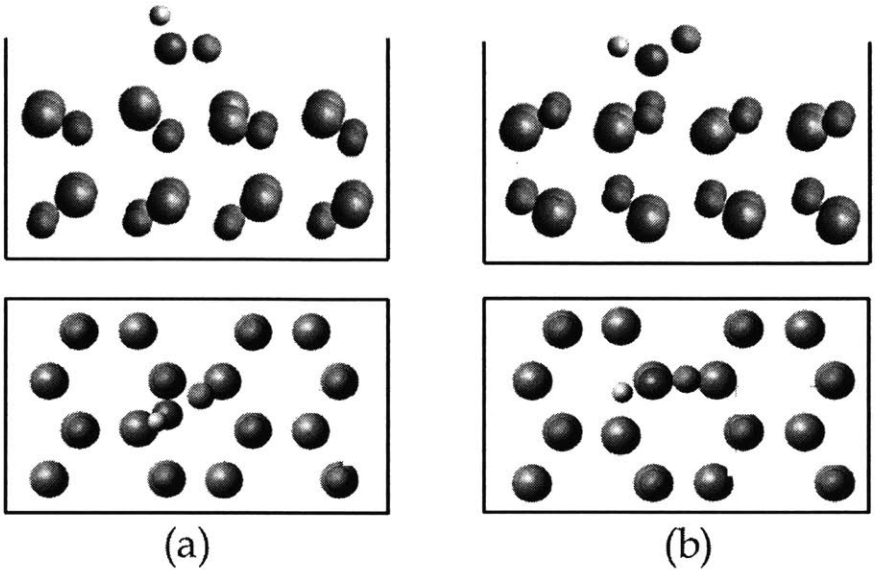


Figure A-15: Atomic geometry of HCO adsorption shown with side and top views of all unconstrained atoms for (a) Zn-terminated ZnO(0001) and b) O-terminated ZnO($000\bar{1}$).

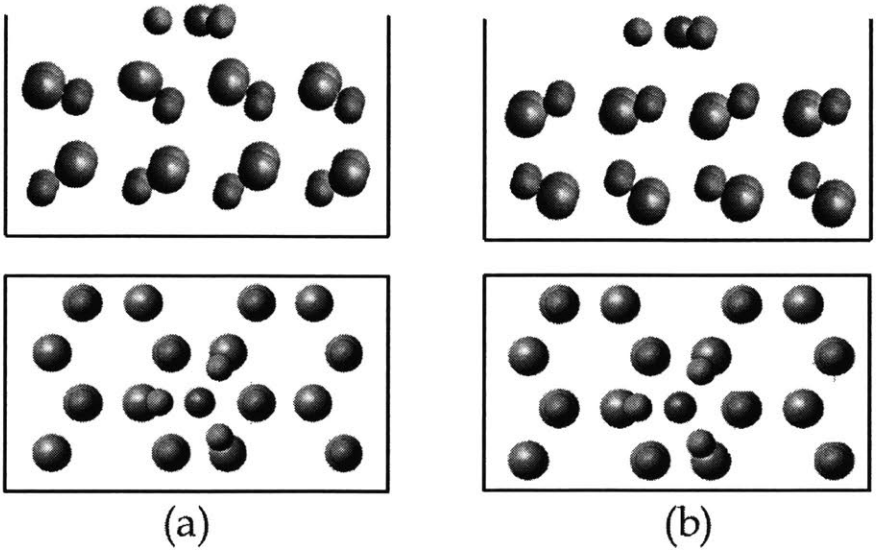


Figure A-16: Atomic geometry of $CO_3$ adsorption shown with side and top views of all unconstrained atoms for (a) Zn-terminated ZnO(0001) and b) O-terminated ZnO($000\bar{1}$).

# Appendix B

# DFT study of remote epitaxy through graphene layers

*Portions of this appendix were published in a co-authored paper [146].*

## B.1 Introduction

Epitaxial growth of materials has traditional been carried out on cleaved 3D structures, as the dangling bonds present anchors for the flux of atoms forming the epitaxial layer [147, 148]. The chemical bonds at the interface force each atom of the epitaxial layer are paired with a distinct atom of the substrate: the pairing of atoms is responsible for the crystalline ordering in an epitaxial growth, causing the epitaxial layer to mimic the crystalline symmetry and orientation of the substrate, especially in the case of homoepitaxy (growth of one material on another sample of the same material). However, this presents a limitation since the lattice of both the substrate and epitaxial layers must closely match for the anchoring to occur. Any deviation greater than 2-3% in lattice parameters usually result in strain of the epitaxial layer. When the lattice mismatch is relatively small, the first few atomic layers of the epitaxial layer can be coherently strained. The amount of the strain energy increases with the thickness of the epitaxial layer throughout the growth process. When the thickness of the thin film exceeds a certain critical value, it is energetically more favorable for

the system to nucleate defects, such as dislocations, vacancies and stacking faults, to relax the strain energy [149, 150]. These defects negatively impact the performance of semiconductors grown as heteroepitaxial systems.

Van der Waals (vdW) epitaxy [151] provides a way to circumvent the lattice match requirement. vdW epitaxy can be realized on materials having no dangling bonds on their clean surfaces, on which epitaxial growth proceeds by the van der Waals force. These materials are usually layered materials such as transition metal dichalcogenides ($TX_2$, T - transition metal, X - chalcogen, such as $MoS_2$ [152] and $MoTe_2$ [153]) and graphene. Being able to grow three-dimensional (3D) epitaxial films on 2D materials allow the transfer of single-crystalline semiconductor films since the epitaxial layer can be easily taken off the 2D substrate [154].

Van der Waals epitaxy also comes with its own disadvantages, however. The suppressed nucleation of the flux of atoms on the surface of the substrate limits the formation of a consistent single-crystalline layer of a sufficiently large area for practical applications [152, 153, 155, 156]. This means the 3D materials agglomerate on the surface of 2D materials rather than form consistent thin films [155, 156]. One way to solve this problem is to use interfacial buffers between the 3D epitaxial layer and the 2D substrate to promote nucleation of 3D materials [157, 158, 159]. However, the presence of the interfacial buffer layer does not bring the quality of the epitaxial film to that of one grown on a 3D material [160, 156].

Moreover, the presence of a buffer layer can be undesirable, for example in a case where device functionality relies on the contact between epitaxial layer and substrate, or when it is absolutely important to control the quality of the film. In 2014, J. Kim *et. al.* [5] demonstrated a process for the epitaxial growth of high-quality 3D GaN on graphene that overcome the challenges of the use of buffers and also produces higher quality films. The process is described in Fig. B-1. In addition to growing consistent films, their method could also be used for multiple growths and transfers of the GaN films on/from the original graphene/SiC substrate.

It has been assumed that the 2D materials are the only seed layers for van der Waals epitaxy [155, 161, 162] and no effort has so far been made to explore any

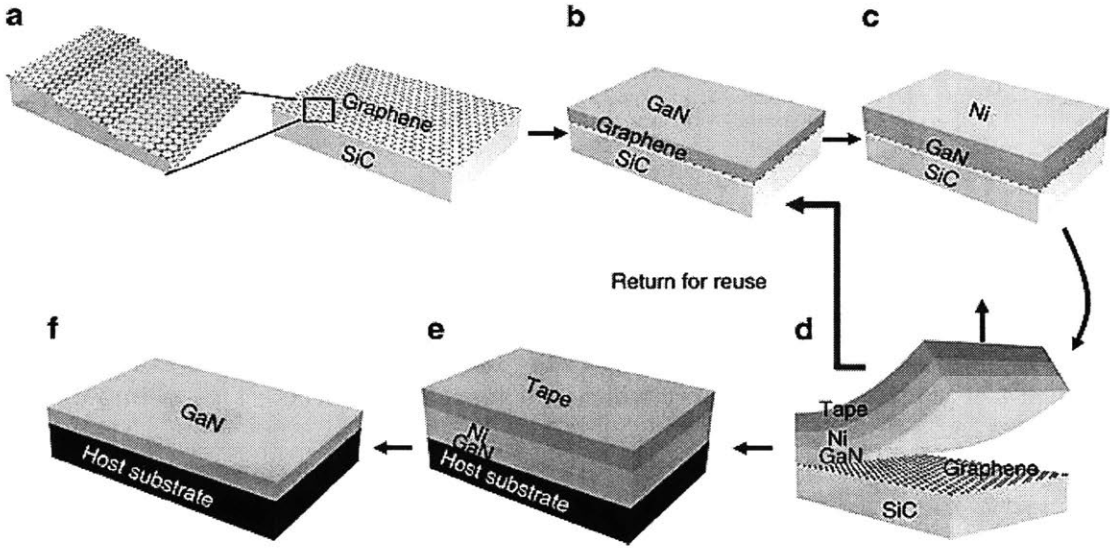


Figure B-1: Schematic of a method for growing/transferring single-crystalline thin films on/from epitaxial graphene. (a) Graphitization of a SiC substrate to form epitaxial graphene. (b) Epitaxial growth of GaN on graphene. (c) Deposition of a stressor layer (Ni). (d) Release of GaN from the substrate with a handling tape. (e) Transfer of the released GaN/Ni/tape stack on a host substrate. (f) Removal of the tape and Ni by thermal release and wet etching, leaving a GaN film on the host substrate. Reprinted with permission from Ref. [5].

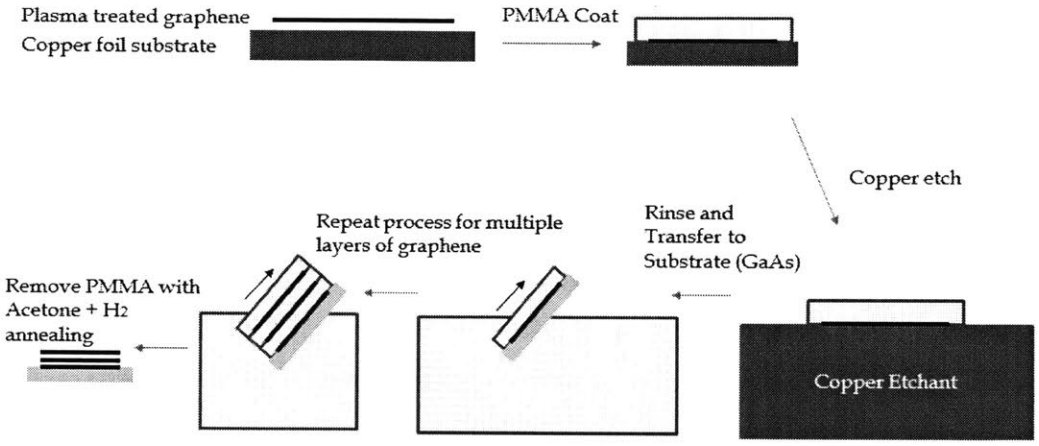


Figure B-2: Experimental method of multiple layer graphene transfer. This figure was produced by the Jeehwan Kim Group at MIT.

influence of the substrate support which can be a 3D material. This is important because the potential field applied from the underlying substrate support could be strong due the dangling bonds on its surface. Therefore, the substrates below 2D materials may still interact with the epitaxial layers grown during epitaxy, as in the case of the wetting transparency documented for graphene [163, 164]. In this work, we explore the influence of the substrate on van der Waals epitaxy and make predictions for certain materials. We will be exploring a semiconductor of commercial interest: GaAs.

## B.2 Methods

### B.2.1 Graphene formation and transfer

GaAs films were grown on CVD graphene or epitaxial graphene transferred on GaAs(001) wafers without precise alignment. CVD graphene was synthesized on a Cu foil using low pressure CVD. Cu foil was annealed in a quartz tube furnace at 1,000 °C for 30

min under 10 standard cubic centimetres per minute (sccm) of $H_2$ flow. Graphene growth proceeded under 4 sccm of $CH_4$ and 70 sccm of $H_2$ flow for 30 min at 1.90 torr. Graphene growth was terminated by a self-limiting process, yielding a monolayer of polycrystalline graphene. For the transfer process, poly(methyl-methacrylate) (PMMA) was spin-cast onto graphene coated Cu foil and baked at 80 °C for 10 min. Using the PMMA as a âĂŸhandleâĂŹ, the Cu foil was dissolved in $FeCl_3$ copper etchant solution for 15 min. While the grapheneâĂŞPMMA stack was held on the water surface by surface tension, the stack was transferred onto a GaAs substrate after its oxide was removed by 10% hydrochloric acid solution. The substrate was dried at 80 °C for 10 min and then the PMMA âĂŸhandleâĂŹ was dissolved in acetone. Annealing of transferred CVD graphene on GaAs substrates was performed at 350 °C for 30 min in ambient $H_2$ to remove the process residues at the interface and promote better adhesion. Epitaxial graphene was grown on a Si-face 4H-SiC(0001) wafer. Graphitization of SiC was performed at 1,575 °C for 1 h to form monolayer graphene in ambient Ar. The graphene was completely exfoliated using the LRGT process, in which a Ni stressor layer was deposited on epitaxial graphene and the grapheneâĂŞNi stack was removed from SiC using a thermally released tape handling layer. The grapheneâĂŞNi stack was immediately transferred to HCl-treated GaAs substrates followed by the removal of the thermal tape by annealing just above the release temperature of 90 °C. Then the Ni stressor layer was removed by dipping into acids.

### B.2.2 Epitaxial growth

Epitaxial growth of GaAs was performed on CVD graphene transferred onto GaAs(001) substrates in a close coupled showerhead MOCVD reactor. For GaAs growth, arsine and trimethylgallium were used as the precursors for As and Ga sources. The growth was divided into two parts. First, the growth proceeded at a relatively low temperature of 450 °C at 100 torr for a short time to encourage the nucleation of GaAs islands on graphene to initiate the growth. The reactor temperature was then ramped to 650 °C for normal growth of GaAs. For GaP and InP growth, phosphine, trimethylgal-

lium and trimethylindium were used as P, Ga and In sources, respectively, the growth conditions proceeded in the same manner as the GaAs growth in the MOCVD reactor. The LED device stack was regrown on a 4 $\mu$m thick n-GaAs buffer layer in the MOCVD reactor, with 800 nm of Si doped n-AlGaInP, 100 nm of GaInP, 800 nm of Zn doped p-AlGaInP and 100 nm of p-GaAs as a capping layer. The device was grown at 650 °C under $N_2$ flow as ambient carrier gas.

### B.2.3 Computational model

As-termination of GaAs(001) slabs was selected for computational modelling as the growth conditions of the epitaxial layer imply an As pre-layer terminating the ends of the slabs. DFT computations were performed to determine the interaction of As- and Ga-terminated layers of GaAs(001) on the As-terminated substrate. The computations were done using the plane-wave pseudopotential code Quantum Espresso [94]. We found the convergence of the number of layers of GaAs(001) slab to be 12. In all our calculations, all atoms (Ga, As) were relaxed. A k-point mesh of $4 \times 4 \times 1$ was selected. For the local exchange correlation functional, the PerdewâĂŞBurkeâĂŞErnzerhof general gradient approximation was used [165]. The spacing between periodic images of the superstructure in the z direction was varied between 5 Åand 30 Å. The in-plane lattice constant was fixed to $1 \times 1$ times the calculated lattice constant (5.63 Å) of bulk GaAs. An ideal case of a $1 \times 1$ system was modelled for the simulation as surface reconstructions do not significantly affect the behaviour of the surface at the interface [166, 167]. The relaxation calculations were set to complete when the forces on the relaxed layers were less than $1 \times 10^{-3}$ a.u. We employed wavefunction and charge density kinetic energy cut-offs of 50 Ry and 350 Ry, respectively.

### B.2.4 Exfoliation of GaAs from graphene surface

Deposition of a 100 nm Ti adhesion layer and a high stress Ni stressor layer on the GaAs epilayer surface induces strain at the GaAsâĂŞgraphene interface. By applying the thermal-release handling tape, fast release of the GaAs epilayer occurs from the

graphene surface.

### B.2.5 Light-emitting diodes

After remote epitaxy, the front contact is patterned by photolithography using an LOR 3A and SPR 220 bilayer photoresist process. Then, a Pd(5 nm)/Ge(20 nm)/Au(100 nm) metal contact is deposited by e-beam evaporation. The 100 $\mu$m diameter contact pad is patterned at the centre of the device. After the metal layer is lifted off, 200 $\mu$m $\times$ 200 $\mu$m mesas are defined by photolithography using SPR 220 and chemical etching using HCl:$H_3PO_4$ (3:1) solution. The LEDs are annealed for 1 h at 200 °C for ohmic contact formation. For 2DLT processed LEDs, 50 nm of titanium is deposited by thermal evaporation on the as-grown sample then nickel was sputter deposited to a thickness of 6 Îijm with argon plasma. Thermal release tape is applied to the metal stressor/as-grown sample heterostructure, followed by pulling the thermal release tape from the substrate edge to obtain exfoliation from the graphene interface. For thin films transferred to silicon, polydimethylsiloxane (PDMS) was spin-coated onto a Si(001) wafer at 2,000 r.p.m. for 30 s, followed by baking in an oven at 80 °C for 2 min. The exfoliated film is then placed on the PDMS and pressure is applied. The thermal tape holding the film is then removed by heating the entire structure on a hot plate at 125 °C until the tape is thermally released. The bonded stack is left to cool at room temperature for 30 min. Nickel and titanium are removed by FeCl3 solution (20% w/v) and dilute HF. After the film transfer, the same fabrication method is applied for the substrate-based LED described above. The LEDs are tested under continuous-wave (CW) conditions.

## B.3 Results

To experimentally verify if remote homoepitaxy of GaAs through a graphene interlayer is possible, we prepared epitaxial templates by transferring monolayer, bilayer and tetralayer graphene onto GaAs(001) substrates. Native oxide on the GaAs substrates was etched away in HCl solution prior to immediate graphene transfer to

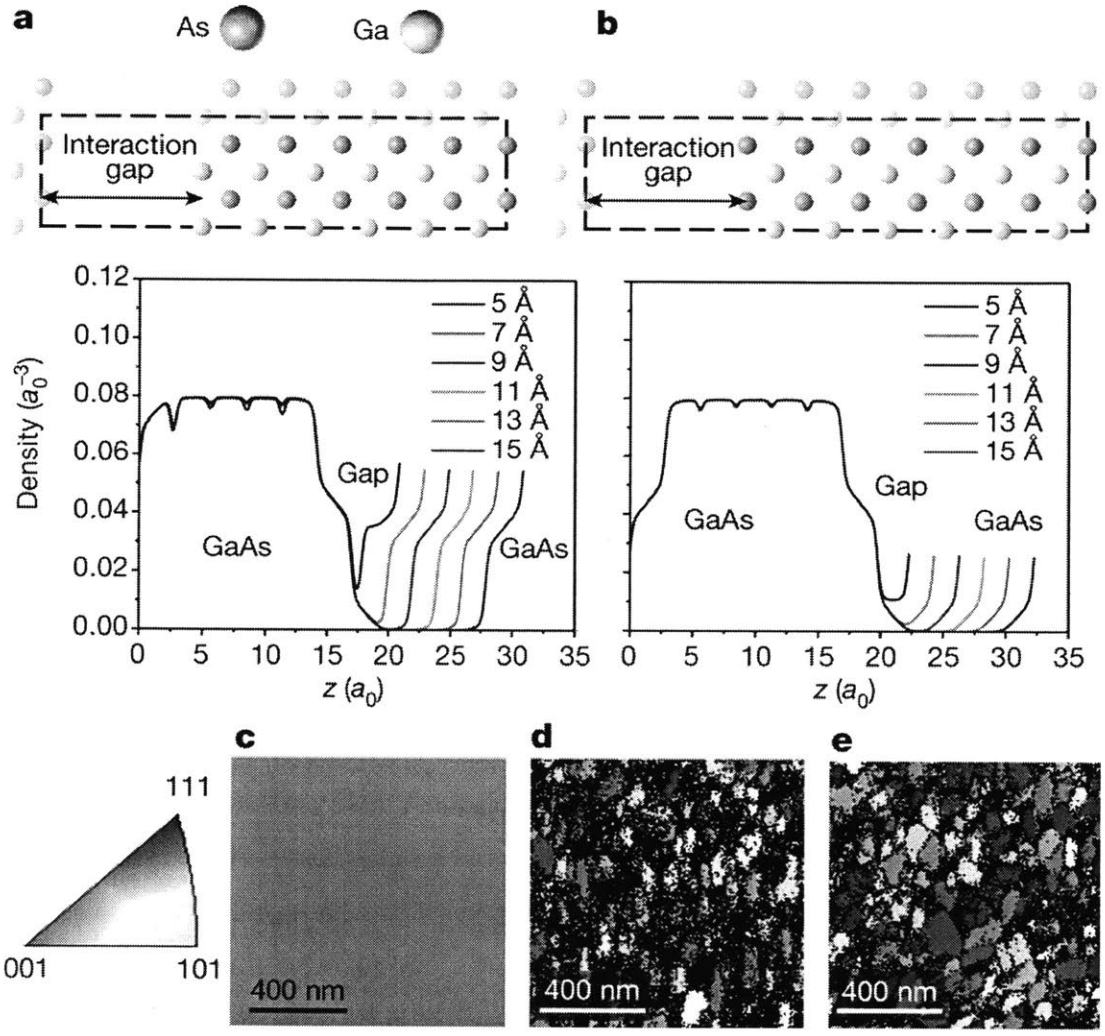


Figure B-3: (a), (b), Main plots, results of DFT calculations of averaged electron density along separated slabs of GaAs for AsâĂŞGa interaction (a) and AsâĂŞAs interaction (b). Periodic boundary conditions were imposed along the dashed lines of the simulation model (shown at top). Both plots show the existence of significant electron charge density between the separated slabs within a gap of about 9 Å. (c)âĂŞ(e), EBSD maps of GaAs grown on and exfoliated from âĂŸmonolayerâĂŹ grapheneâĂŞGaAs(001) substrate (c), showing (001) single-crystallinity, and of GaAs grown on and exfoliated from âĂŸbilayerâĂŹ (d) and âĂŸtetralayerâĂŹ (e) grapheneâĂŞGaAs(001) substrate showing (111)-dominant polycrystallinity. On the left is the inverse pole figure colour triangle for crystallographic orientations.

ensure a pristine interface between graphene and GaAs. Next, epitaxial growth of GaAs films on the various graphene stacks on GaAs(001) substrates was performed (see Fig. B-4 for the topology of GaAs epilayer surfaces). To characterize the crystallographic orientation of the GaAs epilayer independently from that of the GaAs substrate, the GaAs epilayer was exfoliated from the grapheneâĂŞGaAs substrate using a metal stressor8. Because the graphene interlayer completely separates the GaAs film from the GaAs substrate and allows precise release of GaAs films from the weakly attached graphene surface, the surface of the released side of GaAs presents a smooth finish after exfoliation (see see Fig. B-4). This flat morphology enabled the use of electron backscatter diffraction (EBSD) mapping to identify domains of unique crystalline orientations in the GaAs epilayer. We found that the exfoliated GaAs epilayer grown on âĂŸmonolayerâĂŹ grapheneâĂŞGaAs(001) substrate exhibits (001) orientation, as indicated in red by the inverse pole figure (IPF) colour triangle (see Fig. B-3(c)). This (001) orientation imprinted by the substrate disappears when GaAs films are grown on bilayer or tetralayer graphene (see Fig. B-3(d), (e)). X-ray diffraction using ÏĽâĂŞ2Îÿ scans of exfoliated GaAs epilayers also indicates that (001) single-crystallinity, present in GaAs grown on monolayer graphene, disappears for GaAs grown on bilayer and tetralayer graphene (see Fig. B-5). These observations indicate that remote epitaxy through the gap created by monolayer graphene is possible. Moreover, the large-scale view of an EBSD map of the exfoliated side of a GaAs film grown on grapheneâĂŞGaAs(001) substrate in Fig. B-6(a) shows (001) single-crystallinity. A high-resolution X-ray diffraction ÏŢ scan of the same exfoliated GaAs films (see Fig. B-6b) shows four-fold symmetry of the diffraction peaks corresponding to GaAs(224) with 90Âř intervals, indicating that the GaAs grown on the GaAs(001) substrate through monolayer graphene is a single-crystalline zinc-blende phase without azimuthal rotations. Taken together, these observations confirm that the single-crystalline substrate is capable of transferring its epitaxial registry through a single graphene layer remotely to the epilayer, in good agreement with our critical gap calculation.

We note that merely placing monolayer graphene on the substrate does not guar-

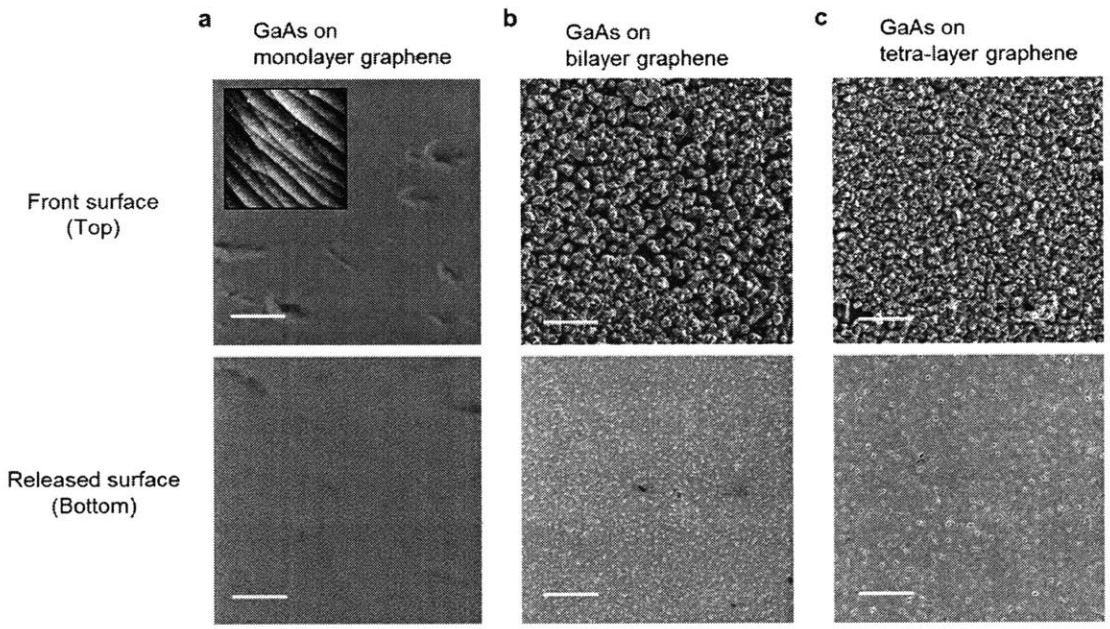


Figure B-4: (a) The front surface of the GaAs epilayer grown on monolayer grapheneâĂŞGaAs substrate is generally smooth but also contains impinging marks which need to be addressed by further optimization of nucleation and growth. Inset, 1 Îijm ĂŰ 1 Îijm non-contact AFM scan; the epitaxial layer appears to be growing via step flow growth. The r.m.s. roughness of the AFM scan is 0.3 nm. (b), (c), Three-dimensional growth was observed for films grown on thicker grapheneâĂŞsubstrates owing to limited registry from the substrates. Scale bars, 4 Îijm. Top and bottom panels of aâĂŞc indicate front and released surfaces, respectively.

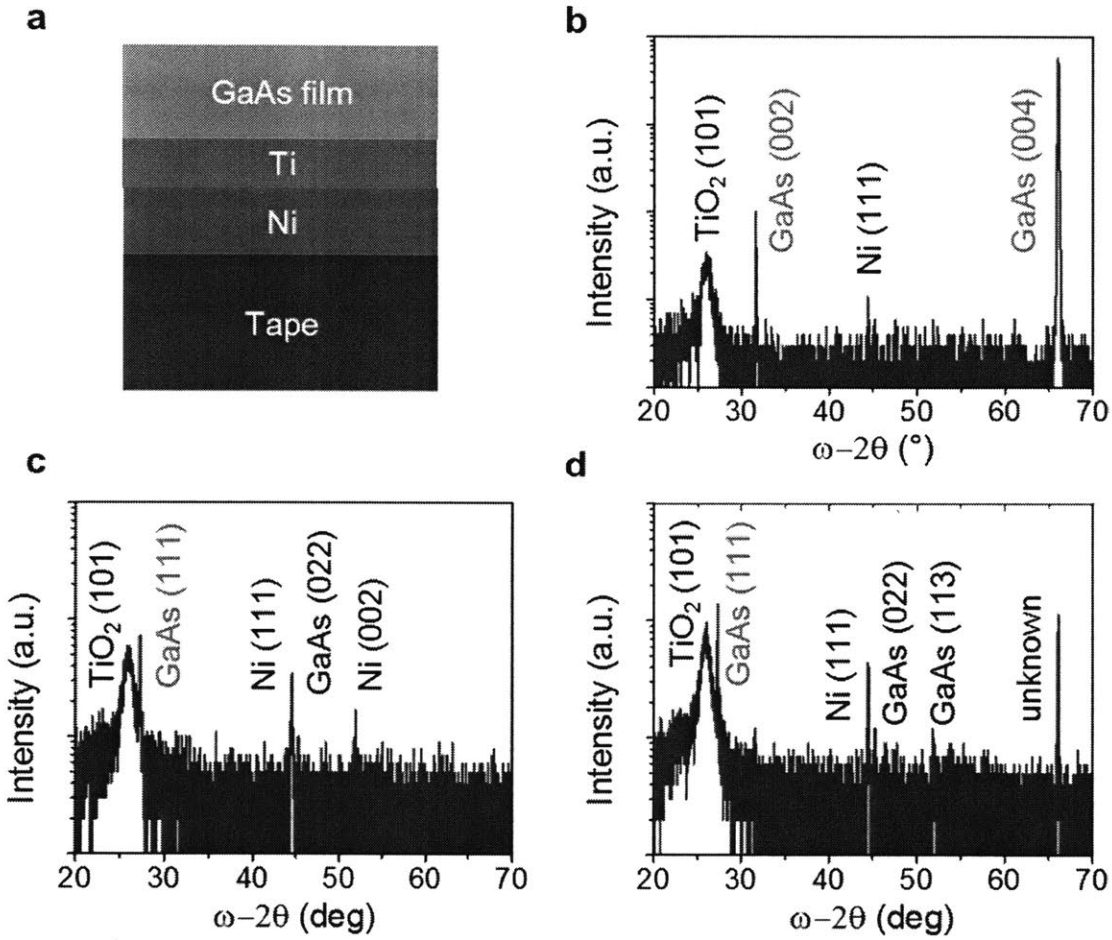


Figure B-5: (a) Diagram of exfoliated stacks of GaAs released from a grapheneâĂŞ-GaAs(001) substrate. (b) ÏĽâĂŞ2Îÿ scan of GaAs exfoliated from monolayer graphene transferred on a GaAs(001) substrate showing (001) single-crystallinity as indicated by XRD peaks of the (002) and (004) lattice labelled in red. (c) ÏĽâĂŞ2Îÿ scan of GaAs exfoliated from bilayer graphene transferred on GaAs(100) substrate showing polycrystallinity with dominant (111) orientation, as indicated by the XRD peak of the (111) lattice labelled in red, and d, ÏĽâĂŞ2Îÿ scan of GaAs exfoliated from tetralayer graphene transferred on a GaAs(001) substrate showing polycrystallinity with dominant (111) orientation, also indicated by XRD peak of the (111) lattice labelled in red. The ÏĽâĂŞ2Îÿ scans also picked up XRD peaks from the Ni stressor film and the Ti adhesion layer that was used to exfoliate the GaAs films (Methods). The presence of these films are shown by the XRD peak of the (111) Ni lattice and the (101) lattice of anatase TiO2 from the Ti layer.

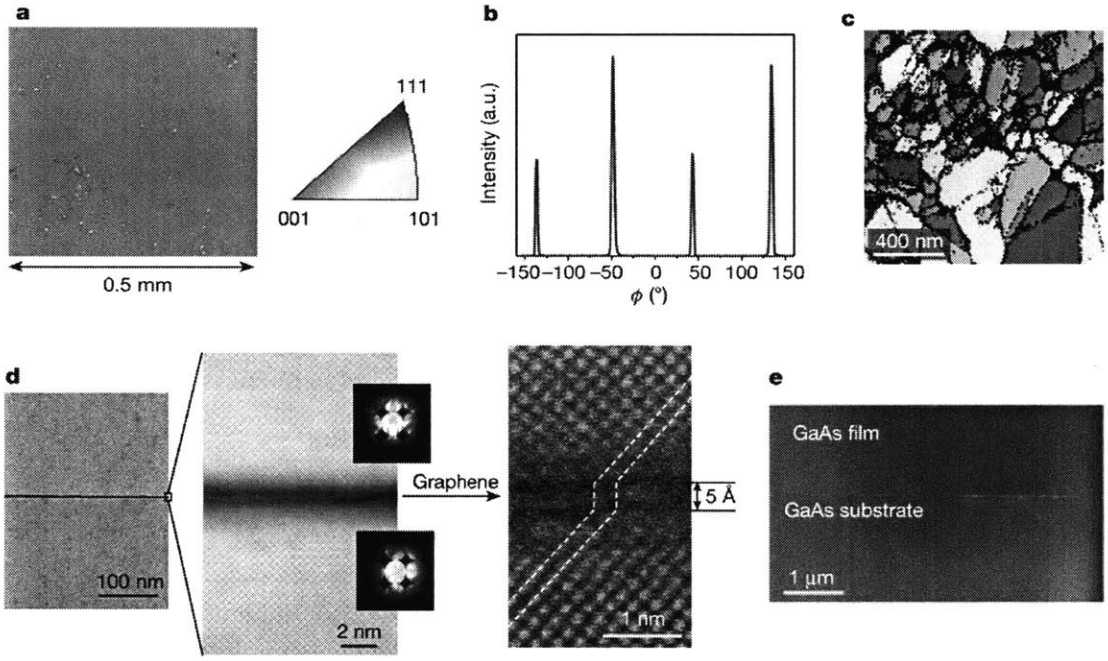


Figure B-6: Characterization of GaAs grown on the monolayer grapheneâĂŞGaAs(001) substrate. (a) Large-scale EBSD map of exfoliated GaAs. (b) High-resolution X-ray diffraction azimuthal off-axis ÏŢ scan of the same exfoliated GaAs layer, representing a single-crystalline zinc-blende structure without in-plane rotations. (c) EBSD map of an exfoliated GaAs layer grown on a monolayer grapheneâĂŞGaAs substrate without $H_2$ annealing after transfer. (d) High-resolution STEM images showing excellent remote alignment of the GaAs(001) lattices through the graphene. Convergent-beam electron diffraction patterns from the epilayer (top inset) and the substrate (bottom inset) show identical zinc-blende (001) orientations. (e) Low-angle annular dark field STEM image showing no dislocations.

antee perfect registry of the epilayer to the substrate. During the wet transfer of graphene grown on Cu foils via chemical vapour deposition, process-induced adsorbates can reside at the graphene surface and at transfer interfaces [168, 169] and need to be removed via annealing [170, 171] to enhance the proximity of graphene to the substrate. As shown in the EBSD map of GaAs grown on âĂŸun-annealedâĂŹ monolayer graphene transferred on a GaAs substrate, the resulting GaAs films are not epitaxial to the substrate (see Fig. B-6(c)). To ensure a clean interface in the graphene transfer, we use a layer-resolved graphene transfer (LRGT) process whereby a metal stressor is used to exfoliate monolayer epitaxial graphene from a SiC substrate immediately followed by dry-transfer onto the GaAs substrate. The LRGT process ensures single-crystalline growth via remote epitaxy without the need for annealing. We find that regardless of the type of graphene and its alignment to the substrate, GaAs epilayers are registered to the GaAs substrate through monolayer graphene.

The remote epitaxial alignment between a GaAs(001) epilayer and a GaAs(001) substrate was atomically resolved by performing cross-sectional scanning transmission electron microscopy (STEM). Figure 2d shows STEM images at different magnifications which reveal that the GaAs(001) epilayer is epitaxially aligned with the GaAs(001) substrate through the gap created by monolayer graphene. The measured gap between the GaAs epilayer and the substrate is about 5 ÃĚ, which is below the critical gap calculated with DFT. In Fig. B-6(d), the monolayer graphene is visible between the epitaxial layer and the substrate (indicated by the arrow). Identical convergent beam electron diffraction patterns from the epilayer and the substrate also confirm the epitaxial relationship. We also investigated the dislocation density using low-angle annular dark field imaging of the GaAsâĂŞgrapheneâĂŞGaAs sample at low magnification in cross-sectional STEM (see Fig. B-6(e)); we found no evidence for strain contrast at the substrateâĂŞepilayer interfaceâĂŤwhich typically appears when dislocations are presentâĂŤin these images. This implies that no dislocations are present, at least not in the inspected area. Moreover, no anti-phase domains appeared to have nucleated at the graphene interface. Although the TEM inspection covered only a limited sample area, corresponding to the conventional size of TEM

samples prepared by a focused ion beam, it does confirm that remote homoepitaxial growth of GaAs through flat graphene on GaAs substrates does occur.

Steady-state room-temperature photoluminescence spectra of exfoliated GaAs, grown on grapheneâĂŞGaAs substrates, are comparable to spectra recorded for GaAs wafers, indicating no degradation in material quality during growth/transfer processes. This motivated us to grow AlGaInPâĂŞGaInP double heterojunction light-emitting diodes (LEDs) on grapheneâĂŞGaAs substrates (see Fig. B-7(a) for cross-sectional scanning electron microscopy of heterojunction LEDs). Such devices exhibited IâĂŞV curves and turn-on voltages of 1.3 V that are comparable to those of LEDs directly grown on a bare GaAs substrate (Fig. B-7(b), with the inset illustrating red light emission from LEDs grown through remote epitaxy). Electroluminescence spectra of the LEDs grown on GaAs, either through remote epitaxy with graphene or conventionally without graphene, confirmed their nearly identical performance, with very similar full-width at half-maxima of 45 Âś 5 nm and peak electroluminescence intensities at an injection current of 250 mA (see Fig. B-7(c)). The insets of Fig. 3c show photographs of functioning LEDs grown on GaAs with and without graphene. The LEDs were exfoliated and transferred to the Si substrate, which minimally degrades the LED performance as indicated by the comparable IâĂŞV curves and light emission before and after the transfer.

To investigate if remote homoepitaxy can be applied to other general material systems, we have performed epitaxial growth of InP and GaP on InP(001) and GaP(001) substrates, respectively, with an overlayer of monolayer graphene. As shown in Fig. B-8, single-crystalline GaAs(001), InP(001) and GaP(001) films were successfully grown via remote homoepitaxy and exfoliated. Characterizations based on high-resolution X-ray diffraction and EBSD measurements (shown in Fig. 4dâĂŞf and gâĂŞi, respectively) confirm the single-crystal nature of GaAs, InP and GaP films grown by remote epitaxy that support the feasibility of our 2D material-based layer transfer (2DLT) technique for general material systems. In addition, the crystalline orientation can be manipulated by changing the orientation of the substrate. Single-crystalline GaAs(111) films have been grown on monolayer grapheneâĂŞGaAs(111)B. Graphene

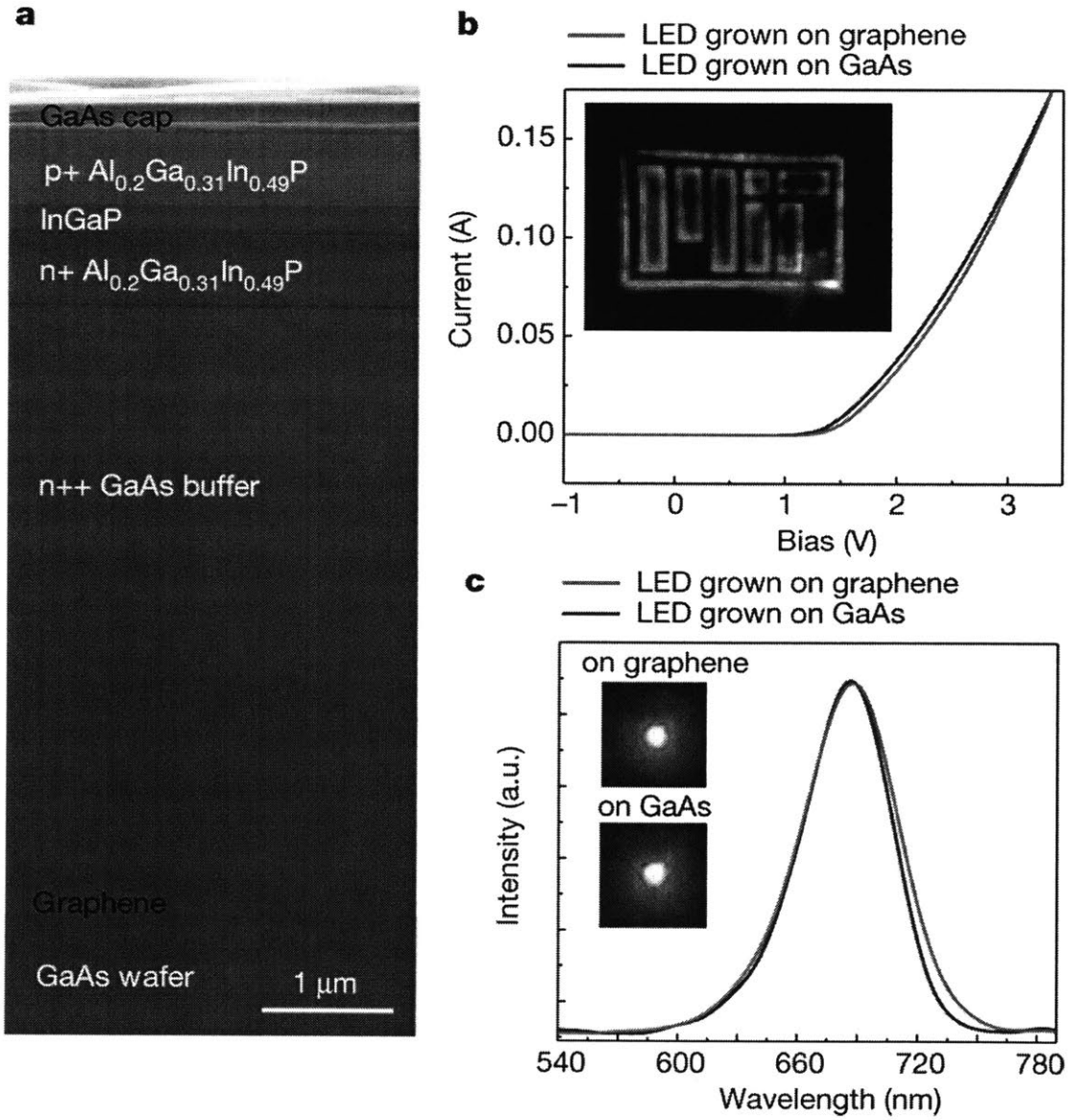


Figure B-7: AlGaInPâĂŞGaInP double heterojunction LEDs on a grapheneâĂŞGaAs substrate. AlGaInPâĂŞGaInP double heterojunction LEDs on a grapheneâĂŞGaAs substrate. a, Cross-sectional SEM image of heterojunction LEDs. b, IâĂŞV curves of LEDs grown on grapheneâĂŞGaAs substrates and directly on GaAs. Inset, emitted red light from the LEDs grown on the grapheneâĂŞGaAs substrate. c, Electroluminescence spectra of the LEDs grown on grapheneâĂŞGaAs substrates and directly on GaAs, Inset, photographs of functioning LEDs grown on both substrates.

is known to remain pristine during epitaxy without dissolving into substrates or epilayers owing to its high thermal stability thus all epitaxial materials investigated in this study were successfully exfoliated by a Ti/Ni stressor as shown in Fig. B-8(a)âĂŞ(c). Epilayers failed to exfoliate when epitaxy was performed on a substrate with a graphene overlayer that had been pre-damaged by Ar plasma treatment. The smooth morphology of the exfoliated epilayer surface suggests precise release from pristine graphene. Note that rough spalling marks observed in very limited areas originated from direct epitaxy through localized defects/holes in the graphene which remains to be addressed by improving the yield of graphene transfer. The ease of applying this 2DLT technique to a multitude of systems will allow less common semiconductors such as InP to see common use in various applications.

## B.4 Conclusion

Our results indicate that remote homoepitaxy is possible due to the interaction between substrate and epilayer through monolayer graphene, which is sufficiently thin and electrically penetrable to guide the epitaxial orientation of overlayers. Since the epilayers grown by remote homoepitaxy can be released from the graphene surface, this 2DLT technique offers the potential to grow, transfer and stack any electronic and photonic materials on 2D materials without the lattice matching limitation. This will open a pathway towards defect-free heterointegration of dissimilar materials while saving the cost of expensive and exotic substrates.

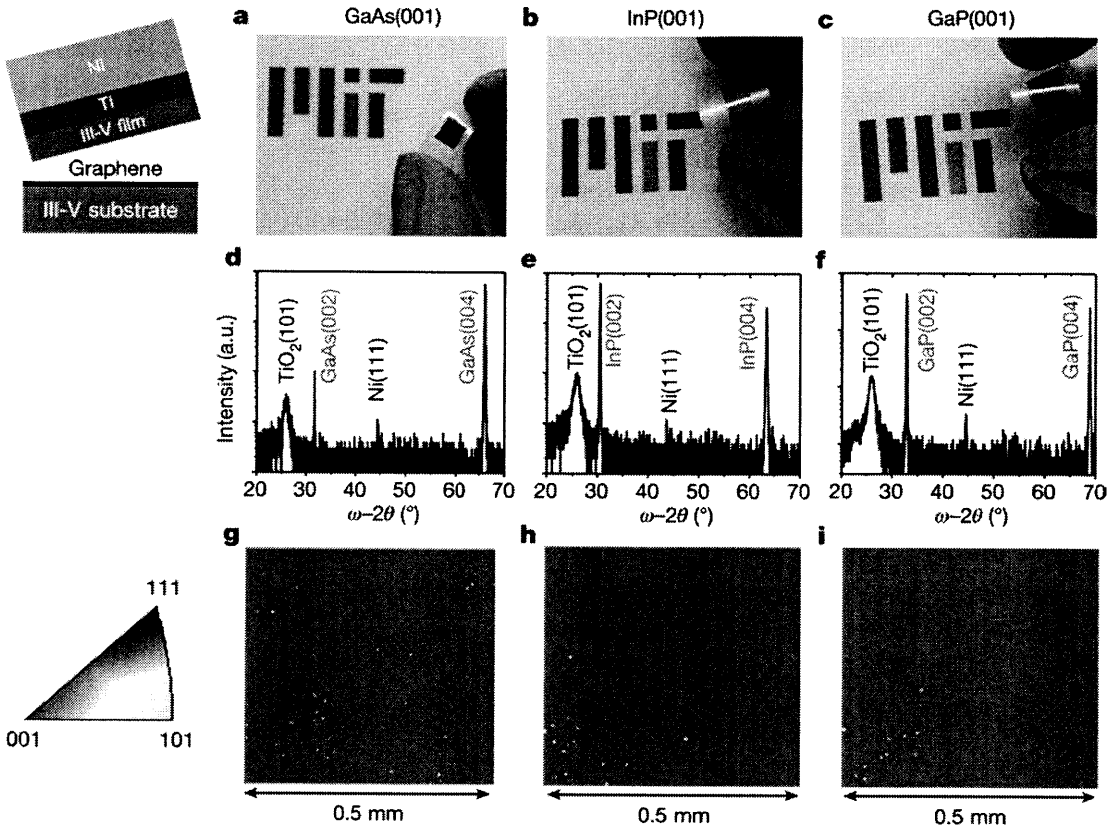


Figure B-8: Single-crystalline III-V(001) films exfoliated from grapheneâĂŞIII-V(001) substrates after remote epitaxy. Single-crystalline III-V(001) films exfoliated from grapheneâĂŞIII-V(001) substrates after remote epitaxy. a, d, g, GaAs; b, e, h, InP; c, f, i, GaP. Schematic illustration (top left) shows the exfoliation process of thin-film sample preparation for high-resolution X-ray diffraction and EBSD characterizations. aâĂŞc, Photographs of single-crystalline GaAs(001), InP(001), and GaP(001) films exfoliated from grapheneâĂŞIII-V(001) substrates. dâĂŞf, High-resolution X-ray diffraction ĬL'âĂŞ2Îÿ scans of the exfoliated semiconductor/stressor stack that includes GaAs(001), InP(001), and GaP(001) epilayers. gâĂŞi, Large-scale EBSD maps of GaAs(001), InP(001), and GaP(001) epilayer surfaces.

# Bibliography


[1] Mette Mikkelsen, Mikkel Jørgensen, and Frederik C. Krebs. The teraton challenge. a review of fixation and transformation of carbon dioxide. *Energy & Environmental Science*, 3(1):43, 2010.

[2] Hyungwoo Lee, Tae Heon Kim, Jacob J Patzner, Haidong Lu, Jung-Woo Lee, Hua Zhou, Wansoo Chang, Mahesh K Mahanthappa, Evgeny Y Tsymbal, Alexei Gruverman, et al. Imprint control of batio3 thin films via chemically induced surface polarization pinning. *Nano letters*, 16(4):2400–2406, 2016.

[3] Alexie M Kolpak, Ilya Grinberg, and Andrew M Rappe. Polarization effects on the surface chemistry of PbTiO3-supported pt films. *Physical review letters*, 98(16):166101, 2007.

[4] X. H. Wei, Y. R. Li, W. J. Jie, J. L. Tang, H. Z. Zeng, W. Huang, Y. Zhang, and J. Zhu. Heteroepitaxial growth of ZnO on perovskite surfaces. *Journal of Physics D: Applied Physics*, 40(23):7502, 2007.

[5] Jeehwan Kim, Can Bayram, Hongsik Park, Cheng-Wei Cheng, Christos Dimitrakopoulos, John A Ott, Kathleen B Reuter, Stephen W Bedell, and Devendra K Sadana. Principle of direct van der waals epitaxy of single-crystalline films on epitaxial graphene. *Nature communications*, 5, 2014.

[6] Babatunde Alawode. A first principles computational study of zno/$PbTiO_3$ as a tunable catalyst for $CO_2$ conversion. Master's thesis, Massachusetts Institute of Technology, Cambridge, MA, USA, 2015.

[7] Greenhouse gases, climate change, and energy.

[8] Appendix a: CO2 for use in enhanced oil recovery (EOR) | global carbon capture and storage institute.

[9] The Global CCS Institute. Accelerating uptake of CCS: industrial use of captured carbon dioxide. Technical report, March 2011.

[10] Carbon capture and storage: Special report of the intergovernmental panel on climate change. Technical report, IPCC, 2005.

[11] P. Viebahn and M. Fischedick. Carbon capture and storage in Germany–Cost development, life cycle assessment, and energy scenarios within an integrated assessment.

[12] M. Lenzen. Global warming effect of leakage from CO2 storage. *Critical Reviews in Environmental Science and Technology*, 2010.

[13] False hope: Why arbon capture and storage won't save the climate. Technical report, Greenpeace, May 2008.

[14] Walter Leitner. Supercritical carbon dioxide as a green reaction medium for catalysis. *Accounts of Chemical Research*, 35(9):746–756, September 2002.

[15] Clarence D Chang. Methanol to gasoline process. In *Perspectives in Molecular Sieve Science*, volume 368, pages 596–614. American Chemical Society, 1988.

[16] The Methanol Institute. The methanol industry report 2015.

[17] J. F. Knifton and R. G. Duranleau. Ethylene glycol—dimethyl carbonate co-generation. *Journal of molecular Catalysis*, 67(3):389–399, 1991.

[18] S. Liang, H. Liu, T. Jiang, J. Song, G. Yang, and B. Han. Highly efficient synthesis of cyclic carbonates from CO2 and epoxides over cellulose/KI. *Chem. Commun.*, 47(7):2131–2133, 2010.

[19] K. Xu. Nonaqueous liquid electrolytes for lithium-based rechargeable batteries. *Chemical Reviews-Columbus*, 104(10):4303–4418, 2004.

[20] Michael North. Synthesis of cyclic carbonates from CO2 emissions. *Chemistry Today*, 30(3), June 2012.

[21] Felix Studt, Irek Sharafutdinov, Frank Abild-Pedersen, Christian F Elkjær, Jens S Hummelshøj, Søren Dahl, Ib Chorkendorff, and Jens K Nørskov. Discovery of a Ni-Ga catalyst for carbon dioxide reduction to methanol. *Nature Chemistry*, 6(4):320–324, 2014.

[22] Anders B Laursen, Ana Sofia Varela, Fabio Dionigi, Hank Fanchiu, Chandler Miller, Ole L Trinhammer, Jan Rossmeisl, and Søren Dahl. Electrochemical hydrogen evolution: SabatierâĂŹs principle and the volcano plot. *Journal of Chemical Education*, 89(12):1595–1599, 2012.

[23] Jeff Greeley, Thomas F Jaramillo, Jacob Bonde, IB Chorkendorff, and Jens K Nørskov. Computational high-throughput screening of electrocatalytic materials for hydrogen evolution. *Nature materials*, 5(11):909–913, 2006.

[24] Malte Behrens, Felix Studt, Igor Kasatkin, Stefanie Kuhl, Michael Havecker, Frank Abild-Pedersen, Stefan Zander, Frank Girgsdies, Patrick Kurr, Benjamin-Louis Kniep, Michael Tovar, Richard W. Fischer, Jens K. Norskov, and Robert Schlogl. The active site of methanol synthesis over $Cu/ZnO/Al_2O_3$ industrial catalysts. *Science*, 336(6083):893–897, 2012.

[25] J.-D Grunwaldt, A.M Molenbroek, N.-Y TopsâĹŽâĹŔe, H TopsâĹŽâĹŔe, and B.S Clausen. In situ investigations of structural changes in Cu/ZnO catalysts. *Journal of Catalysis*, 194(2):452 – 460, 2000.

[26] Charles T. Campbell. Ultrathin metal films and particles on oxide surfaces: Structural, electronic and chemisorptive properties. *Surf. Sci. Rep.*, 27(1âĂŽĂĎĂň3):1–111, 1997.

[27] Jun Hee Lee and Annabella Selloni. $TiO_2$/ferroelectric heterostructures as dynamic polarization-promoted catalysts for photochemical and electrochemical oxidation of water. *Physical review letters*, 112(19):196102, 2014.

[28] Arvin Kakekhani and Sohrab Ismail-Beigi. Ferroelectric-based catalysis: Switchable surface chemistry. *ACS Catalysis*, 5(8):4537–4545, 2015.

[29] Arvin Kakekhani and Sohrab Ismail-Beigi. Ferroelectric oxide surface chemistry: water splitting via pyroelectricity. *Journal of Materials Chemistry A*, 4(14):5235–5246, 2016.

[30] G. Parravano. Ferroelectric transitions and heterogenous catalysis. *The Journal of Chemical Physics*, 20(2):342–342, 1952.

[31] H. L. Stadler. Changing properties of metals by ferroelectric polarization charging. *Physical Review Letters*, 14(24):979–981, 1965.

[32] Y Ishibashi and HL Stadler. Ferroelectric electroreflectance of gold films. *Journal of Physics and Chemistry of Solids*, 30(9):2113–2116, 1969.

[33] Y. Inoue, K. Sato, and S. Suzuki. Polarization effects upon adsorptive and catalytic properties. II: surface electrical conductivity of NiO deposited on LiNbO3 and its changes upon gas adsorption. *Journal of physical chemistry*, 89(13):2827–2831, 1985.

[34] Yasunobu Inoue, Isao Yoshioka, and Kazunori Sato. Polarization effects upon adsorptive and catalytic properties. 1. carbon monoxide oxidation over palladium deposited on lithium niobate (LiNbO3) ferroelectrics. *The Journal of Physical Chemistry*, 88(6):1148–1151, March 1984.

[35] JM Vohs and MA Barteau. Conversion of methanol, formaldehyde and formic acid on the polar faces of zinc oxide. *Surface Science*, 176(1-2):91–114, 1986.

[36] JM Vohs and MA Barteau. Dehydration and dehydrogenation of ethanol and 1-propanol on the polar surfaces of zinc oxide. *Surface science*, 221(3):590–608, 1989.

[37] JM Vohs and MA Barteau. Reaction pathways and intermediates in the decomposition of acetic and propionic acids on the polar surfaces of zinc oxide. *Surface science*, 201(3):481–502, 1988.

[38] Claudine Noguera. Polar oxide surfaces. *Journal of Physics: Condensed Matter*, 12(31):R367, 2000.

[39] Johan M Carlsson. Electronic structure of the polar zno {0001}-surfaces. *Computational materials science*, 22(1):24–31, 2001.

[40] S Sanna, R Hölscher, and WG Schmidt. Temperature dependent linbo 3 (0001): Surface reconstruction and surface charge. *Applied Surface Science*, 301:70–78, 2014.

[41] DD Fong, AM Kolpak, JA Eastman, SK Streiffer, PH Fuoss, GB Stephenson, Carol Thompson, DM Kim, Kyoung Jin Choi, CB Eom, et al. Stabilization of monodomain polarization in ultrathin pbtio 3 films. *Physical review letters*, 96(12):127601, 2006.

[42] Yang Yun and Eric I. Altman. Using ferroelectric poling to change adsorption on oxide surfaces. *Journal of the American Chemical Society*, 129(50):15684–15689, December 2007.

[43] Li Li, Paul A. Salvador, and Gregory S. Rohrer. Photocatalysts with internal electric fields. *Nanoscale*, 6(1):24–42, 2014. WOS:000328673000001.

[44] Ionel Popescu, Adriana Urda, Tatiana Yuzhakova, Ioan-Cezar Marcu, Jozsef Kovacs, and Ioan Sandulescu. BaTiO3 and PbTiO3 perovskite as catalysts for methane combustion. *Comptes Rendus Chimie*, 12(9):1072–1078, September 2009.

[45] Mosha H. Zhao, Dawn A. Bonnell, and John M. Vohs. Effect of ferroelectric polarization on the adsorption and reaction of ethanol on BaTiO3. *Surface Science*, 602(17):2849–2855, September 2008.

[46] Dongbo Li, Mosha H. Zhao, J. Garra, A. M. Kolpak, A. M. Rappe, D. A. Bonnell, and J. M. Vohs. Direct in situ determination of the polarization dependence of physisorption on ferroelectric surfaces. *Nature Materials*, 7(6):473–477, June 2008.

[47] JL Wang, B Vilquin, and N Barrett. Screening of ferroelectric domains on batio3 (001) surface by ultraviolet photo-induced charge and dissociative water adsorption. *Applied Physics Letters*, 101(9):092902, 2012.

[48] Junsoo Shin, Von Braun Nascimento, Grégory Geneste, John Rundgren, E Ward Plummer, Brahim Dkhil, Sergei V Kalinin, and Arthur P Baddorf. Atomistic screening mechanism of ferroelectric surfaces: an in situ study of the polar phase in ultrathin batio3 films exposed to h2o. *Nano letters*, 9(11):3720–3725, 2009.

[49] Salim Nassreddine, Franck Morfin, Gang Niu, Bertrand Vilquin, François Gaillard, and Laurent Piccolo. Application of a sensitive catalytic reactor to the

study of co oxidation over srtio3 (100) and batio3/srtio3 (100) ferroelectric surfaces. *Surface and Interface Analysis*, 46(10-11):721–725, 2014.

[50] Yanyu Mi, Gregory Geneste, Julien E Rault, Claire Mathieu, Alexandre Pancotti, and Nicholas Barrett. Polarization dependent chemistry of ferroelectric batio3 (001) domains. *Journal of Physics: Condensed Matter*, 24(27):275901, 2012.

[51] S Roberts and RJ Gorte. A comparison of pt overlayers on $\alpha$-al2o3 (0001), zno (0001) zn, and zno (0001ÌĎ) o. *The Journal of Chemical Physics*, 93(7):5337–5344, 1990.

[52] Y. Yun, N. Pilet, U. D. Schwarz, and E. I. Altman. Comparison of the interaction of pd with positively and negatively poled LiNbO3(0 0 0 1). *Surface Science*, 603(20):3145–3154, October 2009.

[53] Markku Leskelä and Mikko Ritala. Atomic layer deposition (ald): from precursors to thin film structures. *Thin solid films*, 409(1):138–146, 2002.

[54] Al Y Cho and JR Arthur. Molecular beam epitaxy. *Progress in solid state chemistry*, 10:157–191, 1975.

[55] Yasunobu Inoue, Kazunori Sato, and Osamu Hayashi. Adsorptive properties of semiconducting thin nio and tio 2 films combined with an oppositely polarized ferroelectric support. *Journal of the Chemical Society, Faraday Transactions 1: Physical Chemistry in Condensed Phases*, 83(9):3061–3068, 1987.

[56] Yasunobu Inoue. Effects of acoustic waves-induced dynamic lattice distortion on catalytic and adsorptive properties of metal, alloy and metal oxide surfaces. *Surface science reports*, 62(8):305–336, 2007.

[57] Kevin Garrity, Arvin Kakekhani, Alexie Kolpak, and Sohrab Ismail-Beigi. Ferroelectric surface chemistry: First-principles study of the PbTiO3 surface. *Physical Review B*, 88(4):045401, July 2013.

[58] Andrew J Medford, Aleksandra Vojvodic, Jens S Hummelshøj, Johannes Voss, Frank Abild-Pedersen, Felix Studt, Thomas Bligaard, Anders Nilsson, and Jens K Nørskov. From the sabatier principle to a predictive theory of transition-metal heterogeneous catalysis. *Journal of Catalysis*, 328:36–42, 2015.

[59] Ashildur Logadottir, Thomas Holm Rod, Jens Kehlet Nørskov, Bjørk Hammer, Søren Dahl, and CJH Jacobsen. The brønsted–evans–polanyi relation and the volcano plot for ammonia synthesis over transition metal catalysts. *Journal of Catalysis*, 197(2):229–231, 2001.

[60] J. E. Jones. On the determination of molecular fields. II. from the equation of state of a gas. *Proceedings of the Royal Society of London. Series A*, 106(738):463–477, October 1924.

[61] A. K. Rappe, C. J. Casewit, K. S. Colwell, W. A. Goddard, and W. M. Skiff. UFF, a full periodic table force field for molecular mechanics and molecular dynamics simulations. *Journal of the American Chemical Society*, 114(25):10024–10035, December 1992.

[62] Murray S. Daw and M. I. Baskes. Embedded-atom method: Derivation and application to impurities, surfaces, and other defects in metals. *Physical Review B*, 29(12):6443–6453, June 1984.

[63] Robert J. Le Roy, Nikesh S. Dattani, John A. Coxon, Amanda J. Ross, Patrick Crozet, and Colan Linton. Accurate analytic potentials for li2(x $\sigma$1g+) and li2(a $\sigma$1u+) from 2 to 90 å, and the radiative lifetime of li(2p). *The Journal of Chemical Physics*, 131(20):204309, November 2009.

[64] E. Schrödinger. An undulatory theory of the mechanics of atoms and molecules. *Physical Review*, 28(6):1049–1070, December 1926.

[65] P. Hohenberg and W. Kohn. Inhomogeneous electron gas. *Physical Review*, 136:864–871, November 1964.

[66] W. Kohn and L. J. Sham. Self-consistent equations including exchange and correlation effects. *Physical Review A*, 140:1133–1138, 1965.

[67] W. Kohn and L. J. Sham. Self-consistent equations including exchange and correlation effects. *Physical Review*, 140(4A):A1133–A1138, November 1965.

[68] G. B. Bachelet, D. R. Hamann, and M. Schlüter. Pseudopotentials that work: From h to pu. *Physical Review B*, 26(8):4199–4228, October 1982.

[69] David Vanderbilt. Soft self-consistent pseudopotentials in a generalized eigenvalue formalism. *Physical Review B*, 41(11):7892–7895, April 1990.

[70] Stefan Grimme. Semiempirical GGA-type density functional constructed with a long-range dispersion correction. *Journal of Computational Chemistry*, 27(15):1787–1799, November 2006.

[71] Jens Antony and Stefan Grimme. Density functional theory including dispersion corrections for intermolecular interactions in a large benchmark set of biologically relevant molecules. *Physical Chemistry Chemical Physics*, 8(45):5287, 2006.

[72] Stefan Grimme, Jens Antony, Tobias Schwabe, and Christian M?ck-Lichtenfeld. Density functional theory with dispersion corrections for supramolecular structures, aggregates, and complexes of (bio)organic molecules. *Organic & Biomolecular Chemistry*, 5(5):741, 2007.

[73] Arthur F. Voter and Jimmie D. Doll. Transition state theory description of surface self-diffusion: Comparison with classical trajectory results. *The Journal of Chemical Physics*, 80(11):5832–5838, June 1984.

[74] Graeme Henkelman, Blas P. Uberuaga, and Hannes Jónsson. A climbing image nudged elastic band method for finding saddle points and minimum energy paths. *The Journal of Chemical Physics*, 113(22):9901–9904, 2000.

[75] A. J. Cohen, P. Mori-Sanchez, and W. Yang. Insights into current limitations of density functional theory. *Science*, 321(5890):792–794, August 2008.

[76] Per Stoltze. Surface science as the basis for the understanding of the catalytic synthesis of ammonia. *Physica Scripta*, 36(5):824, 1987.

[77] JK Nørskov and P Stoltze. Theoretical aspects of surface reactions. *Surface Science*, 189:91–105, 1987.

[78] K Honkala, Anders Hellman, IN Remediakis, Ashildur Logadottir, A Carlsson, Søren Dahl, Claus H Christensen, and Jens Kehlet Nørskov. Ammonia synthesis from first-principles calculations. *Science*, 307(5709):555–558, 2005.

[79] Shampa Kandoi, Jeff Greeley, Marco A Sanchez-Castillo, Steven T Evans, Amit A Gokhale, James A Dumesic, and Manos Mavrikakis. Prediction of experimental methanol decomposition rates on platinum from first principles. *Topics in catalysis*, 37(1):17–28, 2006.

[80] Suljo Linic, Jerome Jankowiak, and Mark A Barteau. Selectivity driven design of bimetallic ethylene epoxidation catalysts from first principles. *Journal of Catalysis*, 224(2):489–493, 2004.

[81] RD Cortright and JA Dumesic. Kinetics of heterogeneous catalytic reactions: Analysis of reaction schemes. *Advances in catalysis*, 46:161–264, 2001.

[82] Babatunde O. Alawode and Alexie M. Kolpak. $PbTiO_3(001)$ capped with $ZnO(11\bar{2}0)$: An ab initio study of effect of substrate polarization on interface composition and CO2 dissociation. *The Journal of Physical Chemistry Letters*, 7(7):1310–1314, 2016. PMID: 26996327.

[83] R Stuart Haszeldine. Carbon capture and storage: how green can black be? *Science*, 325(5948):1647–1652, 2009.

[84] K Garrity, AM Kolpak, S Ismail-Beigi, and EI Altman. Chemistry of ferroelectric surfaces. *Advanced materials*, 22(26-27):2969–2973, 2010.

[85] A Riefer, S Sanna, and WG Schmidt. Polarization-dependent methanol adsorption on lithium niobate z-cut surfaces. *Physical Review B*, 86(12):125410, 2012.

[86] Dongbo Li, Mosha H Zhao, J Garra, AM Kolpak, AM Rappe, DA Bonnell, and JM Vohs. Direct in situ determination of the polarization dependence of physisorption on ferroelectric surfaces. *nature materials*, 7(6):473–477, 2008.

[87] Christoph Baeumer, Diomedes Saldana-Greco, John Mark P. Martirez, Andrew M. Rappe, Moonsub Shim, and Lane W. Martin. Ferroelectrically driven spatial carrier density modulation in graphene. *Nat Commun*, 6, January 2015.

[88] Melanie Kurtz, Jennifer Strunk, Olaf Hinrichsen, Martin Muhler, Karin Fink, Bernd Meyer, and Christof Woll. Active sites on oxide surfaces: ZnO-Catalyzed synthesis of methanol from CO and h2. *Angewandte Chemie International Edition*, 44(18):2790–2794, April 2005.

[89] Y. R. Wang and C. B. Duke. Surface reconstructions of ZnO cleavage faces. *Surface science*, 192(2):309–322, 1987.

[90] B Meyer and Dominik Marx. Density-functional study of the structure and stability of zno surfaces. *Physical Review B*, 67(3):035403, 2003.

[91] Jo?rg Koßmann, Guido Roßmu?ller, and Christof Ha?ttig. Prediction of vibrational frequencies of possible intermediates and side products of the methanol synthesis on ZnO(0001) by ab initio calculations. *The Journal of Chemical Physics*, 136(3):034706, 2012.

[92] Na Sai, Alexie M. Kolpak, and Andrew M. Rappe. Ferroelectricity in ultrathin perovskite films. *Physical Review B*, 72(2):020101, July 2005.

[93] Rémi Arras, Victor G. Ruiz, Warren E. Pickett, and Rossitza Pentcheva. Tuning the two-dimensional electron gas at the LaAlO3/SrTiO3(001) interface by metallic contacts. *Physical Review B*, 85(12):125404, March 2012.

[94] Paolo Giannozzi, Stefano Baroni, Nicola Bonini, Matteo Calandra, Roberto Car, Carlo Cavazzoni, Davide Ceresoli, Guido L Chiarotti, and Matteo Cococcioni. QUANTUM ESPRESSO: a modular and open-source software project for quantum simulations of materials. *Journal of Physics: Condensed Matter*, 21(39):19, 2009.

[95] Z. Wu and R. E. Cohen. More accurate generalized gradient approximation for solids. *Physical Review B*, 73(23):235116, 2006.

[96] Fabien Tran, Robert Laskowski, Peter Blaha, and Karlheinz Schwarz. Performance on molecules, surfaces, and solids of the wu-cohen GGA exchange-correlation energy functional. *Physical Review B*, 75(11), March 2007.

[97] Lennart Bengtsson. Dipole correction for surface supercell calculations. *Physical Review B*, 59(19):12301, 1999.

[98] A. Dutta, T. K. Chaudhuri, and S. Basu. Deposition and characterization of zinc oxide thin films for hydrogen sensor devices. *Materials Science and Engineering: B*, 14(1):31–35, 1992.

[99] Jin-Hong Lee and Byung-Ok Park. Transparent conducting zno: Al, in and sn thin films deposited by the sol–gel method. *Thin Solid Films*, 426(1):94–99, 2003.

[100] Andriy Zakutayev, Nicola H Perry, Thomas O Mason, David S Ginley, and Stephan Lany. Non-equilibrium origin of high electrical conductivity in gallium zinc oxide thin films. *Applied Physics Letters*, 103(23):232106, 2013.

[101] Frederic C Meunier. Mixing copper nanoparticles and zno nanocrystals: A route towards understanding the hydrogenation of co2 to methanol? *Angewandte Chemie International Edition*, 50(18):4053–4054, 2011.

[102] Andrea Dal Corso, Michel Posternak, Raffaele Resta, and Alfonso Baldereschi. Ab initio study of piezoelectricity and spontaneous polarization in zno. *Physical Review B*, 50(15):10715, 1994.

[103] Fabio Bernardini, Vincenzo Fiorentini, and David Vanderbilt. Spontaneous polarization and piezoelectric constants of iii-v nitrides. *Physical Review B*, 56(16):R10024, 1997.

[104] Jun Liu, Xiaolong Chen, Wenjun Wang, Yu Liu, Qingsong Huang, and Zaiping Guo. Self-assembly of [101 [combining macron] 0] grown zno nanowhiskers with exposed reactive (0001) facets on hollow spheres and their enhanced gas sensitivity. *CrystEngComm*, 13(10):3425–3431, 2011.

[105] Xiang Yang Kong and Zhong Lin Wang. Polar-surface dominated zno nanobelts and the electrostatic energy induced nanohelixes, nanosprings, and nanospirals. *Applied Physics Letters*, 84(6):975–977, 2004.

[106] Jing Hui Zeng, Bin Bin Jin, and Ye Feng Wang. Facet enhanced photocatalytic effect with uniform single-crystalline zinc oxide nanodisks. *Chemical Physics Letters*, 472(1):90–95, 2009.

[107] Malte Behrens, Felix Studt, Igor Kasatkin, Stefanie Kühl, Michael Hävecker, Frank Abild-Pedersen, Stefan Zander, Frank Girgsdies, Patrick Kurr, Benjamin-Louis Kniep, et al. The active site of methanol synthesis over cu/zno/al2o3 industrial catalysts. *Science*, 336(6083):893–897, 2012.

[108] A. Onodera. Novel ferroelectricity in II-VI semiconductor ZnO. *Ferroelectrics*, 267(1):131–137, 2002.

[109] X. S. Wang, Z. C. Wu, J. F. Webb, and Z. G. Liu. Ferroelectric and dielectric properties of li-doped ZnO thin films prepared by pulsed laser deposition. *Applied Physics A*, 77(3-4):561–565, August 2003.

[110] C. W. Zou, M. Li, H. J. Wang, M. L. Yin, C. S. Liu, L. P. Guo, D. J. Fu, and T. W. Kang. Ferroelectricity in li-implanted ZnO thin films. *Nuclear Instruments & Methods in Physics Research Section B-Beam Interactions with Materials and Atoms*, 267(7):1067–1071, April 2009. WOS:000266155000004.

[111] S. Massidda, R. Resta, M. Posternak, and A. Baldereschi. Polarization and dynamical charge of zno within different one-particle schemes. *Phys. Rev. B*, 52:R16977–R16980, Dec 1995.

[112] Y. Noel, C. M. Zicovich-Wilson, B. Civalleri, Ph. D'Arco, and R. Dovesi. Polarization properties of zno and beo: An *ab initio* study through the berry phase and wannier functions approaches. *Phys. Rev. B*, 65:014111, Dec 2001.

[113] Andrea Dal Corso, Michel Posternak, Raffaele Resta, and Alfonso Baldereschi. *Ab initio* study of piezoelectricity and spontaneous polarization in zno. *Phys. Rev. B*, 50:10715–10721, Oct 1994.

[114] Claudine Noguera. Polar oxide surfaces. *Journal of Physics: Condensed Matter*, 12(31):R367, 2000.

[115] Olga Dulub, Lynn A Boatner, and Ulrike Diebold. Stm study of the geometric and electronic structure of zno (0001)-zn,(0001)-o,(1010), and (1120) surfaces. *Surface Science*, 519(3):201–217, 2002.

[116] Colin L Freeman, Frederik Claeyssens, Neil L Allan, and John H Harding. Graphitic nanofilms as precursors to wurtzite films: theory. *Physical Review Letters*, 96(6):066102, 2006.

[117] Dangxin Wu, MG Lagally, and Feng Liu. Stabilizing graphitic thin films of wurtzite materials by epitaxial strain. *Physical Review Letters*, 107(23):236101, 2011.

[118] Lixin Zhang and Hanchen Huang. Structural transformation of zno nanostructures. *Applied Physics Letters*, 90(2):023115, 2007.

[119] Bin Wen and Roderick Melnik. Relative stability of nanosized wurtzite and graphitic zno from density functional theory. *Chemical Physics Letters*, 466(1):84–87, 2008.

[120] Frederik Claeyssens, Colin L Freeman, Neil L Allan, Ye Sun, Michael NR Ashfold, and John H Harding. Growth of ZnO thin films âĂŤ experiment and theory. *Journal of Materials Chemistry*, 15(1):139–148, 2005.

[121] C Tusche, HL Meyerheim, and J Kirschner. Observation of depolarized zno (0001) monolayers: formation of unreconstructed planar sheets. *Physical Review Letters*, 99(2):026102, 2007.

[122] X. H. Wei, Y. R. Li, J. Zhu, W. Huang, Y. Zhang, W. B. Luo, and H. Ji. Epitaxial properties of ZnO thin films on SrTiO[sub 3] substrates grown by laser molecular beam epitaxy. *Applied Physics Letters*, 90(15):151918, 2007.

[123] Christof Wöll. The chemistry and physics of zinc oxide surfaces. *Progress in Surface Science*, 82(2):55–120, 2007.

[124] S Akhter, K Lui, and Harold H Kung. Comparison of the chemical properties of the zinc-polar, the oxygen-polar, and the nonpolar surfaces of zinc oxide. *The Journal of Physical Chemistry*, 89(10):1958–1964, 1985.

[125] Angelos Michaelides, Z.-P. Liu, C. J. Zhang, Ali Alavi, David A. King, and P. Hu. Identification of general linear relationships between activation energies and enthalpy changes for dissociation reactions at surfaces. *Journal of the American Chemical Society*, 125(13):3704–3705, 2003.

[126] T. Bligaard, J.K. Norskov, S. Dahl, J. Matthiesen, C.H. Christensen, and J. Sehested. The brønsted–evans–polanyi relation and the volcano curve in heterogeneous catalysis. *Journal of Catalysis*, 224(1):206 – 217, 2004.

[127] Jun Hee Lee and Annabella Selloni. $tio_2$. *Phys. Rev. Lett.*, 112:196102, May 2014.

[128] Daniel Sheppard, Rye Terrell, and Graeme Henkelman. Optimization methods for finding minimum energy paths. *The Journal of Chemical Physics*, 128(13):134106, 2008.

[129] [http://webbook.nist.gov/chemistry/].

[130] T Bligaard, JK Nørskov, S Dahl, J Matthiesen, CH Christensen, and J Sehested. The brønsted–evans–polanyi relation and the volcano curve in heterogeneous catalysis. *Journal of Catalysis*, 224(1):206–217, 2004.

[131] JN Bronsted. Acid and basic catalysis. *Chemical Reviews*, 5(3):231–338, 1928.

[132] MG Evans and Michael Polanyi. Inertia and driving force of chemical reactions. *Transactions of the Faraday Society*, 34:11–24, 1938.

[133] [http://webbook.nist.gov/chemistry/].

[134] Yong Liu, Yi Zhang, Tiejun Wang, and Noritatsu Tsubaki. Efficient conversion of carbon dioxide to methanol using copper catalyst by a new low-temperature hydrogenation process. *Chemistry Letters*, 36(9):1182–1183, 2007.

[135] Xu and J. A. Moulijn. Mitigation of CO2 by chemical conversion: Plausible chemical reactions and promising products. *Energy & Fuels*, 10(2):305–325, January 1996.

[136] Andrew A. Peterson, Frank Abild-Pedersen, Felix Studt, Jan Rossmeisl, and Jens K. Nørskov. How copper catalyzes the electroreduction of carbon dioxide into hydrocarbon fuels. *Energy & Environmental Science*, 3(9):1311, 2010.

[137] C Woll. The chemistry and physics of zinc oxide surfaces. *Progress in Surface Science*, 82(2-3):55–120, 2007.

[138] Andrew J Medford, Jens Sehested, Jan Rossmeisl, Ib Chorkendorff, Felix Studt, Jens K Nørskov, and Poul Georg Moses. Thermochemistry and micro-kinetic analysis of methanol synthesis on zno (0001). *Journal of Catalysis*, 309:397–407, 2014.

[139] H Xu, Lei Dong, Xing Qiang Shi, Michel Andre Van Hove, Wing Kin Ho, Nian Lin, Hua Sheng Wu, and Shuk Yin Tong. Stabilizing forces acting on zno polar surfaces: Stm, leed, and dft. *Physical Review B*, 89(23):235403, 2014.

[140] Georg Kresse, Olga Dulub, and Ulrike Diebold. Competing stabilization mechanism for the polar zno (0001)-zn surface. *Physical Review B*, 68(24):245409, 2003.

[141] Michael Bowker, Hilary Houghton, and Kenneth C Waugh. Mechanism and kinetics of methanol synthesis on zinc oxide. *Journal of the Chemical Society, Faraday Transactions 1: Physical Chemistry in Condensed Phases*, 77(12):3023–3036, 1981.

[142] Kevin Kähler, Marie Christine Holz, Markus Rohe, Jennifer Strunk, and Martin Muhler. Probing the reactivity of zno and au/zno nanoparticles by methanol adsorption: a tpd and drifts study. *ChemPhysChem*, 11(12):2521–2529, 2010.

[143] PM Jones, JA May, JB Reitz, and Edward I Solomon. Photoelectron spectroscopic and electronic structure studies of ch2o bonding and reactivity on zno surfaces: Steps in the methanol synthesis reaction. *Inorganic chemistry*, 43(11):3349–3370, 2004.

[144] Lin-Fei Xiao, Fu-Wei Li, Jia-Jian Peng, and Chun-Gu Xia. Immobilized ionic liquid/zinc chloride: Heterogeneous catalyst for synthesis of cyclic carbonates from carbon dioxide and epoxides. *Journal of Molecular Catalysis A: Chemical*, 253(1-2):265–269, July 2006.

[145] Takashi Yano, Hideo Matsui, Takahiro Koike, Hiroyasu Ishiguro, Hisashi Fujihara, Masakuni Yoshihara, and Toshihisa Maeshima. Magnesium oxide-catalysed reaction of carbon dioxide with an epoxide with retention of stereochemistry. *Chemical Communications*, (12):1129–1130, 1997.

[146] Yunjo Kim, Samuel S Cruz, Kyusang Lee, Babatunde O Alawode, Chanyeol Choi, Yi Song, Jared M Johnson, Christopher Heidelberger, Wei Kong, Shinhyun Choi, et al. Remote epitaxy through graphene enables two-dimensional material-based layer transfer. *Nature*, 544(7650):340–343, 2017.

[147] Atsushi Koma, Kazumasa Sunouchi, and Takao Miyajima. Fabrication and characterization of heterostructures with subnanometer thickness. *Microelectronic Engineering*, 2(1-3):129–136, 1984.

[148] Atsushi Koma, Kazumasa Sunouchi, and Takao Miyajima. *Fabrication of ultrathin heterostructures with van der Waals epitaxy.* PhD thesis, AVS, 1985.

[149] Jan H Van Der Merwe, J Woltersdorf, and WA Jesser. Low energy dislocation structures in epitaxy. *Materials Science and Engineering*, 81:1–33, 1986.

[150] JW Matthews and AE Blakeslee. Defects in epitaxial multilayers: I. misfit dislocations. *Journal of Crystal Growth*, 27:118–125, 1974.

[151] Muhammad Iqbal Bakti Utama, Qing Zhang, Jun Zhang, Yanwen Yuan, Francisco J Belarre, Jordi Arbiol, and Qihua Xiong. Recent developments and future directions in the growth of nanostructures by van der waals epitaxy. *Nanoscale*, 5(9):3570–3588, 2013.

[152] T Löher, Y Tomm, A Klein, D Su, C Pettenkofer, and W Jaegermann. Highly oriented layers of the three-dimensional semiconductor cdte on the two-dimensional layered semiconductors mote2 and wse2. *Journal of applied physics*, 80(10):5718–5722, 1996.

[153] T Löher, Y Tomm, C Pettenkofer, and W Jaegermann. Van der waals epitaxy of three-dimensional cds on the two-dimensional layered substrate mote2 (0001). *Applied physics letters*, 65(5):555–557, 1994.

[154] Rui Huang. Show of adhesive strength. *Nat Nanotechnol*, 6:537–8, 2011.

[155] Kunook Chung, Chul-Ho Lee, and Gyu-Chul Yi. Transferable gan layers grown on zno-coated graphene layers for optoelectronic devices. *Science*, 330(6004):655–657, 2010.

[156] Yasuyuki Kobayashi, Kazuhide Kumakura, Tetsuya Akasaka, and Toshiki Makimoto. Layered boron nitride as a release layer for mechanical transfer of gan-based devices. *Nature*, 484(7393):223–227, 2012.

[157] Kunook Chung, Suk In Park, Hyeonjun Baek, Jin-Seok Chung, and Gyu-Chul Yi. High-quality gan films grown on chemical vapor-deposited graphene films. *NPG Asia Materials*, 4(9):e24, 2012.

[158] Hyobin Yoo, Kunook Chung, Suk In Park, Miyoung Kim, and Gyu-Chul Yi. Microstructural defects in gan thin films grown on chemically vapor-deposited graphene layers. *Applied Physics Letters*, 102(5):051908, 2013.

[159] Neeraj Nepal, Virginia D Wheeler, Travis J Anderson, Francis J Kub, Michael A Mastro, Rachael L Myers-Ward, Syed B Qadri, Jaime A Freitas, Sandra C Hernandez, Luke O Nyakiti, et al. Epitaxial growth of iii–nitride/graphene heterostructures for electronic devices. *Applied Physics Express*, 6(6):061003, 2013.

[160] L Liu and James H Edgar. Substrates for gallium nitride epitaxy. *Materials Science and Engineering: R: Reports*, 37(3):61–127, 2002.

[161] Yumeng Shi, Wu Zhou, Ang-Yu Lu, Wenjing Fang, Yi-Hsien Lee, Allen Long Hsu, Soo Min Kim, Ki Kang Kim, Hui Ying Yang, Lain-Jong Li, et al. van der waals epitaxy of mos2 layers using graphene as growth templates. *Nano letters*, 12(6):2784–2791, 2012.

[162] Pascal Gehring, Bo F Gao, Marko Burghard, and Klaus Kern. Growth of high-mobility bi2te2se nanoplatelets on hbn sheets by van der waals epitaxy. *arXiv preprint arXiv:1301.6601*, 2013.

[163] Chih-Jen Shih, Michael S Strano, and Daniel Blankschtein. Wetting translucency of graphene. *Nature materials*, 12(10):866–869, 2013.

[164] Rishi Raj, Shalabh C Maroo, and Evelyn N Wang. Wettability of graphene. *Nano letters*, 13(4):1509–1515, 2013.

[165] John P. Perdew, J. A. Chevary, S. H. Vosko, Koblar A. Jackson, Mark R. Pederson, D. J. Singh, and Carlos Fiolhais. Atoms, molecules, solids, and surfaces: Applications of the generalized gradient approximation for exchange and correlation. *Physical Review B*, 46(11):6671–6687, September 1992.

[166] EM Kneedler, BT Jonker, PM Thibado, RJ Wagner, BV Shanabrook, and LJ Whitman. Influence of substrate surface reconstruction on the growth and magnetic properties of fe on gaas (001). *Physical Review B*, 56(13):8163, 1997.

[167] R Moosbühler, F Bensch, M Dumm, and G Bayreuther. Epitaxial fe films on gaas (001): Does the substrate surface reconstruction affect the uniaxial magnetic anisotropy? *Journal of Applied Physics*, 91(10):8757–8759, 2002.

[168] M Temmen, O Ochedowski, M Schleberger, M Reichling, and TRJ Bollmann. Hydration layers trapped between graphene and a hydrophilic substrate. *New Journal of Physics*, 16(5):053039, 2014.

[169] Manisha Chhikara, Egon Pavlica, Aleksandar MatkovicÌĄ, RadosÌŇ GajicÌĄ, and Gvido Bratina. Effect of water layer at the sio2/graphene interface on pentacene morphology. *Langmuir*, 30(39):11681–11688, 2014.

[170] Zengguang Cheng, Qiaoyu Zhou, Chenxuan Wang, Qiang Li, Chen Wang, and Ying Fang. Toward intrinsic graphene surfaces: a systematic study on thermal annealing and wet-chemical treatment of sio2-supported graphene devices. *Nano letters*, 11(2):767–771, 2011.

[171] Yung-Chang Lin, Chun-Chieh Lu, Chao-Huei Yeh, Chuanhong Jin, Kazu Suenaga, and Po-Wen Chiu. Graphene annealing: how clean can it be? *Nano letters*, 12(1):414–419, 2011.